④

FIRST ANNUAL REPORT

FOR THE PROJECT

"COMPOSITE CERAMIC SUPERCONDUCTING
WIRES FOR ELECTRIC MOTOR APPLICATIONS"

PRIME CONTRACTOR

CERAMICS PROCESS SYSTEMS CORPORATION
155 FORTUNE BOULEVARD
MILFORD, MASSACHUSETTS 01757

7 JULY 1989

DTIC
ELECTE
JUL 1 9 1989
S D

**CERAMICS** *PROCESS SYSTEMS*

FIRST ANNUAL REPORT

FOR THE PROJECT

"COMPOSITE CERAMIC SUPERCONDUCTING
WIRES FOR ELECTRIC MOTOR APPLICATIONS"

PRIME CONTRACTOR

CERAMICS PROCESS SYSTEMS CORPORATION
155 FORTUNE BOULEVARD
MILFORD, MASSACHUSETTS   01757

7 JULY 1989

CPS 89-009

DARPA ORDER NO:   9525
CONTRACT NO:   N00014-88-C-0512
CONTRACT EFFECTIVE DATE:   30 JUNE 1988
CONTRACT EXPIRATION DATE: 31 MARCH 1991
PRINCIPAL INVESTIGATOR:   JOHN W. HALLORAN
(508) 634-3422

Prepared for
DEFENSE ADVANCED RESEARCH PROJECTS AGENCY
1400 Wilson Boulevard
Arlington, VA   22209

OFFICE OF NAVAL RESEARCH
800 North Quincy Street
Arlington, VA   22217-5000

APPROVED FOR PUBLIC RELEASE:   DISTRIBUTION IS UNLIMITED

# REPORT DOCUMENTATION PAGE

| 1. AGENCY USE ONLY (Leave blank) | 2. REPORT DATE | 3. REPORT TYPE AND DATES COVERED |
|---|---|---|
| | July 7, 1989 | Technical Report 6/30/88 – 6/30/89 |

| 4. TITLE AND SUBTITLE | 5. FUNDING NUMBERS |
|---|---|
| Composite Ceramic Superconducting Wires for Electric Motor Applications | N00014-88-C-0512 |

**6. AUTHOR(S)**

J. W. Halloran

| 7. PERFORMING ORGANIZATION NAME(S) AND ADDRESS(ES) | 8. PERFORMING ORGANIZATION REPORT NUMBER |
|---|---|
| Ceramics Process Systems Corporation<br>155 Fortune Boulevard<br>Milford, MA 01757 | CPS 89-009 |

| 9. SPONSORING/MONITORING AGENCY NAME(S) AND ADDRESS(ES) | 10. SPONSORING/MONITORING AGENCY REPORT NUMBER |
|---|---|
| Defense Advanced Research Projects Agency<br>1400 Wilson Boulevard, Arlington, VA 22209<br><br>Office of Naval Research<br>800 North Quincy Street, Arlington, VA 22217-500 | |

**11. SUPPLEMENTARY NOTES**

N/A

| 12a. DISTRIBUTION/AVAILABILITY STATEMENT | 12b. DISTRIBUTION CODE |
|---|---|
| Unlimited | |

**13. ABSTRACT (Maximum 200 words)**

This report describes progress on developing Y-123 wire for an HTSC motor. The wire development involves synthesis of Y-123 powder, spinning polymer-containing "green fiber", heat treating the fiber to produce metallized superconducting filaments, and characterizing the electrical properties. A melt spinning process was developed for producing 125-micron diameter green fiber containing 50 vol% Y-123. This fiber can be braided for producing transposed multifilamentary wire. A process was developed to coat green fiber with silver alloys which can be co-fired to yield Ag-clad Y-123 wire. Half-meter prototypes of wire were produced by continuous sintering. A second process for multifilamentary ribbon wire is also being developed. The Y-123 filaments have 77° self-field $J_c$ values up to 2600 A/cm$^2$, but $J_c$ is reduced to 10 A/cm$^2$ at 800 G. Preliminary data is presented on mechanical properties.

A DC homopolar motor with an iron magnetic circuit is being designed at Emerson Electric as the first proof-of-principle motor. This machine is designed to operate with early HTSC wire. A cryogenic induction motor is being evaluated as a second application. Models have been developed to calculate eddy current loss, hysteresis loss, and adiabatic and dynamic stability in HTSC wires.

| 14. SUBJECT TERMS | | | 15. NUMBER OF PAGES |
|---|---|---|---|
| Superconductor, ceramic, motor | | | 181 |
| | | | 16. PRICE CODE |

| 17. SECURITY CLASSIFICATION OF REPORT | 18. SECURITY CLASSIFICATION OF THIS PAGE | 19. SECURITY CLASSIFICATION OF ABSTRACT | 20. LIMITATION OF ABSTRACT |
|---|---|---|---|
| Unclassified | Unclassified | Unclassified | |

# COMPOSITE CERAMIC SUPERCONDUCTING WIRES FOR ELECTRIC MOTOR APPLICATIONS

## EXECUTIVE SUMMARY

This report describes progress on producing Y-123 wire for an HTSC motor. The wire development activity includes synthesis of Y-123 powder, spinning polymer-containing "green fiber", heac treating the fiber to produce metallized superconducting filaments, and characterizing the electrical properties of the filaments. The HTSC motor has been designed and will be built by Emerson Electric Company.

Signifiant progress has been made on the both the HTSC wire and on the design of HTSC motors. The program is close to the original schedule on all major tasks. Prototype clad wire has been made in about half-meter lengths, and the first coils of wire for the proof-of-principle motor are expected in the second quarter of the coming year.

The design of flexible clad-fiber HTSC wire was refined for both ribbon conductor design and a simpler monofil wire design. The relationship between diameter and bending radius was quantified, and compared with preliminary data. The strength of metal clad fiber was calculated. Concepts and methods for producing filament transposition were defined. Progress was made in defining the eddy current and and hysteretic losses for HTSC wire, and determining the adiabatic and dynamic stability of ribbon conductors.

A process was placed into operation to manufacture reproducible phase pure Y-123 powder in kilogram quantities. This powder is made by solid state reaction, controlled to yield at least 98 wt% of the Y-123 phase, with traces of barium carbonate, barium cuprate, and "211". Jet-milling is used to produce a highly sinterable powder with an average particle size of $1.6 \pm 0.2$ microns and specific surface area of $2.5 \pm 0.3$ m$^2$/gm. All of the recent Y-123 green fibers are made with this powder.

A novel melt spinning process has been developed at Albany International Research Company to manufacture continuous green fiber containing 50 vol% Y-123 carried in a polymer blend. The melt spun fibers are made with conventional fiber spinning equipment with a process which readily lends itself to scale-up. Consequently, melt spinning has been adopted as the preferred method of producing green fiber. The solvent-based dry spinning method is used only for small experimental lots.

A large number of thermoplastic resins, carrier polymer-lubricant blends, and processing conditions have been explored. The evaulations were based on processibility, binder burnout behavior, and properties related to continuous sintering of fibers. High density polyethylene-based systems presently make the best green fiber with Y-123. Melt spun green fiber has been prepared with diameters ranging between 50 and 330 microns at lengths up to about 0.5 kilometer. The current standard green fiber diameter is 125 micron in diameter. This grade of fiber is being used to supply the cladding and sintering operations. Development efforts continue to reduce fiber diameter down to about 10 microns, to allow a more flexible wire to be produce.

The feasibility using braided Y-123 green fiber to produce multifilamentary wire with transposed filaments has been supported by recent success in producing continuous braids from the HDPE-based green fiber using a conventional braiding machine. Earlier work on simple braids showed that binder burnout and sintering is possible with braided green fiber.

The Y-123 green fiber can be coated with a silver or Ag/Pd alloy coating, which can be co-fired with the Y-123 during sintering. For the ribbon wire, the silver alloy coating provides a wettable surface for adhesion of the solder and acts as a barrier isolating the Y-123 from the solder. For the monofil wire, the silver alloy coating is the primary metallization, and serves all of the functions of the stabilizing metal. Presently about 100 meters of fiber are coated continuously. The system is still being developed to produce thicker, more uniform coatings.

The green fibers are sintered by two techniques. The older method, multiple zone sintering, produced 10-cm long samples by moving the fiber through the hot zone of a small tube furnace. Typically, a Y-123 fiber was exposed to about six repeated passes through the furnace, each involving 0.5- 5 minutes at peak temperature. Zone sintering was used to simulate continuous sintering, and to evaluate the sinterability of experimental powders and fibers, and to produce dense Y-123 filaments with self field critical currents as high as 2600 A/cm$^2$. Microstructure development during zone sintering has been characterized.

A commercial belt furnace was modifed make it suitable for continuous sintering of fibers. This is currently being used to develop a process for continuous sintering of bare and Ag-coated Y-123 fiber. Green fibers are fed into a belt furnace for binder removal and sintering. This process is the prototype for reel-to-reel manufacture, and has replaced the zone sintering method. To progress from the tube furnace to the belt furnace it was necessary to overcome a number of practical problems related to the burnout characteristics of the green fiber, adhesion of the fiber to the belt cover, and some mechanical difficulties with the furnace itself. At present, fibers can only be semi-continuously sintered. The filament length was limited by the present need to pass the fibers through the belt furnace several times for binder burnout, presintering, and sintering.

The achievement of semi-continuous fiber sintering is significant because it demonstrates that coated green fiber an be carried through binder burnout and densification continuously without breaking. This indicates that the manufacture of composite wire from green fiber is feasible. Experiments on meter-length samples are in progress to define an optimal heating schedule. Based on these results, additional heating zones will be installed on the belt furnace so it can operate in true reel-to-reel mode.

A solder reflow method was developed to clad fibers to make the ribbon wire. A cladding machine has been built to do continuous cladding of continuous sintered Y-123 filaments. This machine is designed to fabricate the ribbon by sandwiching a sintered fiber array between copper foil strips and solder bonding them. The cladding module is presently being tested.

Techniques were developed to directly measure the transport properties of single Y-123 filaments. The resistive transition show that the quality of the 100-micron filaments is equivalent to the best polycrystalline Y-123. Filaments have been produced with self-field critical currents up to 2600 A/cm$^2$, with typical performance around 1500 A/cm$^2$, both bare and metal clad specimen. These filaments, like all bulk Y-123, are weak-linked, so the $J_c$ drops to around 10 A/cm$^2$ at 800 G.

Preliminary data on the mechanical properties of sintered Y-123 filaments indicate a fracture strength of 75-180 MPa. This data has been used to predict that long coils, with a 10-cm radius of curvature, can be wound from Ag/Pd clad 100 micron diameter filaments.

Notable progress has been made at Emerson Electric in HTSC motor design. After considering the characteristics of DC homopolar, heteropolar, reluctance, and induction motors, the induction and homopolar machines were selected as the machines for proof-of-principal. Assuming that current capacity and flexibility of early Y-123 wire will be limited, a novel type of drum homopolar machine has been designed. This machine has simple bobbin wound field coils to minimize bending stresses on the Y-123 wire and an iron magnetic circuit to allow useful horsepower output from as little as a 300 G field. A second motor under investigation is a cryogenic induction machine.

# TABLE OF CONTENTS

## LIST OF FIGURES

## LIST OF TABLES

COMPOSITE CERAMIC SUPERCONDUCTING WIRES FOR
ELECTRIC MOTOR APPLICATIONS

JOHN W. HALLORAN
PRINCIPAL INVESTIGATOR
CERAMICS PROCESS SYSTEMS CORPORATION
MILFORD, MASSACHUSETTS

SECTION 1

GENERAL INTRODUCTION

This First Annual Report covers activities from July 1988 through June 1989, on a program to develop high temperature superconducting wire by cladding $YBa_2Cu_3O_{7-x}$ (Y-123) ceramic fibers with metal, and to use this wire to build a superconducting motor. This program is being carried out by three subcontractors: an affiliate of Ceramics Process Systems, CPS Superconductor Corporation (CPSS) is charged with development of the wire; the fiber spinning technology is being developed with Albany International Research Corporation (AIResCo); and the Emerson Motor Division (EMD) of Emerson Electric is designing and will build the superconducting motor. Another contributing organization is the University of Wisconsin Applied Superconductivity Center, which is acting as a consultant to Emerson Electric on motor design and the properties of high temperature superconductors.

The first year progress measured against intermediate milestones has been very good, considering the uncertainties of research of this kind. The production of continuous wire and building the HTSC motor are milestones for late 1989 and early 1990, so these milestones were not achieved in the first year of the program.

We have demonstrated the feasibility of the fiber-wire process by producing a sample of superconducting silver alloy clad Y-123 wire using the

continuous sintering furnace. The wire sample is longer than the furnace, proving that the Y-123 fiber can be carried through binder burnout and densification continuously without breaking. The length was limited because the wire was passed through the belt furnace several times for binder burnout, presintering, and sintering. Experiments on meter-length samples are in progress to define an optimal heating schedule. Based on these results, we will install additional heating zones on the belt furnace so it can operate in true reel-to-reel mode.

The design of fiber process HTSC wire was refined for both ribbon conductor design and a simpler monofil wire design. The relationship between diameter and bending radius was quantified, and compared with preliminary data. The strength of metal clad fiber was calculated. Progress was made in defining the critical twist pitch and hysteretic losses for HTSC wire, and determining the adiabatic and dynamic stability of ribbon conductors.

To supply program needs, we developed a process for manufacturing reproducible phase pure 1.6 $\mu$ Y-123 powder in kilogram quantities. This powder is highly sinterable and can consistently be made with little variation in surface area or particle size distribution.

Very important progress has been made at Albany International Research Company in fiber spinning, resulting in the invention of a melt spinning process to manufacture continuous green fiber containing 50 vol% Y-123 carried in a polymer blend. This process works with conventional fiber spinning equipment, using a wide variety of carrier polymers. We have prepared green fiber with diameters between 2 and 13 mils at lengths up to about 0.5 kilometer. Typically we prepare spools with about 100 meters of 125 micron diameters fiber. The preferred fiber variety can be heat treated to

produce a continuous superconducting filament. The Y-123 green fibers can be braided on conventional braiding machines to produce continuous multifilament arrays with complete filament transposition.

We developed a process to continuously coat green fiber with a silver or Ag/Pd alloy coating, which is co-fired with the Y-123 during sintering. For the ribbon wire concept, the silver alloy coating has two functions: it provides a wettable surface for adhesion of the solder and is a thin barrier isolating the Y-123 from the solder. For the monofil wire, the silver alloy coating is the primary metallization, and serves all of the functions of the stabilizing metal.

We developed a process for continuous sintering of bare and Ag-coated Y-123 fiber. Green fibers are fed into a belt furnace for binder removal and sintering. This process is the prototype for reel-to-reel manufacture. This replaced our lab-scale zone sintering method, which produced 10-cm long samples by moving the fiber through the hot zone of a small tube furnace. To progress from the tube furnace to the belt furnace it was necessary to overcome a number of practical problems related to the burnout characteristics of the green fiber, adhesion of the fiber to the belt cover, and some mechanical difficulties with the furnace itself.

We designed and built a cladding module for the ribbon wire. This machine is designed to fabricate the ribbon by sandwiching a sintered fiber array between copper foil strips and solder bonding them. The cladding module is presently being tested.

We have produced filaments with self-field critical currents up to 2600 A/cm$^2$, with typical performance around 1500 A/cm$^2$, both bare and metal clad. These filaments, like all bulk Y-123, are weak-linked.

Notable progress has been made at Emerson Electric in HTSC motor design. After considering the characteristics of DC homopolar, heteropolar, reluctance, and induction motors, the induction and homopolar machines were selected as the machines for proof-of-principal. Assuming that current capacity and flexibility of early Y-123 wire will be limited, a novel type of drum homopolar machine has been designed. This machine has simple bobbin wound field coils to minimize bending stresses on the Y-123 wire and an iron magnetic circuit to allow useful horsepower output from as little as a 300 G field.

The program did have several setbacks. For the first six months raw material was a problem. While we planned to eventually produce our own Y-123 powder, we expected to use a commercial powder to begin the program. We had encouraging results with one commercial lot, but were unable to obtain more. This forced us to develop our own process for producing Y-123 powders in the one-kilogram quantities required for melt spinning of fibers. We were quite sucessful and now have a pilot-scale process producing excellent powder at high yield, but several months were invested in producing and evaluating trial lots of powder.

We have not yet produced textured Y-123. We have not yet been able to produce platy Y-123 particles as a sinterable powder, so have not induced rheological texture by the spinning operation. Our original concept of inducing texture during sintering by means of directional recrystallization also has not yet been successful.

Most importantly, we have not been able to produce strong-linked high critical current density material from bulk polycrystalline Y-123 fibers. This is not surprising, as all credible data on conventionally sintered Y-123

show that it is weak-linked. We have begun to explore other avenues which could lead to strong-linked HTSC filaments. These involve a novel melt processing of Y-123 fibers and controlled sintering of thallium calcium barium cuprate fibers.

The status of the program is compared with individual tasks of the Statement of Work in Figures 1.1, 1.2, and 1.3, which show timelines for the major fiber and wire development tasks and the HTSC motor development, comparing actual progress with the original program schedule. Actual program activities have diverged somewhat from the original work statement, as we exploited new opportunities, pursued alternatives to electroplating for cladding, and worked through difficulties. The changes mostly reflect the fact that the program involves development of a process with about fourteen major steps, most of which are novel, and which must be developed in parallel. This has delayed our progress in the last two steps, continuous sintering and cladding, which require spools of high quality sinterable green fiber as feedstock. Development of the fiber spinning process itself progressed faster than scheduled, using a substitute material as powder, but transferring this to Y-123 powder was slowed by the availability of high quality Y-123 in sufficient quantity. We have developed four different grades of Y-123 powder in kilogram quantities, and evaluated their behavior in the form of spun fibers. The present grade, which is satisfactory, became available in quantity during the third quarter.

The changes in the program activities also reflect new development activities arising from new and better ideas on how to make HTSC fiber and wire. The statement reflected the original plan to dry spin fibers, sinter and anneal in-line, and clad with copper by electroplating. This was aimed at a

HTSC composite wire consisting of a copper clad Y-123 monofilamentary fiber. The primary task of the AIResCo subcontract was to scale up the dry spinning process and design a pilot plant for dry spinning at CPSS. Early in the program, however, we developed a melt spinning process, yielding a better green fiber which could be produced using existing facilities at AIResCo. The dry spinning pilot plant design activity became unnecessary.

The wire design concepts also evolved to consider a multifilamentary wire in the form of a flexible ribbon, produced by cladding a flat braid of Y-123 filaments. The preferred cladding method is to solder bond the braid to a thin copper strip. The process plan is to melt spin Y-123 fibers, apply a thin silver coating (to make them wet solder), braid the green fibers into a flat belt, sinter and anneal in-line, and clad by soldering to copper strip.

The development of a convenient process of applying a silver coating then led us to the concept of a simpler style of Y-123 wire in which the silver coating was complete metallization. This would allow us to produce useful lengths of continuous HTSC wire before the base metal cladding process was completed, offsetting the higher cost of a noble metal cladding. This process plan is to apply a thicker silver coating, sinter, then anneal as a separate step, to make silver clad wire. This wire will be first made as a silver clad monofilament, but could be made as a multifilament using a loose yarn or a braided belt of silvered green fiber.

The following sections describe in detail the progress on the wire manufacturing task and the motor design task. Section 2 covers all aspects of the wire manufacturing development, incuding the fiber spinning work conducted at Albany International Research Corporation in Mansfield, Massachusetts, and

the Y-123 powder production, sintering, cladding, and characterization work conducted at CPS Superconductor in Milford, Massachusetts. Section 3 outlines the HTSC motor design activities at Emerson Motor Division in St. Louis, Missouri, and also has analyses of HTSC wire design by Mohamed Hilal of the University of Wisconsin, Madison, Wisconsin.

```
                1988          1989                    1990              1991
                J A S O N D J F M A M J J A S O N D J F M A M J J A S O N D J F M
                  1  |  2  |  3  |  4  |  5  |  6  |  7  |  8  |  9  | 10  | 11  |
                                             .
                                             .
                     CPSS                    .
                     lab scale               .
    FIBER            dry spin                .
    DELVP            [========]              .
                                             .
    original         AIRC dry spinning
    schedule          development        process development
                     [=================][=======================]
                                             .
                                             .
                                             .Dry spinning pilot line
                                      design      build        optimize
                                      [====][============][==========]

                  1  |  2  |  3  |  4  |  5  |  6  |  7  |  8  |  9  | 10  | 11  |
                                             .
                                             .
                     Rh-P dry                .
                     spin fiber              .
                     [======---]             .
                        CPSS dry spin fiber
    FIBER               [=================------
    DEVLP                                    .
                     BaTiO₃ melt spinning
                     [=====================------
    actual                                   .
    schedule             Y-123 melt spinning
                     [==================================]
                                             .
                                      .Green fiber braiding
                                      [=====================]
                                             .
                                             .
                  1  |  2  |  3  |  4  |  5  |  6  |  7  |  8  |  9  | 10  | 11  |
```

Figure 1.1      Above: Original Project Schedule for Fiber
                        Below: Actual Project Activities for Fiber

```
              1988         1989                    1990                   1991
              J A S O N D J F M A M J J A S O N D J F M A M J J A S O N D J F M
                1  |  2  |  3  |  4  |  5  |  6  |  7  |  8  |  9  | 10  | 11  |
              Lab                       .
              Sinter                    .
              [=======]                 .
TASK IC&ID                              .
                    sinter              .
                    continuous          .
WIRE                [========           .
                              Lab scale continuous
original                       sinter and plate
schedule            [=====================]
              Lab plate                 .
              [=======]                 .
                    contin.             .
                    plate               .
              [========                 .
                                        .
                                      Wire pilot line
                          [========================================

                1  |  2  |  3  |  4  |  5  |  6  |  7  |  8  |  9  | 10  | 11  |

              Lab sinter                .
              [======================--
                                        .
                          RTC furnace   .
                          [===========  .
WIRE                                    .
                                      Ribbon wire
DEVLP                                   .    ============================
                                        .
actual              Cladding module     .
schedule            Design and build    .
                    [================    .

              Silver coat and co-fire
              [=============================----------------------

                          Silver monofil wire
                          [=================================

                1  |  2  |  3  |  4  |  5  |  6  |  7  |  8  |  9  | 10  | 11  |
```

Figure 1.2    Above:  Original Project Schedule for Wire Tasks
              Below:  Actual Project Schedule for Wire Tasks

```
       1988          1989                        1990                    1991
       J A S O N D J F M A M J J A S O N D J F M A M J J A S O N D J F M
         1   |   2   |   3   |   4   |   5   |   6   |   7   |   8   |   9   |  10   |  11  |
                                              .
MOTOR          application                   .
DELVP            study                        .
               [═══════════════]              .
                                              .
               define properties   build test equip
               [════════════════][══════════════════]
                                              .
original                                     .test short
schedule                                      .  wire         test coils
                                              [═══════════][═══════════════════════]
                                              .
                                              .  design    fabr      test
                                              .  motor     motor     motor
                                              [═════════][═══════════][══════════════════]
                                              .
                                              .  design cryo
                                              [═══════════════]
                                              .  advanced motor design    build
                                              .       [══════════════════]════════════════]
                                              .
         1   |   2   |   3   |   4   |   5   |   6   |   7   |   8   |   9   |  10   |  11  |
MOTOR                application             .
DELVP                  study                  .
                       [═══════════]          .
                                              .
               define properties      .     build test equip
               [═══════════════════════════]   [═══════════════════]
                                              .
actual                                        .     test short
schedule                                      .        wire         test coils
                                              [═══════════][═══════════════════════]
                                              .
                                              .  design    fabr      test
   •                                          .  motor     motor     motor
                                     [═══════════════════════][═══════════][══════════════════]
                                              .
                                              .  advanced motor design    build
                                              .      [═══════════════════]════════════════]
                                              .
         1   |   2   |   3   |   4   |   5   |   6   |   7   |   8   |   9   |  10   |  11  |
```

Figure 1.3        Above:  Original Project Schedule for HTSC Motor Task
                  Below:  Actual Project Schedule for HTSC Motor Task

## SECTION 2

## WIRE FABRICATION

DAVID CHANDLER, ZONGYI CHEN, JOHN HALLORAN, JAMES HODGE,
LORI JO KLEMPTNER, MATTHEW NEAL, MARK PARISH,
VIREN PATHARE, AND RAYSHA PICERNO
CPS SUPERCONDUCTOR CORPORATION

GEORGE BAKIS, DANA EAGLES, WESLEY ISHIDA, AND STEPHEN TIERNAN
ALBANY INTERNATIONAL RESEARCH CORPORATION

**2.1        Introduction and General Comments**

In this section we report on all activities realated to the development of HTSC wire, from the underlying design philosophy of the fiber process for composite wire through raw materials, processing, and property characterization on the Y-123 filaments. The detailed progress reports for the three wire process steps of fiber production, sintering, and cladding are presented in Sections 2.2 to 2.4. Section 2.5 describes transport measurements on Y-123 filaments.

2.1.1   HTSC Wire Design

2.1.1.1      Composite Wire Design Philosophy

The strategy for producing practical wires from HTSC ceramics centers around the use of fine ceramic filaments in a normal metal matrix. In this regard, it is similar to traditional low temperature superconductor multifilamentary conductor designs.  However, the motivating factors influencing the use of fine ceramic filaments is different.  Low temperature superconductors favor fine filaments primarily to promote stability against

flux jumps, and to minimize AC losses[1]. A recent analysis by Collings[2] has shown that for $YBa_2Cu_3O_{7-\delta}$ at liquid nitrogen temperature, even macroscopically large filaments are intrinsically stable against flux jumps, so fine filaments are not as important, unless AC losses are a concern. However, in the case of HTSC materials, fine ceramic filaments are necessary for mechanical reasons if the brittle ceramics are to be used like conventional flexible wires.

A brittle ceramic HTSC filament will be flexible if it is small enough that the elastic strains due to flexing will be too small to damage the superconducting ceramic. If the filament is exactly at the mechanical neutral axis of a wire, the maximum elastic tensile strain suffered by the filament can be calculated from simple beam theory. The minimum bending radius, R, which a filament of diameter, D, can withstand is related to the maximum tolerable tensile strain, $\epsilon_m$, by:

$$2.1) \qquad R = D/(2\epsilon_m)$$

If Young's modulus, E, of the HTSC is known, this can be expressed in terms of a tolerable tensile stress, $\sigma_m$, for a chosen probability of fracture:

$$2.2) \qquad R = ED/2\sigma_m$$

Flexibility demands fine diameter filaments. If the Y-123 can only tolerate a strain $\epsilon = 0.0005$, a filament diameter of 50 microns is required for wire with a one-centimeter bending radius.[3]

---

[1] E.W. Collings, _Applied Superconductivity, The Metallurgy and Physics of Titanium Alloys_, 2, Applications, Plenum Press, NY, 1986

[2] E.W.Collings, "Design Considerations for High $T_c$ Ceramic Superconductors," presented at the MRS International Meeting, Tokyo, May 30, 1988, to be published in _Cryogenics_

[3] It is more convenient to express the properties of Y-123 in terms of strain, since the elastic modulus of Y-123 is irreproducible. See R. E. Loehman et al., J. American Ceramic Soc., 72,(4),669-674, (1989)

Tensile stresses generated upon flexure can also be partially compensated for by any compressive pre-stress that might be exerted on the ceramic filaments by the metal cladding. The thermal expansion difference between $YBa_2Cu_3O_{7-\delta}$ and the metal matrix can be used to generate a desirable axial compressive stress in the $YBa_2Cu_3O_{7-\delta}$ filament, $\sigma_r$, which is proportional to the thermal expansion mismatch:

$$2.3) \qquad \sigma_r \quad \delta\alpha\delta T\Gamma$$

where $\delta\alpha$ is the difference of the thermal expansion coefficients for the metal and the superconductor, $\delta T$ is the temperature difference upon cooling, and $\Gamma$ accounts for wire geometry and relative moduli. (An explicit form for the monofil wire will be given later.) This compressive stress can be significant, since a copper cladding can generate 0.51 MPa/°C, aluminum 0.76 MPa/°C and silver 0.6 MPa/°C. This is sufficient to cause plastic deformation in the metal by creep at high temperatures or yielding at low temperatures. The actual value of residual stress useful for strengthening the wire will be determined by the creep and plastic deformation behavior of the cladding.

2.1.1.2    Wire Designs

Two types of wire designs are under development, a monofilamentary wire and a multifilamentary ribbon wire. These are illustrated in Figure 2.1.1. The monofil wire, a simple metal clad Y-123 fiber is similar to the original concept with a co-fired silver alloy cladding replacing the electrodeposited copper. The ribbon is designed to have many Y-123 filaments located near the mechanical neutral axis to give the benefits of a multifilamentary wire without compromising flexibility.

copper          YBCO



Silver
Alloy

YBCO
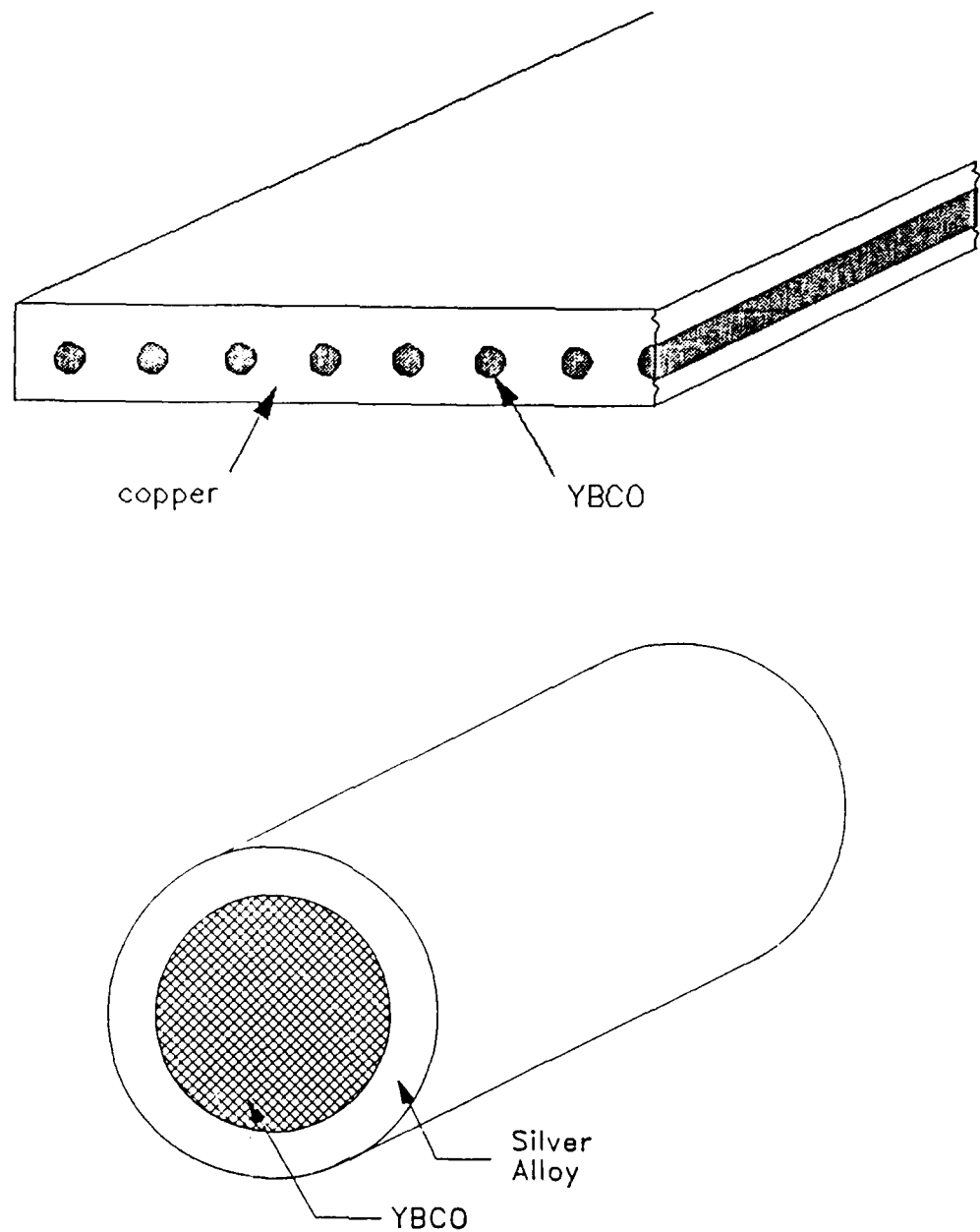
Figure 2.1.1          Top: Schematic of the Flexible Ribbon Conductor
                      Concept Illustrating an Array of Fine Superconductor
                      Filaments in a Normal Metal Cladding

                      Bottom: Silver Clad Monofil
                      Wire.

### 2.1.1.3    Monofilamentary silver clad wire

The monofil wire is fabricated by coating a Y-123 green fiber with a silver alloy powder dope and co-firing.  The relative amount of metal and Y-123, expressed as the metal/superconductor ratio, M, is the major design parameter for the monofil wire.  Its value is a compromise between mechanical properties, which improve with metal thickness, and dilution, cost, and the oxygen annealing time, for which thinner metal layers are prefered.  For a monofil wire with a HTSC core of diameter $d_{sc}$ and the outer wire diameter $d_{Ag}$, M is given by:

$$2.4) \quad M = (d_{Ag}/d_{sc})^2 - 1 \quad - A_{Ag}/A_{sc}$$

where $A_{Ag}$ and $A_{sc}$ are the cross sectional areas of the silver alloy and the superconductor.

The tensile properties of the wire can be modeled by determining the relationship between a tensile load applied to the composite wire, P, and the actual tensile strain suffered by the HTSC core, $\epsilon_{sc}$.  If we accept some value, $\epsilon_{max}$ as the maximum tensile strain which the ceramic can safely bear (say 0.0005), then the maximum tolerable tensile load $P_{max}$ can be calculated.

The elastic strain in the HTSC core is the combination of the applied elastic strain and the elastic strain resulting from residual stresses in the silver cladding.  This can be expressed in terms of the fraction of the applied load born by the HTSC core, $P_{sc}$, and the residual stress in the silver cladding, $\sigma_r$, as:

$$2.5) \quad \epsilon_{sc} - \epsilon_{sc,appl} + \epsilon_{sc,r} - P_{sc}/[A_{sc}E_{sc}] + \sigma_r M/E_{sc}$$

where $E_{sc}$ is the elastic modulus of the superconductor.  The load in the superconductor is related to the total load, P,   e metal/superconductor

ratio, M, and the relative elastic modulus of the cladding and the superconductor, $G=E_{Ag}/E_{sc}$ by:

$$2.6) \quad P = P_{sc}(1+MG)$$

Combining (2.5) and (2.6) gives an expression for the maximum tensile load that the composite wire can withstand:

$$2.7) \quad P_{max} = [\epsilon_{max} - \sigma_r M/E_{sc}]A_{sc}E_{sc}[1+MG]$$

This expression shows how the load tolerance increases with the metal/-superconductor ratio and the relative modulus. Notice that load tolerance of the wire directly depends upon the amount of residual stress. This residual stress arises primarily from the thermal expansion difference between the silver and the HTSC, and will be compressive on the ceramic and tensile on the metal, in the case of cooling. (A compressive stress means that $\sigma_r$ is negative in Equation 2.7). To be able to estimate the strength of the composite wire, one must understand the magnitude of the thermomechanical residual stress.

Cooling the composite wire from the sintering temperature will create $\delta\alpha\delta T$ thermal stresses, placing the ceramic core in compression. This can be modeled elastically by equating the axial strain in the core and the alloy clad. This strain involves both thermal strain ($\alpha_i\delta T$) and elastic strain:

$$2.8) \quad \alpha_{sc}\delta T + (\sigma_{sc}/E_{sc}) = \alpha_{Ag}\delta T + (\sigma_{Ag}/E_{Ag})$$

Now the stresses in the two materials are related, since each bears equal but opposite loads, i.e., the alloy bears a tensile load, P, while the core carries a compressive load (-P):

$$2.9) \quad \alpha_{sc}\delta T - (P/A_{sc}E_{sc}) = \alpha_{Ag}\delta T + (P/A_{Ag}E_{Ag})$$

One can solve for the load and express the tensile stress in the alloy as:

2.10) $\sigma_{Ag} = P/A_{Ag} = \dfrac{E_{Ag}(\alpha_{sc} - \alpha_{Ag})\delta T}{[(A_{Ag}/A_{sc})(1/E_{sc}) + (1/E_{Ag})]}$

This can be written more neatly in terms of the metal/superconductor ratio, M, and relative elastic moduli, Y:

2.11A) $\qquad \sigma_{Ag} = \{E_{Ag}(\alpha_{sc} - \alpha_{Ag})\delta T\}\{MY+1\}^{-1}$

Similarly, the compressive stress in the HTSC core is given by:

2.11B) $\qquad \sigma_{sc} = -\{E_{sc}(\alpha_{sc} - \alpha_{Ag})\delta T\}\{1 + Y/M\}^{-1}$

Notice that 2.11A and B are simply the thermal mismatch $E\delta\alpha\delta T$ term modified to consider geometry and relative moduli.

These equations are elastic, so cannot take into account plasticity effects. Plasticity certainly comes into play during cooling, since the strains exceed the elastic limit. For example, examine the magnitude of the thermal mismatch stress term for the silver:

$$E_{Ag}(\alpha_{sc} - \alpha_{Ag}) \approx 0.6 \text{ MPa/°C}$$

Cooling from 900°C to room temperature without yielding would induce more than 70,000 psi stress in the alloy. This is greatly in excess of the plastic yield stress, so obviously the silver flows during cooling. Furthermore, one should expect the cladding to creep during cooling and during the long 500°C oxygen anneal, reaching a zero stress condition. One must consider the kinetics of stress relaxation to estimate the retained residual stress. Also, upon cooling to liquid nitrogen, thermal mismatch strains will probably cause yielding in the alloy. This may be a problem. Cycling between room temperature and 77°K might cause mechanical hysteresis, eventually placing the ceramic core in tension. This will be the case for any clad HTSC wire, so the mechanical metallurgy of these metal-HTSC composites needs attention.

Now consider relaxation of thermal mismatch stresses in silver clad wire. Much of the stress is developed at temperatures where the metal can rapidly creep, which will relax away a portion of the stress. (Here we are just considering the silver cladding, which is bonded to the ceramic at the sintering temperature. Creep relaxation will also play a role in the ribbon wire, since the solder will readily creep at lower temperatures.) To estimate the level of residual stress, we have to know at what temperature stress relaxation is slow enough to "freeze in" the thermomechanical stresses.

Stress relaxation is also important during oxygen intercalation of silver clad Y-123 filaments to accommodate the volume decrease associated with the tetragonal-orthorhombic transformation. If the silver cannot creep as the ceramic contracts the fiber will suffer radial tension so it is likely to degrade by microcracking.

Creep in silver is well documented so data is available to calculate approximate relaxation rates. The creep data of Ghosh and Mitra[4] can be fit to a stress relaxation law to express the time dependent stress, $\sigma$, in terms of the initial stress, $\sigma_i$, and kinetic constants:

2.12) $\quad \sigma^{1-n} = \sigma_i^{1-n} + (4B(n-1)G^{1-n})t$

where G is the shear modulus ( 15 GPa for Ag), n is the stress exponent for the plastic strain rate (4.7 for Ag in this range), and B is the creep kinetic constant derived from Ghosh and Mitra's data. The value of B is:

2.13) $\quad B = 1.9*10^{19}/\text{sec} * \exp(-28.3\text{kcal}/RT)$

Stress relaxation is very rapid in silver at the oxygen intercalation temperature range. Above 700°C stress relaxation occurs in

---

[4] R. N. Ghosh and S.K. Mitra, Metal Sci. <u>17</u>, Dec. 1983, p.590

seconds, so the thermal mismatch stresses during cooling from sintering temperature should be dynamically relaxed. Most of the stress relaxes away in about a minute at 500°C, so any thermal mismatch stress in the silver is removed during the oxygen intercalation anneal and the volume contraction of the Y-123 core caused by oxygen intercalation and tetragonal-orthorhombic transformation should be easily accommodated. Relaxation at 300°C is slow enough to preserve thermomechanical stresses during a rapid cool from intercalation temperature to room temperature.

It is possible to estimate the room temperature residual stress. Starting from zero stress after intercalation, thermomechanical stress builds up from around 300°C or so, depending upon cooling rate. If unrelieved, this stress builds up at a rate around 0.6 MPa/°C, which is more than enough to cause plastic yielding. So the upper limit of residual stress in the silver is approximately the same as the room temperature yield stress,[5] which is about 30 MPa for pure Ag or 50 MPa for 20% Pd.[6] A silver-clad filament 100 microns in diameter could therefore tolerate a tensile load, P, of 0.47 N (or 48 grams) before the Y-123 core experienced any tensile strain, and a load of 114 grams at a tensile strain $\epsilon = 0.0005$.

## 2.1.2 Multifilamentary Ribbon Wire

The CPSS ribbon wire design incorporates an array of fine ceramic filaments located at the mechanical neutral axis of a composite ribbon. The

---

[5]. This is a conservative estimate. The stress state in the metal coating is biaxial, so yielding requires larger principal tensile stresses than in the case of uniaxial stress states. The yield strength data is for uniaxial loading.

[6]. T. Maruno, et al., J. Japanese Institute of Metals, 47, (9), pp. 768-775, (1983)

array is preferably a flat braid with complete transposition of filaments to assure an identical electromagnetic enviroment for all filaments. In the case of the ribbon conductor, the cladding method involves solder bonding the Y-123 filaments to copper metal strips. The metal/superconductor ratio for a ribbon with filaments of diameter D and center-to-center spacing W, in a ribbon of thickness, t,:

$$2.14) \qquad M = 4tW/\pi D^2 - 1$$

The practical handling of the ribbon may also play a role in specifying M for the ribbon conductor. If very tight bending radii are specified, very fine filament diameters may be required. This in turn may require a higher M to prevent the ribbon thickness from becoming too small to handle conveniently as a single ribbon wire. It may be necessary to adopt tows of fine ribbons with individual wires bound sufficiently loosely such that each wire is able to respond independently to flexure.

The ribbon design presently being considered is based on preparing bare superconducting filaments that are subsequently clad with metal in a separate step at temperatures below the oxygen intercalation anneal temperature. This is primari˙ motivated by the need to anneal $YBa_2Cu_3O_{7-\delta}$ after sintering to restore the superconducting orthorhombic phase, and secondarily to permit the use of base metals such as aluminum or copper, that are chemically reactive with $YBa_2Cu_3O_{7-\delta}$ at high temperature. A further advantage of bare filament sintering is that the sintering heat treatment can be optimized for the $YBa_2Cu_3O_{7-\delta}$ ceramic, since it is being treated in isolation. This contrasts with a cofiring approach, where the ceramic is sintered along with the metal cladding; the heat treatment schedule being some

compromise between what optimizes the ceramic and what is best for the metallization.

2.1.3     Raw Material: Y-123 powder production

Rapid sintering demands highly sinterable Y-123 powder as raw material.  It was necessary to develop a process to produce high quality powder in kilogram quantities.  The first task was to scale up a previously developed solid state synthesis method to make phase pure calcined powder. Capacity for calcined powder was increased gradually up to the present level of about 10 kilograms/week, which is adequate to supply the program.  To date, 23 lots of Y-123 powder totaling about 25 kilograms have been supplied to AIResCo for use in fiber spinning.

The phase purity of the powder is a least 98 wt% Y-123, as determined by quantitative x-ray diffraction.  Figure 2.1.2 shows Cu-$K_\alpha$ XRD patterns for a typical lot of powder after milling.  The lower pattern, Figure 2.1.2B shows the low intensity peaks on a scale so that the 5% (012) peak of Y-123 is full scale.  The (111) peak of $BaCO_3$, which is the most intense barium carbonate line, is present at a relative intensity of 0.5%. By comparison with mixed powder standards, this relative intensity corrosponds to about 0.4 wt% barium carbonate. The $BaCuO_2$ (600) peak is detected at a relative intensity of 1%, corrosponding to about 0.5 wt% of this phase.  There is also a 1% intensity peak identifiable as the (101) $Y_2BaCuO_5$ line.  The

presence of minor amounts of these phases has been confirmed by Allied-Signal[7] and the University of Minnesota[8].

Several methods were evaluated for milling the calcined Y-123 to produce a fine powder. Several kilogram lots of powder were dry ball milled to produce a powder with median particle size around 2.5 microns. This powder was used for a number of green fiber experiments. Later it was discovered that stearic acid, used as an anticaking aid during dry ball milling, reacted violently with Y-123, causing severe problems during binder burnout. These reactions were avoided using ethylene glycol as a milling aid, but the particle size was only 3.7 microns, making this grade of powder unsatisfactory. Jet milling was identified as the preferred method of comminution.

The jet milled powder has been adopted as the standard since it produced the finest particle size and most consistent surface area. Figure 2.1.3 shows the morphology of the Y-123 particles. Table 2.2.1 lists the major characteristics of eight lots of powder. The median particle size is consistantly around 1.6 ± 0.2 microns, and the BET surface area[9] is repeatedly around 2.5 ± 0.3 $m^2$/gm. The weight fraction finer than one micron, as determined by centrifugal sedimentation[10], varies from 23-26%. The

---

[7]. Analyses kindly provided by T.J. Barder, Engineered Materials Research Center, Allied Signal Corporation

[8]. Data courtesy of Professor M. Mecartney, University of Minnesota

[9]. Surface area derived from multipoint nitrogen BET adsorption isotherm determined with an Autosorb-6, Quantichrome Corp., Syosett, NY

[10]. Horiba CAPA 700 Centrifugal Particle Size Analyser, using as the suspension medium "Sedisperse A-13", a non-polar hydrocarbon fluid from Micromeritics, Norcross, GA

cumulative particle size distribution for a typical lot is shown in Figure 2.1.4. The distribution is very narrow for a milled powder. About 90% of the particles lie between 0.5 and 3.5 microns in equivalent spherical diameter. The maximum particle size is 4 ¬icrons.

The chemical composition of the Y-123 powder has been analyzed by several laboratories. Two other DARPA contractors have reported the analytical results on our powder. Induction coupled plasma (ICP) spectrochemical data, normalized to yttrium, established the atomic ratios Y/Ba/Cu to be 1/1.9./2.89 at the University of Minnesota and 1/1.93/3.01 at Allied Signal. The total carbon contents of three samples was determined by LECO analyis[11] to be 0.24 wt%, 0.21 wt%. and 0.20 wt%. An independend LECO analyis at Allied Signal indicated 0.27 wt% carbon. The major metallic impurity in the Allied Signal sample was reported to be 98 ppm zirconium, while the University of Minnesota result was about 300 ppm aluminum.

TABLE 2.1.1

CHARACTERISTICS OF JET MILLED Y-123 POWDERS

| POWDER LOT | MEDIAN DIAMETER (micron) | SUBMICRON FRACTION (wt.%) | SURFACE AREA ($m^2$/gm) |
|---|---|---|---|
| 02394 | 1.6 | 29 | 2.7 |
| 03033 | 1.7 | 23 | 2.7 |
| 03025 | 1.7 | 24 | 2.5 |
| 03029 | 1.5 | 26 | 2.7 |
| 03030 | 1.6 | 25 | 2.5 |
| 03006 | 1.7 | 27 | 2.3 |
| 03018 | 1.8 | 23 | 2.3 |
| 02326 | 1.7 | 25 | 2.8 |

---

[11]. Galbraith Laboratories, Knoxville, TN

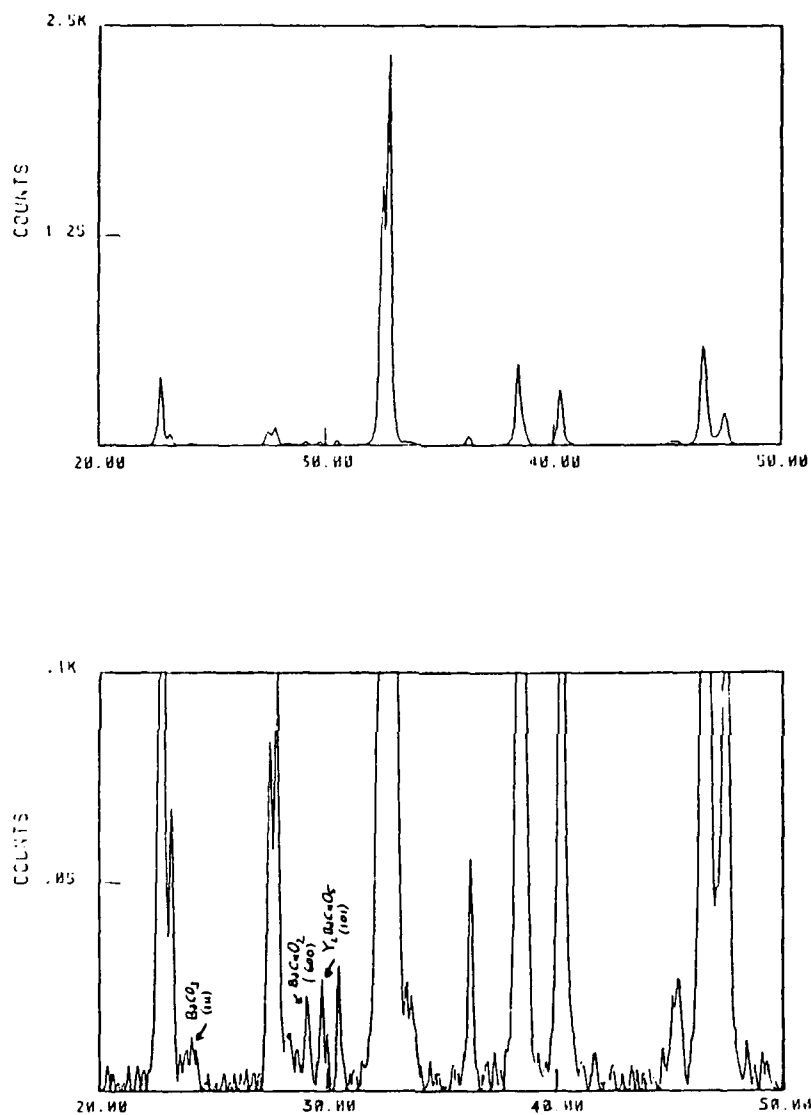Figure 2.1.2    X-Ray Diffraction Pattern of Y-123 Powder Lot # 1303
                Above: Major Peaks of Y-123
                Below: Low Intensity Peaks from Impurity Phases
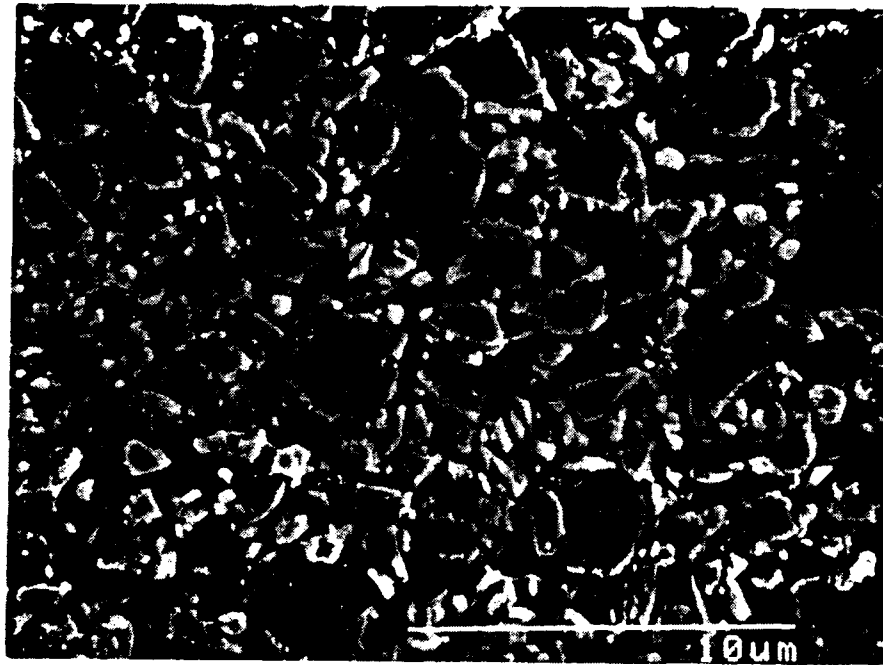
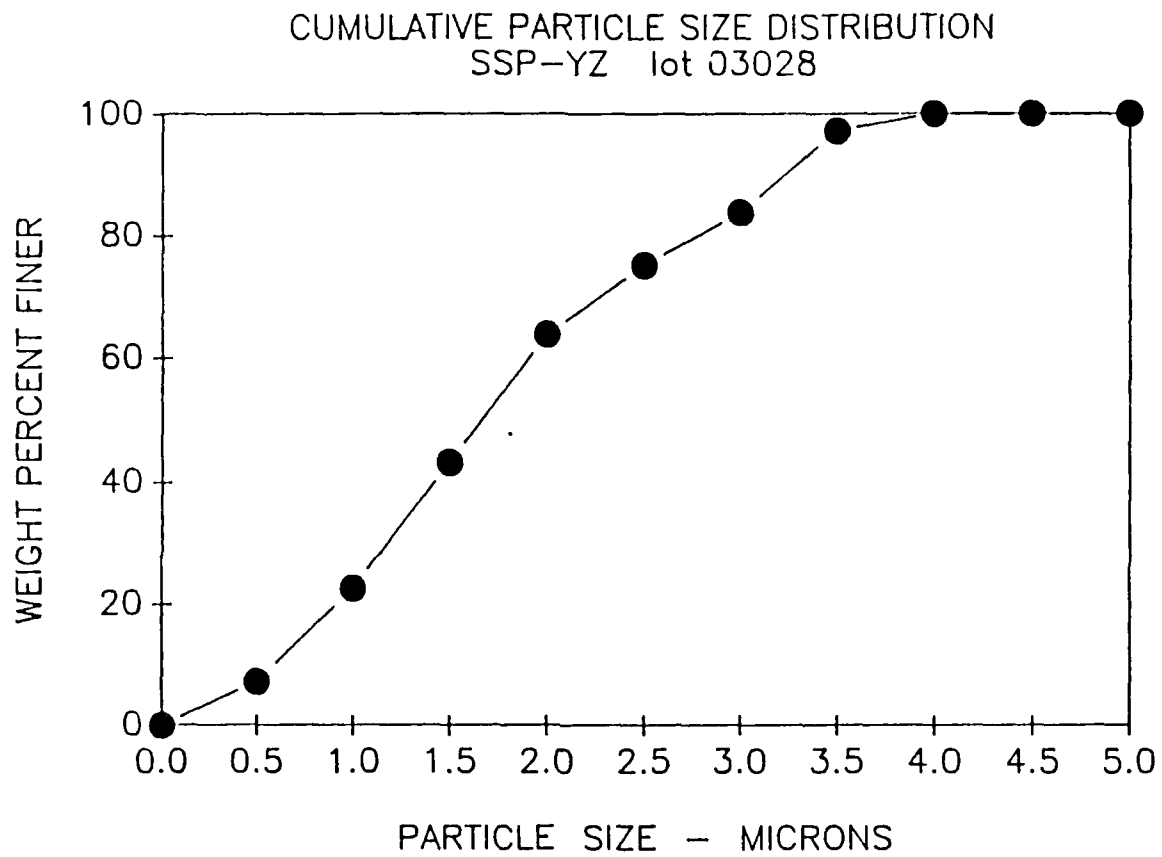Figure 2.1.3    Morphology of Jet Milled Y-123

CUMULATIVE PARTICLE SIZE DISTRIBUTION
SSP–YZ   lot 03028



Figure 2.1.4      Cumulative Particle Size Distribution of Jet-Milled Y-123
Powder by Centrifugal Sedimentation

## 2.2      Fiber Preparation

### 2.2.1      Introduction

High quality Y-123 green fibers are essential to this program. There are many stringent requirement for these fibers. First the fibers must be easily manufactured and have adequate physical properties in the green state. The fiber must have a fine diameter, ultimately as fine as 10 microns, yet still be strong and tough enough as a monofilament for spooling, treating with the silver coating, and handling on machinery to produce braided belts of silver coated fibers. These textile characteristics must be achieved with minimal carrier polymer and maximum Y-123 powder loading. Secondly, the green fibers must produce high quality Y-123 ceramic filaments upon firing. They need to be well behaved during binder burnout and sintering. The carrier polymer must burn out cleanly with no carbonaceous residue. There must be no reaction between the polymer or its pyrolysis products and the easily-reduced Y-123 compound. The green fibers must have good dimensional stability, and have no shrinkage or swelling during heating, as this causes fiber breakage during continuous sintering. The fibers must have good shape retention so there is no slumping during sintering. Finally, they must produce a good, well sintered ceramic capable of high critical current density.

The dry spun fibers developed at CPS in the beginning of the program had fine diameters, good dimensional stability, and sintered well, but otherwise had poor strength and physical properties. Most importantly, the dry spinning process is more difficult to control for continuous manufacture.

At the beginning of the subcontract with Albany International Research Company, melt spinning was proposed as an alternative to dry spinning. At that time we did not know if it would be possible to melt spin polymers with ceramic solids loading as high as 50 vol%, but the manufacturing advantages of melt spinning warranted an attempt. Fortunately, the AIResCo researchers quickly obtained encouraging results, and melt spinning has been established as the preferred method. Dry spinning is now used only to produce fiber from small quantities of experimental powders, since it requires only 30-100 grams of powder.

All melt spun green fiber development and production is done at AIResCo, using Y-123 powder made at CPSS as raw material. AIResCo develops the carrier polymer systems and methods for compounding, spinning, handling, and braiding the green fibers. Thermal analyses and physical properties are determined at AIResCo. The Y-123 green fibers are evaluated at CPSS for their behavior as raw material for Y-123 wire, principally focussing on firing characteristics and related problems. AIResCo's demand for Y-123 powder, paced by the fact that melt spinning requires about one kilogram of powder per batch, was an important spur for the development of pilot scale powder production at CPSS. About 40 types of green fiber, with different combinations of powder type, polymer blend, and spinning conditions, have been produced and evaluated. This includes more than 10 different classes of polymer tested with either barium titanate or one of four different grades of Y-123 powder.

2.2.2     Dry spinning development

Early in the program all Y-123 green fibers were prepared by a dry spinning process in which a "spin dope"- consisting of Y-123 powder, polymers, and solvents- is extruded in a drying column of a simple laboratory scale apparatus. Fibers were spun continuously, but collected in 30-100 cm lengths. The apparatus included a syringe-type dispenser to deliver the dope, a spinnerette, a drying column, and a take-up reel. After compounding, the dope was loaded into the syringe and forced at a uniform rate through the spinnerette. The extruded stream of dope underwent significant elongation under the force of its weight until the fiber dried enough to be rigid. The fiber diameter could be controlled between 20 and 200 microns, depending upon dope rheology, spinnerette size, and the solvent evaporation rate. The dried green fibers had solids loadings of up to 55 vol% ceramic.

The dry spinning dopes were formulated with acrylic resins to provide clean burnout at temperatures as low at 500°C. The polymer fraction was a mixture of a $10^6$ molecular weight acrylic to provide strength and a lower molecular weight acrylic with hydroxyl functionality, which could be cross-linked with a melamine-formaldehyde agent. The extent of the cross-linking reaction dominated the rheology and "spinnability" of the dope. The dope formulations also included a plasticizer, a toluene-methylethylketone-xylene solvent mixture, and sorbitan trioleate as dispersant for the ceramic powder. These materials were typically mixed with 75-80 wt% $YBa_2Cu_3O_{7-\delta}$ powder and agitated until the cross-linking reaction rendered the material "spinnable." The development of the dry spinning dope formulations and process is documented in detail elsewhere[12].

---

[12] "Composite Ceramic Superconducting Filaments for Superconducting Cable," ONR Contract N00014-87-C-0789, Final Report, 12 July 1988

The initial plan was to futher develop the dry spinning process and construct a pilot plant. However, it was realized that dry spinning is not a desirable process for fiber manufacture. A commercial scale operation requires a recovery system to collect the organic solvents driven off during fiber drying. Fiber formation is very sensitive to the rheology of the ceramic-polymer spinning dope, which depends on variables such as mixing and aging time. Also, the drying fibers have little strength, so the spin line breaks easily, making it difficult to produce continuous monofilaments. We decided to attempt to produce green fibers with the more manufacturable process of melt spinning.

## 2.2.3    Melt spun fiber fabrication

A melt spinning process avoids many of the problems associated with dry spinning. In melt spinning, a thermoplastic polymer is melted, extruded through a spinnerette, and drawn in a cooling column. Melt spinning is common in textile fiber applications, while dry spinning is used only for difficult polymers that cannot be melt processed. During the first quarter, a program was undertaken to explore the possibility of developing a melt spinning process with Y-123 solids loadings of up to 50 vol%.

Three critical criteria were defined for green fiber fabrication: 1) complete burnout of the polymer system below 500°C, 2) non-reactivity of the polymer with the ceramic powder, and 3) shape retention of the ceramic fiber upon binder burnout. To meet the first two criteria, the candidate polymer systems could not contain any elemental nitrogen or chlorine and had to burn without charring. To meet the shape retention criterion, polymers

with different burnoff temperatures, crosslinkable polymers, and formulations with different ceramic loadings were to be evaluated.

Several grades of seven different thermoplastic polymers were chosen for the initial study. These were: high density polyethylene (HDPE), polypropylene (PP), polyoxymethylene (celcon), polypropylene carbonate (PPC), ethylene vinyl acetate (EVA), polymethylmethacrylate (PMMA), and polyether ether ketone (PEEK). These polymers were evaluated for their suitability as carrier polymers for green fibers. This included the burnout behavior, reactions with Y-123, ease of compounding and spinning, and suitability of the green fibers during sintering. The evaluation required considerable effort, but will only be briefly reviewed below.

Thermal gravimetric analysis (TGA) of candidate polymers was performed both in nitrogen and air for neat polymer and polymer-Y-123 mixtures. Figure 2.2.1 shows some of the TGA data for neat polymers in air. The burnout range was satisfactory for all polymers except PEEK, which is a polymer that resists thermal degradation. The PPC, PMMA, and celcon had attractive burnout characteristics, but could not be successfully compounded at 50 volume percent loading. The two best polymer candidates were HDPE and PP.
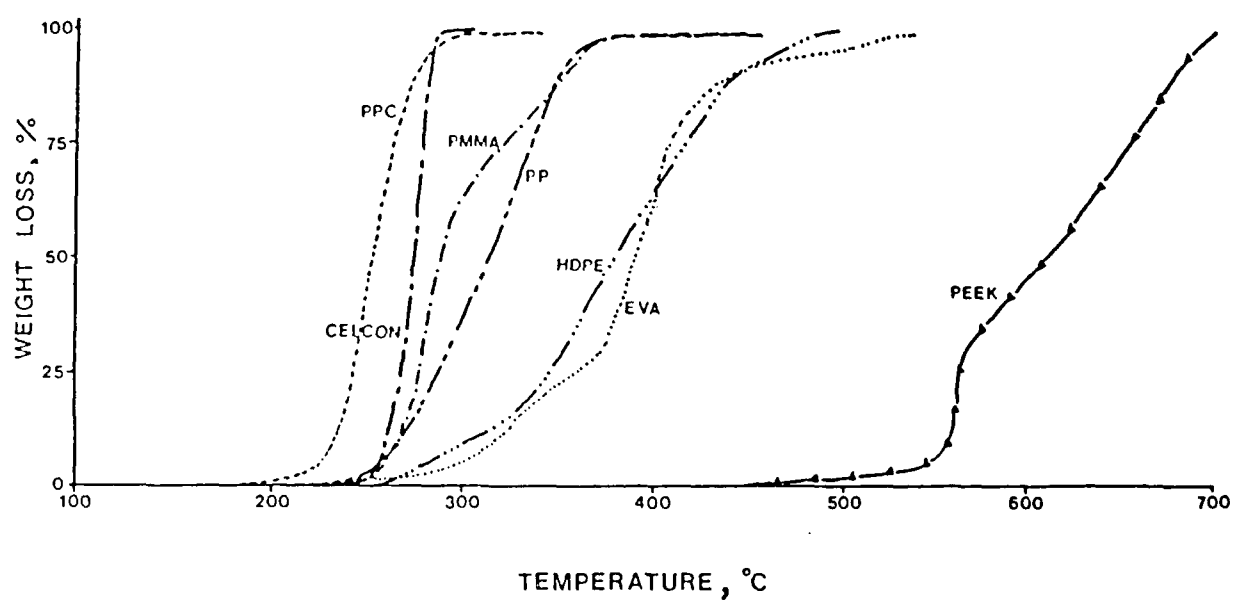
Figure 2.2.1     TGA of Candidate Polymers in Air

Initial melt spinning experiments used small quantities of a relatively crude Y-123 powder compounded at 10 and 30 vol% and extruded with a small CSI mixing extruder.[13] Conventional screw extruders were used for higher solids loadings. These extruders required larger batches containing nearly a kilogram of ceramic powder. This exceeded our capacity for Y-123 powder at that time, so barium titanate[14] was used as a surrogate powder. This proved to be a convenient substitute, and many experiments were performed with barium titanate. Even now we evaluate new spinning compositions with barium titanate since it is much less expensive than Y-123 powder.

The first experiments with 50 vol% $BaTiO_3$-50 vol% polymer prepared with HDPE and PP showed loss of flow during extrusion. It was necessary to add a processing aid into the blend, which is believed to act as a lubricant during compounding and extruding. After many experiments, successful fibers were prepared using polypropylene (PP), ethylene vinyl acetate copolymer (EVA) and high density polyethylene (HDPE). These are adequately strong and can be easily handled. The HDPE tends to be stronger, the PP more easily drawn to fine diameters, and the EVA fiber is much more elastomeric. The EVA was eventually dropped due to its reactivity during binder burnout.

Typical spools of melt spun Y-123 and barium titanate green fiber are shown in Figure 2.2.2. In most cases the spools have several hundred meters of fiber, which is plenty for evaluation of experimental fibers. In principle, the length is limited only by batch size. In practice those spin

---

[13]. Custom Scientific Instruments, Inc., Cedar Knolls, New Jersey 07927

[14] TICON-HPB, a barium titanate powder with specific surface area 2.9 $m^2/gm$, median particle size 1.2 $\mu m$. TAM Ceramics, Inc., Niagara Falls, NY

runs which are not intentionally stopped are terminated by problems, typically clogging of the die or pressure buildup in the extruder. The longest continuous melt spun fiber made to date is about 0.75 kilometer long.

Fiber diameter reduction

The diameter of the green fiber is determined by three factors: 1) die diameter; 2) spin draw, which is drawing of the hot extrudate during the spinning operation; and 3) post draw, which is a secondary drawing of the cold fiber.

Post draw would be an ideal method of diameter control for a variety of reasons. Fiber diameter can be significantly reduced by post draw, while the tensile strength and modulus increases due to improved orientation of the polymer molecules. It is also a convenient way to produce material with a variety of diameters from a single stock of as-spun fiber. Figure 2.2.3 shows a 100-micron barium titanate/HDPE fiber after post drawing to 410% elongation. The obvious elongation of the polymer orients the HDPE and promotes crystallization. Unfortunately, the polymer orientatation causes a dramatic shrinkage of the fiber during heating, as polymer segments relax to more random orientations. In some cases, heated fibers shrank more than 50%, with the diameter increased nearly to the as-spun diameter.
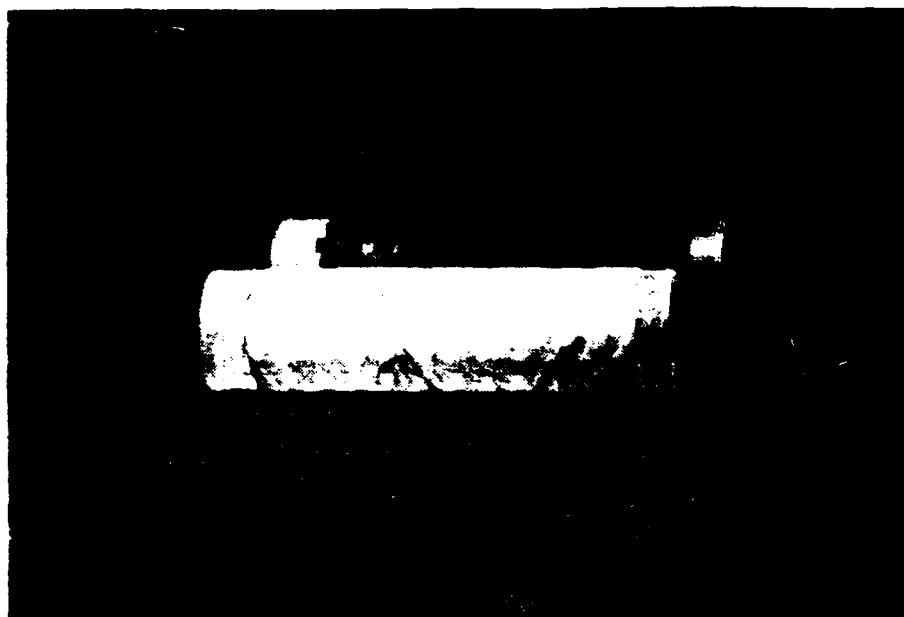
Figure 2.2.2       Typical Spools of Y-123 and Barium Titanate Green Fiber ⁻ ɔduced by Melt Spinning
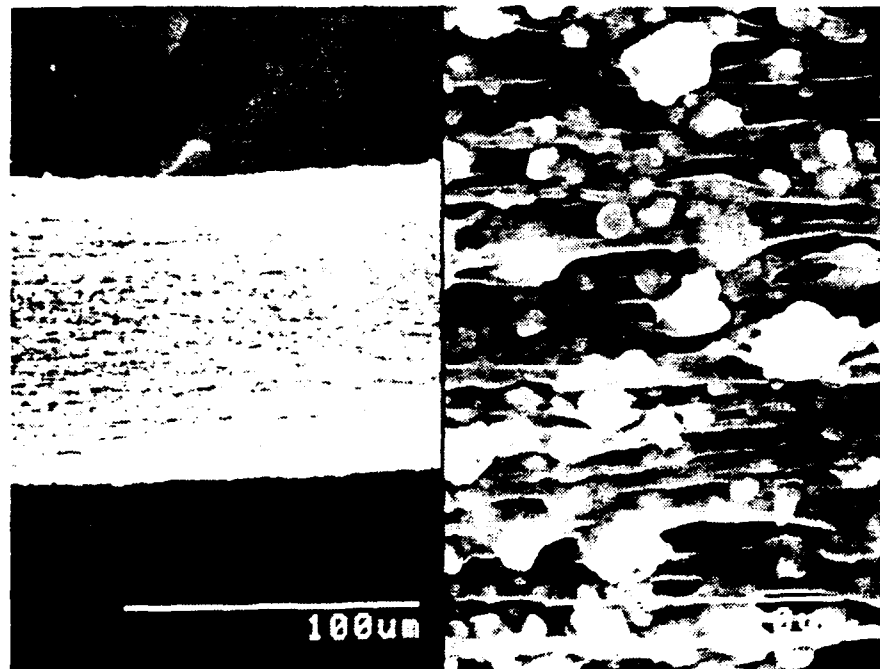
Figure 2.2.3    Barium Titanate/HDPE Green Fiber after Post
Drawing

This is not acceptable for green fiber which is to be sintered. Several attempts were made to combat the shrinkage. A series of PP-based fibers were post-drawn at 150°C to determine if hot drawing reduced orientation, but this did not alleviate the shrinkage problem. Two spinning experiments were conducted with amorphous polymers in the hope that these would have less orientation. Atactic polypropylene (a-PP) could be spun into fibers, but these were too tacky and easily deformed. An ethylene propylene rubber (EPR) resin was found to be a good fiber former at 50 vol% with barium titanate, producing a highly elastomeric green fiber. Unfortunately the fiber was too weak to post-draw. Finally, an attempt was made to radiatively cross-link the drawn fibers to prevent relaxation. A variety of green fibers were exposed to 10 megarads of 165 keV electrons at Energy Sciences, Inc. of Woburn, MA, but this treatment was not effective. For the present, we have rejected post-drawing as a technique to reduce green fiber diameter.

Spin-drawn green fibers do not have as severe a problem with relaxation shrinkage, since the elongation occurs near the melting point of the polymer. The as-spun fiber diameter/die diameter ratio is determined by the spin draw. The degree of spin drawing which the fiber can tolerate without breaking depends upon the melt strength of the powder-polymer blend. Melt strength is difficult to predict. We have found that it varies significantly with the batch composition, polymer grade, lubricant content, and type of Y-123 powder. For example, HDPE based fibers prepared from 3.7 micron Y-123 powder (made by ball milling with ethylene glycol) could be spin-drawn to a draw ratio of 4, but the same fiber composition made with 1.7 micron jet milled Y-123 powder could barely be drawn. It is not yet clear if

this is due to the higher surface area of the jet milled powder, or if it is an effect of surface chemistry. The spin draw of jet milled Y-123/HDPE blends could be improved by increasing the lubricant content, but these fibers had unsatisfactory binder burnout behavior.

Polypropylene-based fibers made with jet-milled powder had much better spin draw. Fibers as fine as 50 microns could be drawn from a 343 micron die. These are the finest melt spun Y-123 fibers prepared to date. Unfortunately, PP-based green fibers were found to have unsatisfactory shape retention, and tended to flatten at contact point with the setter upon sintering. Several attempts were made to alleviate this problem, without success. Because of this, polypropylene is no longer a candidate carrier polymer.

At present, we are producing fine diameter green fibers without draw from HDPE/Y-123 blends by using very fine diameter dies. The 125 micron green fibers now routinely used for coating and sintering are made directly from 125 micron dies. A limited quantity of 50 micron fiber has been spun from a 50 micron die, but this fiber is too fragile to handle conveniently.

### Mechanical properties of green fiber

The tensile properties of the green fibers were routinely determined to assess the tensile strength, tensile elastic modulus, and elongation at break. The tensile strength of Y-123 green fibers typically varied between 7 and 14 MPa (although one post drawn fiber from ball milled Y-123 exceeded 100 MPa). There is no simple relationship between the strength of the neat polymer and the 50 vol% green fiber. The elastic modulus varies more widely than the tensile strength and is sensitive to drawing, reflecting the

influence of polymer orientation. Elongation at break is also highly variable. Some fibers are very brittle, while others elongate more than 100% before breaking. The green fibers spun from EPR were rubbery.

The practical handling behavior of the monofilaments during spooling or braiding depends more on the breaking load than the tensile strength. Figure 2.2.4 shows data for recent green fibers made from the jet milled Y-123 powder as a plot of breaking load and break elongation versus fiber diameter. Most of the load-diameter data lie in a band corrosponding to $9 \pm 2$ MPa, so the main determinant of breaking load is the diameter. The lower limit of tensile load for handling for unwinding and coating is currently around 20 grams, and the fibers finer than 125 microns (5 mils) are presently too weak to survive this handling. Finer fibers will have to be handled as multifilamentary tows. Elongation is important if the green fiber is to be machine braided. Figure 2.2.4 shows that the elongation does not corrolate with diameter, but is sensitive to the carrier polymer.

### Braiding of green fibers

Full transposition of filaments in multifilamentary conductors will be necessary to minimize AC losses and assure an identical electromagnetic enviroment for all filaments. We intend to achieve filament transposition by braiding the green fiber. For the ribbon wire, a flat braid is desired to keep the filaments near the mechanical neutral axis. To evaluate the behavior of the green fiber during braiding several braids were prepared on a tubular braiding machine. Sucessful braiding requires both strength and flexibility from the green fiber. In early attempts, samples of 125 micron and 200 micron Y-123 green fiber were too brittle to survive the

braiding process. These particular fibers had breaking loads of 27 and 49 grams, respectively, and tensile elongations of 40.7 and 57%, respectively. Sucessful 8- and 16-filament braids were produced with 250 micron Y-123 green fiber. The sucessful fiber had a breaking load of 84 grams and a tensile elongation of 106%. Figure 2.2.5 shows the cut cross section of the green 16-filament braid and the top surface of the 8-filament braid. This particular fiber was prepared with extra lubricant, so had poor burnout properties. Consequently, these machine-made braids were not sucessfully sintered.

Very recent attempts to braid the less flexible low-lubricant HDPE fibers have had encouraging results. Through more gentle handing and special techniques, eight-filament braids have been produced from 175-micron and 125-micron green fiber. With these fibers filament breaks occurred frequently, but we believe that entirely sound braids can eventually be produced. This grade of fiber is sinterable. To illustrate that braided green fiber can be sintered, Figure 2.2.6 shows a simple hand made braids of an early grade of EVA/Y-123 green fibers which were sintered to high density without damage. The filaments entirely maintain their identity through binder burnout and sintering.

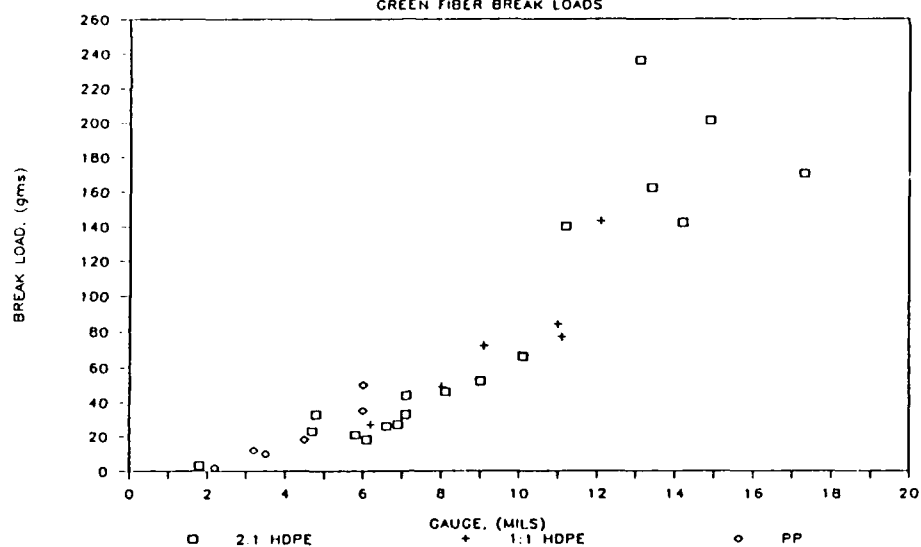## Figure 1
### GREEN FIBER BREAK LOADS



## Figure 2
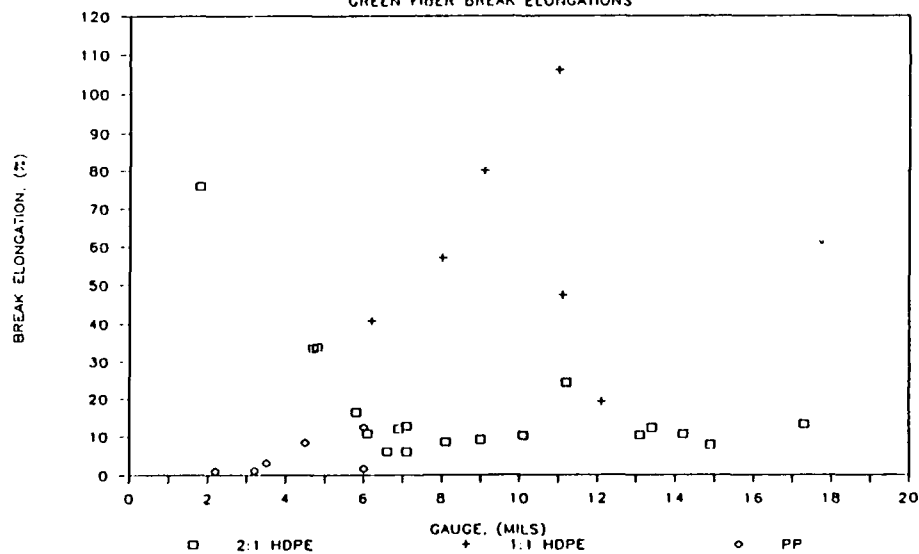### GREEN FIBER BREAK ELONGATIONS



Figure 2.2.4    Green Fiber Breaking Load and Elongation at Break versus Fiber Diameter
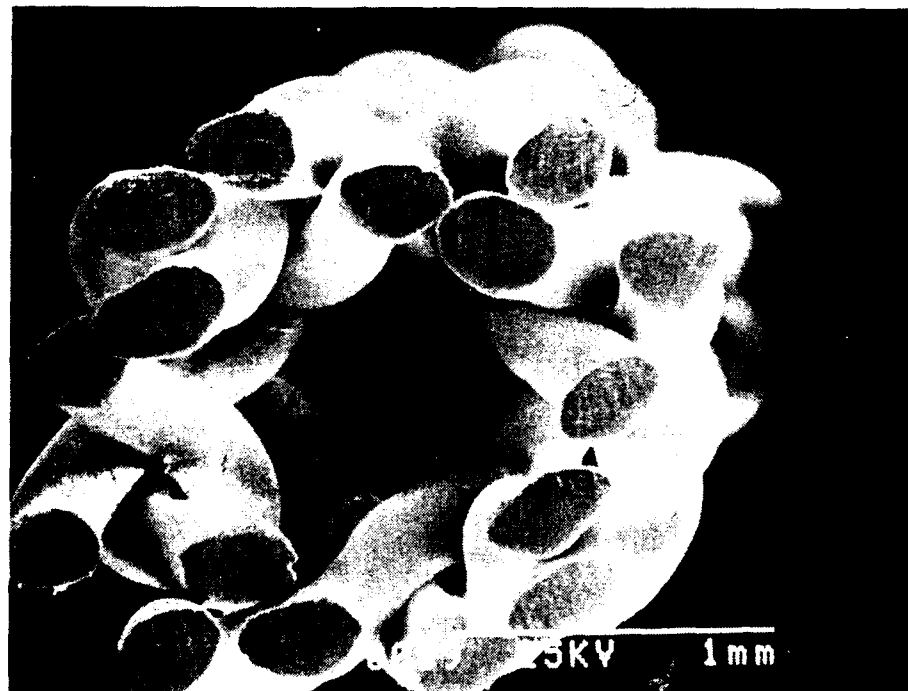
Figure 2.2.5          Cross-section of a Continuous Braid of Sixteen
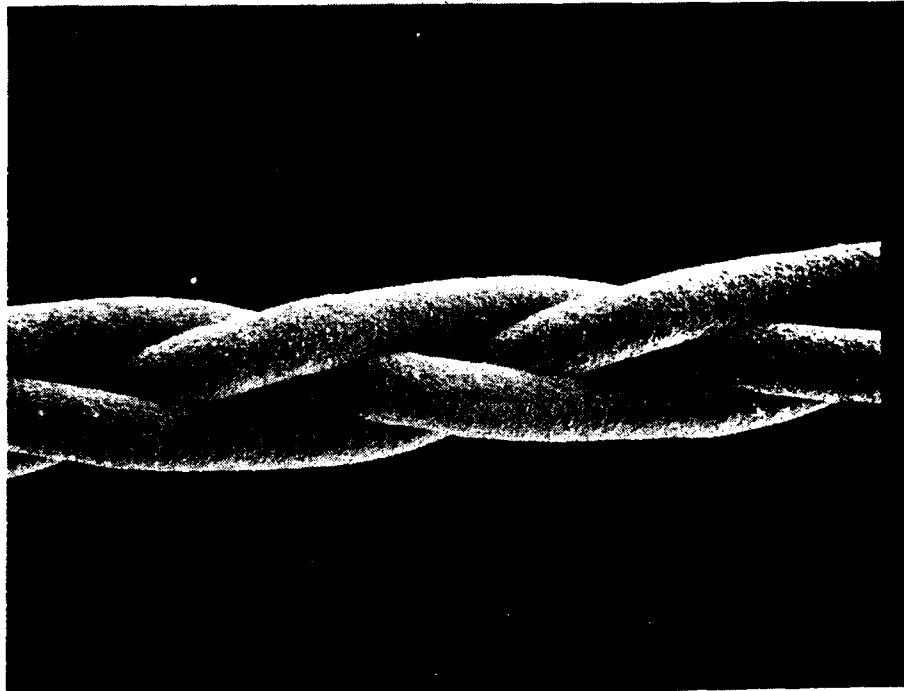                      Fully Transposed Y-123 Green Fibers

Figure 2.2.6        Three Filament Y-123 Braid after Sintering

## 2.3 Heat Treatment of Fibers

### 2.3.1 Introduction

Practical manufacture of Y-123 wire by a fiber process requires continuous sintering of fibers. If the process is ultimately to be capable of producing many kilometers of wire per day, the residence time in the sintering furnace can be no more than a few minutes. This requires very rapid sintering. Most Y-123 fiber sintering work to this point has been performed under conditions that yield high density after approximately fifteen minutes of residence time at temperature. This restriction on residence time means that the Y-123 powder must have excellent sinterability. The development of a suitable powder was a key achievement of this program.

While the goal is to sinter continuous lengths of fiber, most of the work has centered on sintering fibers about 10 cm long, since at the beginning of the program we had neither continuous green fiber nor a furnace for continuous sintering. Activities during the first two quarters involved sintering the short fibers in a laboratory tube furnace, under conditions which simulated continuous sintering, to characterize fiber sintering, Y-123 microstructure development, and to evaluate new grades of powder and fiber. These short fiber specimens were used to establish the critical current density of the Y-123 filaments. During the third and fourth quarters a commercial belt furnace was obtained and configured for continuous fiber sintering. This was used to evaluate the behavior of the green fiber for continuous sintering, and to develop a suitable fiber. By the end of the fourth quarter, meter-long fibers were being continuously sintered.

## 2.3.2     Multiple Zone Sintering of Short Y-123 Fibers

Multiple zone sintering was an expedient method to develop the fiber process before continuous sintering was possible. The emphasis changed as the program evolved. In the first quarter, the only available Y-123 fibers were dry spun using Rhône-Poulenc powder. We made use of these to explore the fiber sintering process and examined the effect of time in the hot zone, heating and cooling rates, number of passes, and peak sintering temperature on microstructure development and transport properties. Later, as experimental CPSS powders were being produced, the sintering behavior of the powders in fiber form were evaluated by zone sintering. This work led to the selection of the jet milling process for the powder. Finally, the zone sintering apparatus was used to determine the sintering range for bare and silver alloy coated melt spun fibers.

Experiments performed under the previous contract[15] and the first two quarters of this contract were aimed at simulating the manufacturing heat treatment process of continuous lengths of fiber rapidly passing through a multi-zone furnace. To achieve this, short lengths (approximately 10 cm long) of green fiber and a Lindberg laboratory furnace were employed. The fibers are placed on an alumina substrate setter that is passed through the horizontal tube furnace at a controlled speed. The alumina substrate rests upon a low thermal mass sled made of rigid alumina fiberboard attached to a slender alumina push rod. The rod is attached to a motorized positioning-track apparatus that moves the sled in and out of the hot zone at controlled rates of between 4 and 150 cm/min. The hot zone of the peak temperature is

---

[15] "Composite Ceramic Superconducting Filaments for Superconducting Cable," ONR Contract N00014-87-C-0789, Final Report 12 July 1988

4 cm wide and fairly uniform between approximately linear 7°C/cm thermal gradients.

As the fibers are passed through the furnace, they are heated to the peak temperature in 4 to 8 min, remain at peak temperature for 1 to 2 min, and then cool at the same rate they were heated. An example of a typical heating profile is shown in Figure 2.3.1. The minimum temperature between successive passes is always below 800°C. After sintering, samples are annealed in a separate furnace.

Smaller diameter green fibers can be directly passed into the hot furnace in air, with binder burnout occurring during the rapid heating (about 300°C/min). However, green fibers larger than about 200 $\mu$m diameter tend to combust if heated this rapidly in air. This can be avoided if the green fibers are preheated above the binder decomposition temperature in an oxygen-lean atmosphere. Most of the zone sintered fibers were subjected to an initial preheat for binder burnout in a nitrogen rich atmosphere, by heating to 500°C at a rate of 5-10°C/min, and then cooling for storage at room temperature until the zone sintering experiments.
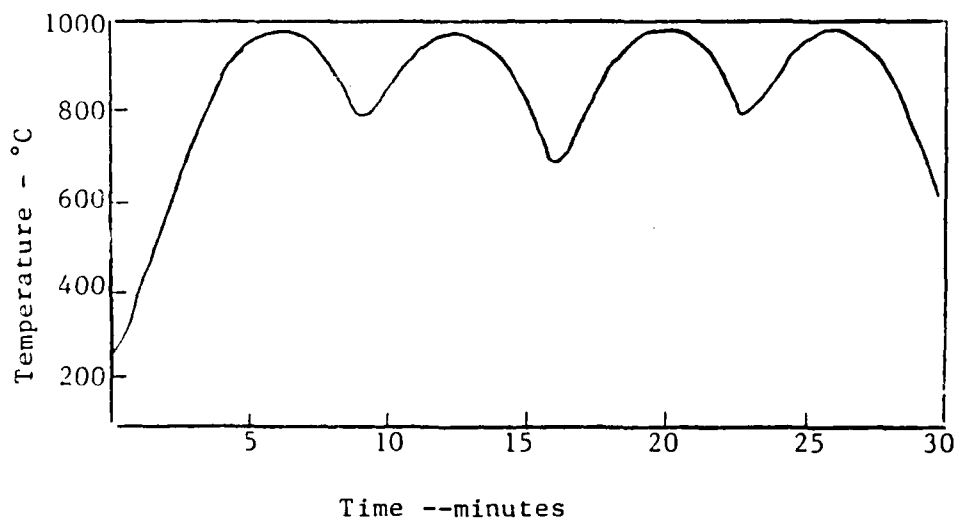
Figure 2.3.1    Typical Temperature-Time Profile for Zone Sintering.

2.3.3          Quantitative stereology of microstructure development

The microstructure development during zone sintered Y-123 has been characterized in some detail for dry spun fibers prepared with Rhône-Poulenc powder. Polished and etched surfaces of selected filaments were examined in detail to determine the grain "widths," "lengths" and aspect ratios. Width and length were determined by measuring the shortest and longest dimensions in the platy-shaped grains. The observations reported in this section essentially document the progress of the secondary recrystallization of grains much larger than the original particle size. Since these fibers were prepared from the Rhône-Poulenc powder, which had about 3 wt% excess copper oxide, the microstructure development reflects liquid phase sintering.

Seventeen filaments were selected for analysis. These were taken from three series of experiments: series A, zone sintered at 950°C for 2 to 10 passes; series B, zone sintered at 935°C for 4 to 12 passes; and series C, that received a 28 min isothermal hold. The average width, length, and aspect ratios of these filaments were measured. The area fraction of fine primary grains, which could not be individually distinguished in the etched specimens, were recorded as the less-than-1-micron fraction. What follows is a presentation of actual distribution data as well as correlations using the combined data set.

Figure 2.3.2 displays the combined data for all filaments, showing the average aspect ratio versus the average grain width. It appears that the aspect ratio scatters around 4-5, independent of the grain width, indicating that the shape of the grains do not change as the microstructures develop.

The Y-123 appears to display a well-defined habit in the presence of a CuO-rich liquid phase.

Grain growth at 950°C is illustrated by Figure 2.3.3, as a sequence of histograms displaying the grain length distributions after 2, 4, 6, 8, and 10 repeated passes through the hot zone. Each pass corresponds to 3.5 min at temperature. The sample is relatively porous after two and four passes, but dense after six passes. Notice the less-than-1 $\mu$m category, which corresponds to the finer primary grains. After two passes, the fine primary grain matrix occupies the entire structure. Upon further repeated passes, the fraction of primary matrix gradually diminishes, vanishing after ten passes. The population of larger secondary grains increases in proportion, with the mode gradually moving to larger grain sizes.

A similar development occurs at 935°C, shown in Figure 2.3.4. The sub-micron categories are truncated from these histograms, so only the population distributions of secondary grains are displayed. The maximum grain length, and number of larger grains increases with repeated passes. The progression of average grain sizes with time upon repeated passes is displayed in Figure 2.3.5A showing average grain width as a function of number of passes and time at temperature, and Figure 2.3.5B that shows the behavior of the average grain length. The size of the error bars show the standard deviation.

Figure 2.3.6 compares the grain size distributions in filaments sintered isothermally for thirty minutes at 935, 945, and 965°C. The most frequently occurring grain lengths are 4-6 $\mu$m for all three temperatures, but the population of grains larger than 16 $\mu$m is greater at higher temperature. One can compare the grain size distributions for zone sintered and isothermally sintered specimens using the 935°C histogram of Figure 2.3.6 and

the eight pass histogram of Figure 2.3.4. In this case, the isothermal and zone sintered specimens are roughly similar.

These early filaments from Rhône-Poulenc powder had low critical current densities ranging between 125 and 792 $A/cm^2$, but it is interesting to inquire if they can be corrolated with microstructure. The entire database of 17 specimens can be used to construct a graph of critical current density versus grain size. Figure 2.3.7 displays such a graph for average grain length of each specimen plotted with its $J_c$. The results are highly scattered, but on first glance seem to show a trend of lower $J_c$ for larger grains. Note, however, that the largest grain size/lowest $J_c$ combinations are for the isothermally sintered specimens. If these three points are excluded, the trend becomes much weaker. Considering the variability in $J_c$ and the width of the grain size distributions, no conclusions can be drawn on the influence of microstructure on weak-link critical current densities.

Finally, these data can be used to relate critical current density to zone sintering conditions. Figure 2.3.8 displays the data for the 935°C series, showing $J_c$ as a function of number of zone passes. There is no trend in these data that is visible against the scatter.

## 01147 and 01153 Series Samples
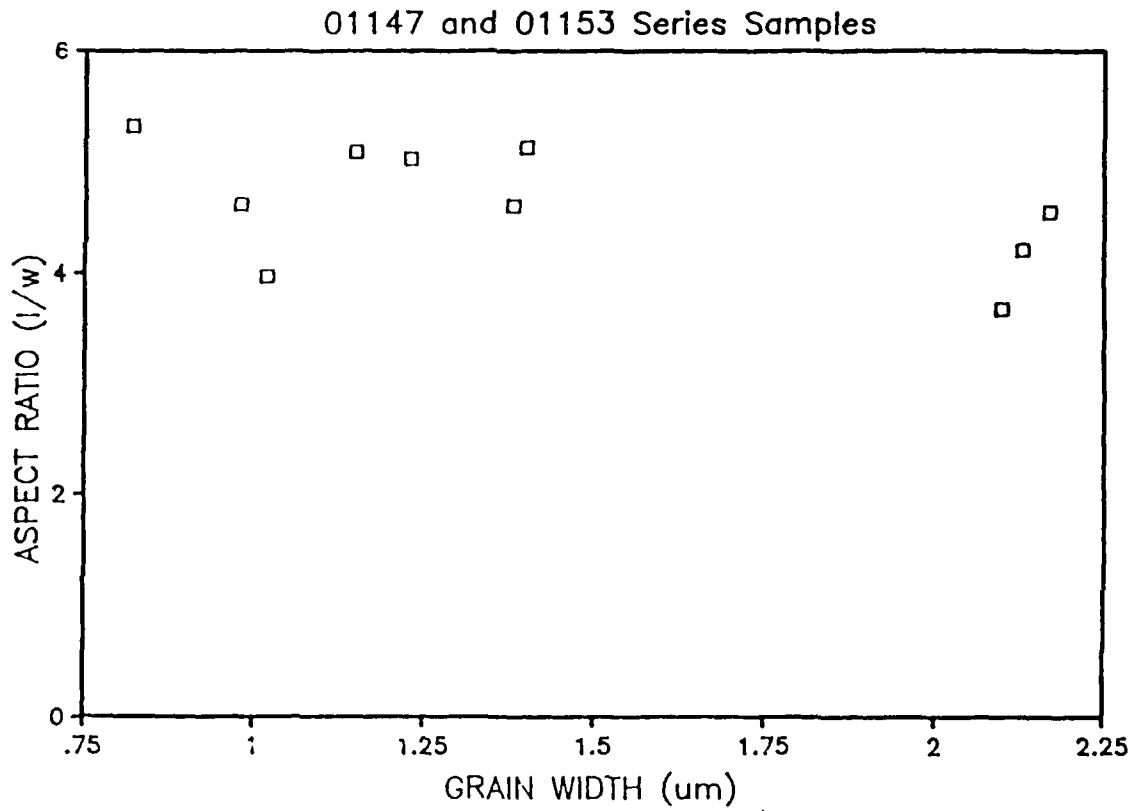


Figure 2.3.2        Average Aspect Ratio versus Average Grain Width for $YBa_2Cu_3O_{7-\delta}$ Filaments Sintered at 935 and 950°C.
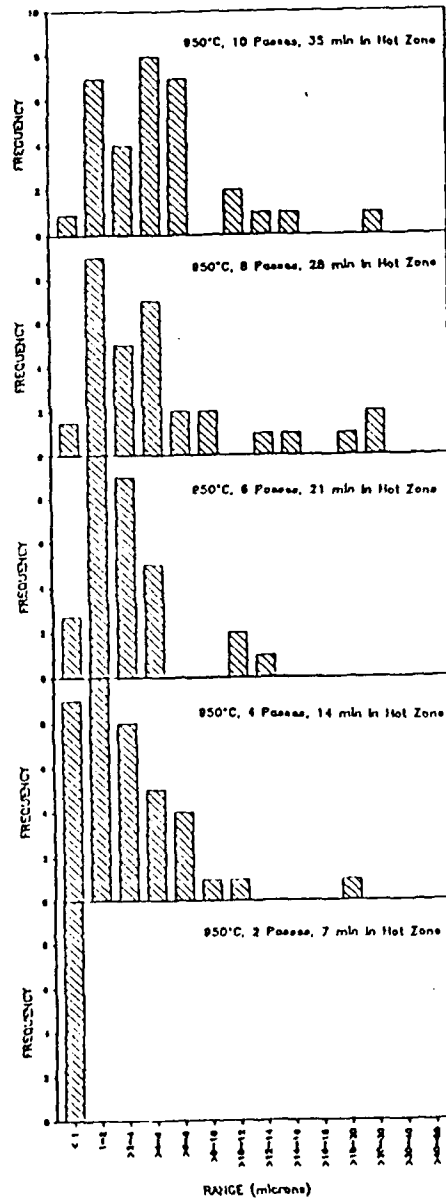
Figure 2.3.3       Grain Length Distributions For $YBa_2Cu_3O_{7-\delta}$ Filaments Zone Sintered at 950°C for 2, 4, 6, 8, and 10 Passes. Each Pass Corresponds to 3.5 Minutes at Temperature.
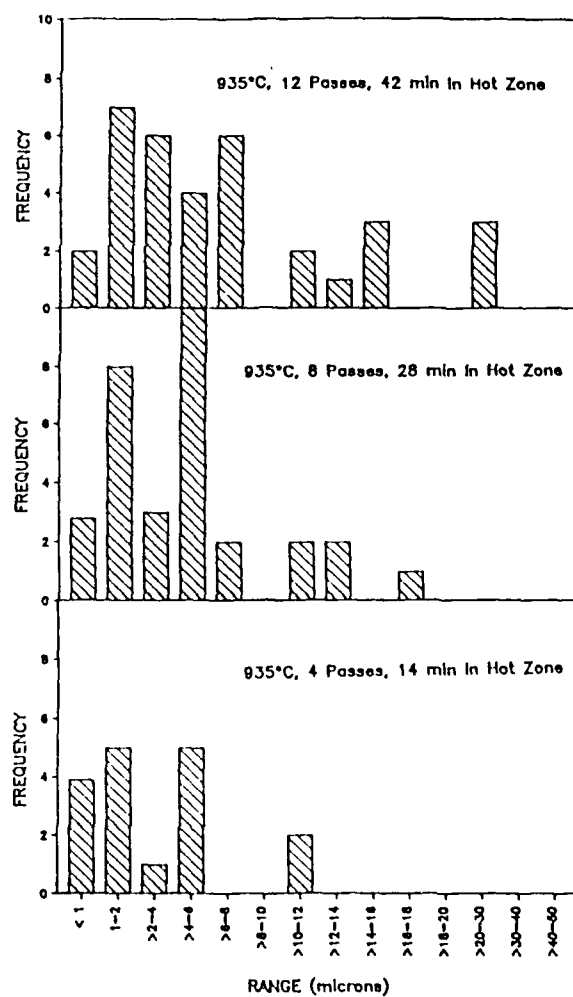
Figure 2.3.4    Grain Length Distributions for $YBa_2Cu_3O_{7-\delta}$ Filaments Zone Sintered at 935°C for 4, 8, and 12 Passes.    Each Pass Corresponds to 3.5 Minutes at Temperature.
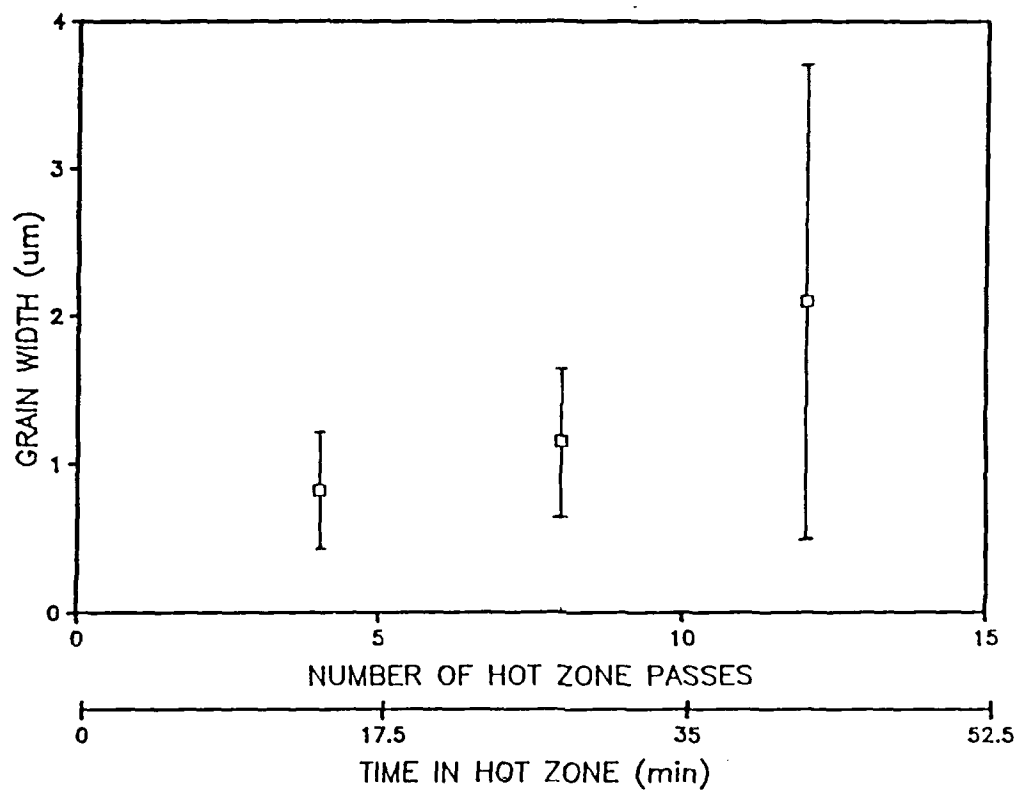
Figure 2.3.5A      Average Grain Width versus Number of Zone Passes and Time at Temperature for $YBa_2Cu_3O_{7-\delta}$ Filaments Sintered at 935°C.
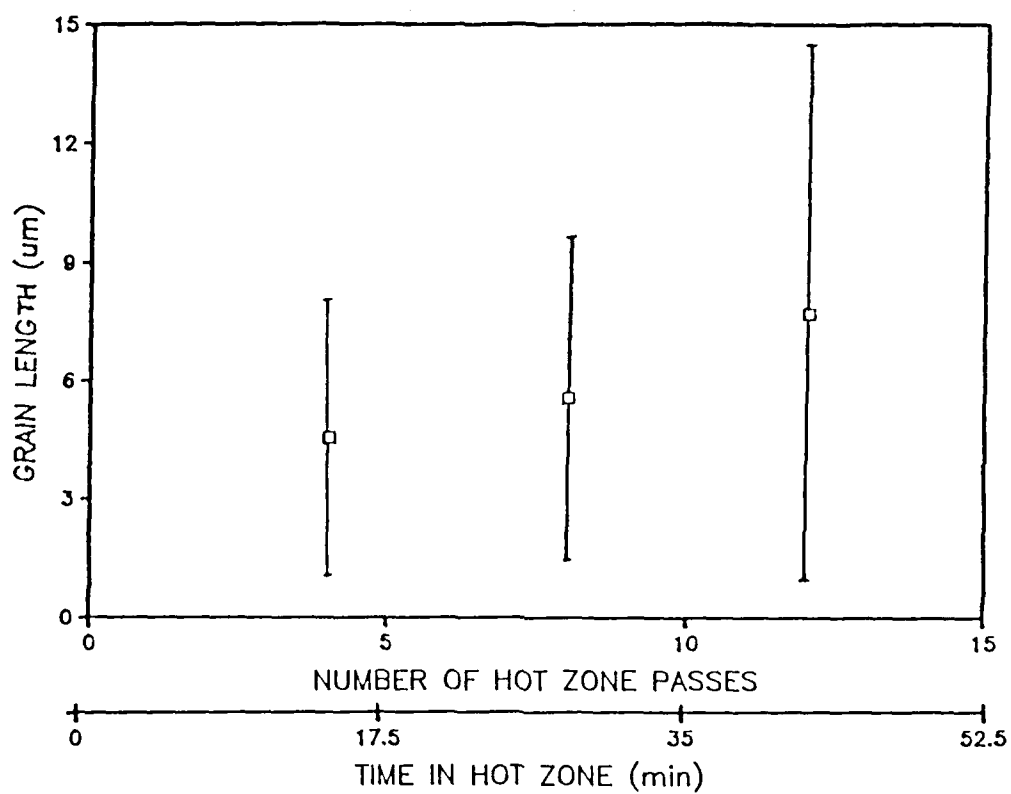
Figure 2.3.5B      Average Grain Length versus Number of Passes for $YBa_2Cu_3O_{7-\delta}$ Filaments Sintered at 935°C.
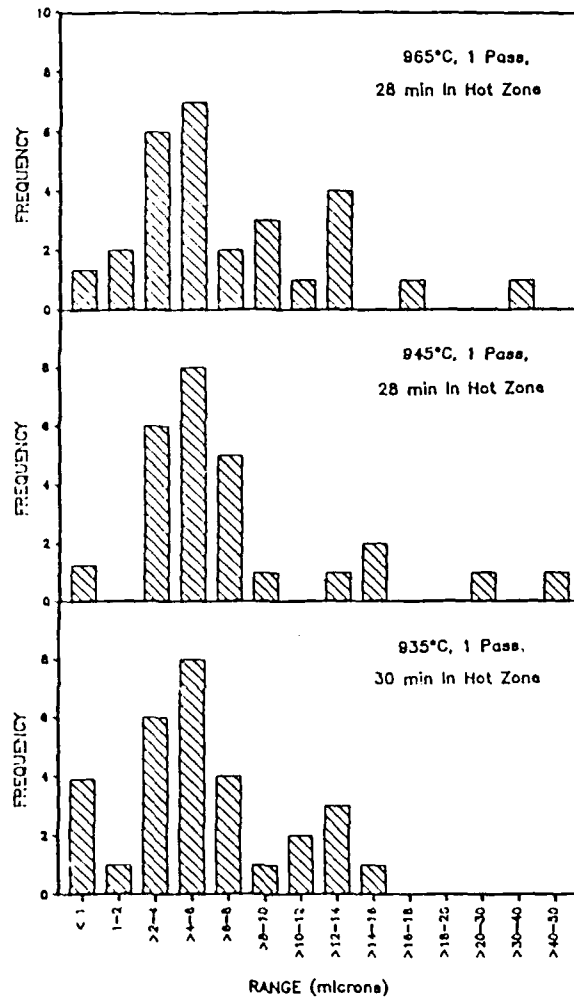
Figure 2.3.6     Grain Size Distributions in Isothermally Sintered $YBa_2Cu_3O_{7-\delta}$   Filaments.
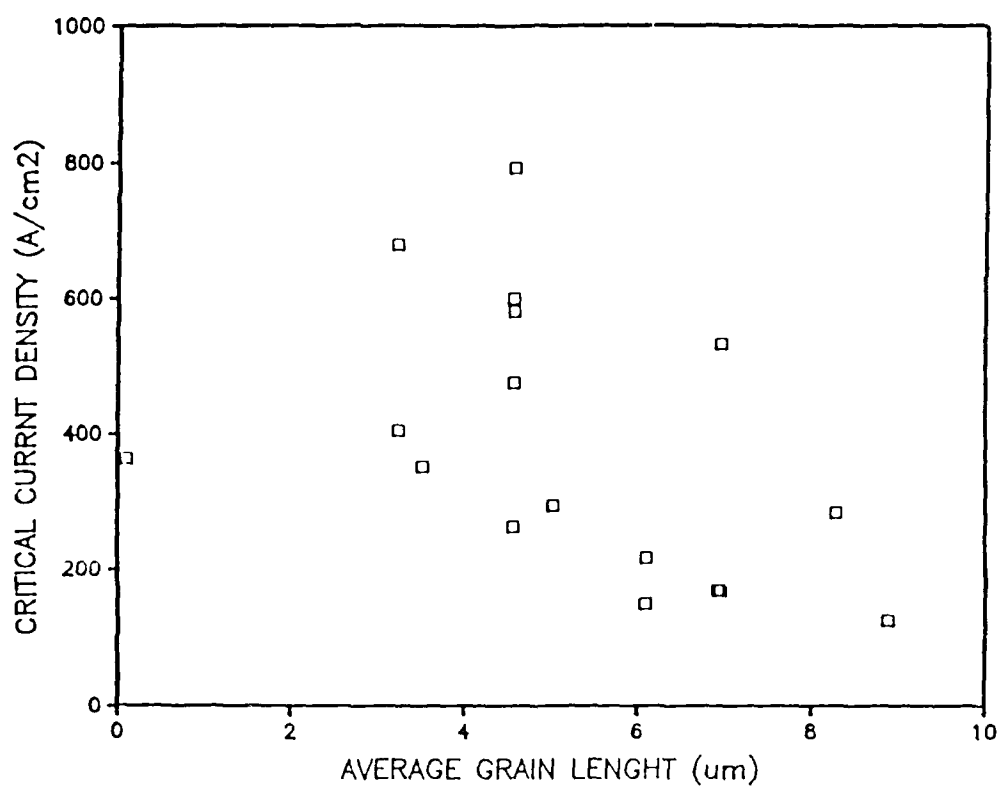
Figure 2.3.7      Critical Current Density versus Average Grain Length for $YBa_2Cu_3O_{7-\delta}$ Filaments Sintered Under a Variety of Conditions.

"01" SERIES
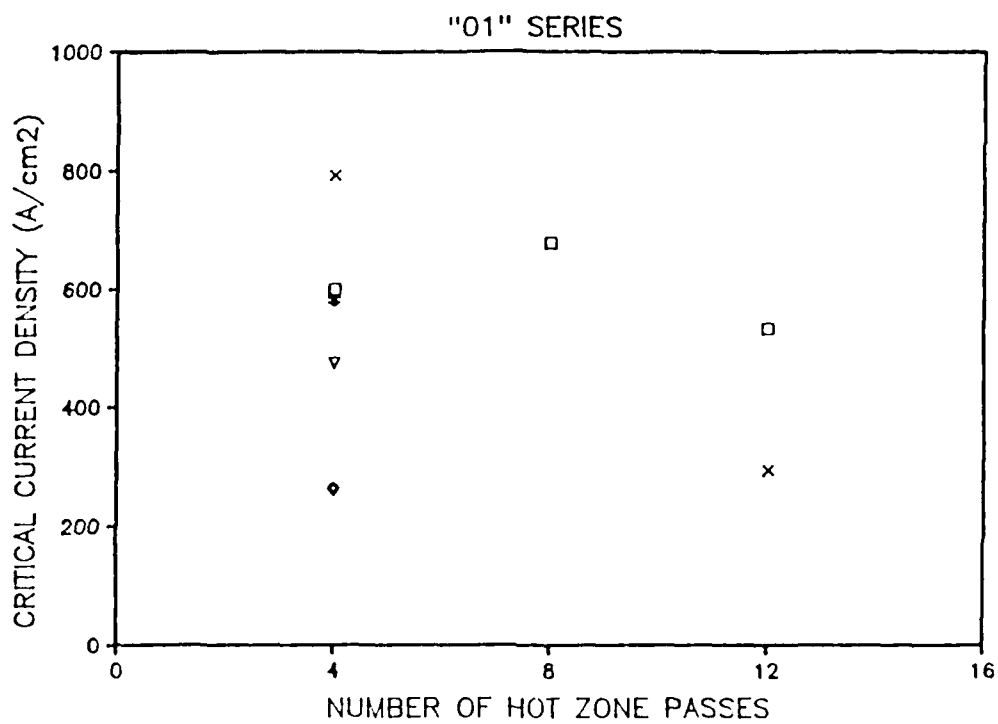
Figure 2.3.8    Critical Current Density versus Number of Repeated
Passes for $YBa_2Cu_3O_{7-\delta}$ Filaments Zone Sintered at 935°C.

2.3.4      Continuous laboratory scale sintering

The furnace for continuous fiber sintering is an infrared belt furnace manufactured by the Radiant Technology Corporation (RTC)[16]. This, intended for firing thick film circuits, consists of a 2 meter heating and cooling section fed by a 2.5 meter long metal mesh belt. The heating section has three zones of control, each about 30 cm long, which use quartz lamps as the heat source. As the name implies, radiation is the primary mode of heat transfer. This furnace is capable of very rapid heating and cooling and can maintain precise temperatures and atmospheres in its heating section. The RTC belt furnace was obtained as a laboratory scale continuous furnace to serve as the prototype for the pilot scale furnace.

The RTC furnace is undergoing continual modifications to reconfigure it for fiber sintering. To support the Y-123 fibers, the metal mesh belt has been covered with suitable woven ceramic fabrics sewn onto the belt. Preliminary work has been with a plain weave tape of Nextel 440[17] aluminosilicate fiber. This appears to be compatible with Y-123 under the RTC sintering conditions of relatively brief 10-30 minute exposures to peak temperature. Occasionally, there is slight sticking of the fiber to the Nextel, which may prove a problem in the future. Also, the durability of the Nextel tape is only marginal. We continue to search for alternatives.

---

[16]. Model RTC A-306X, Radient Technology Corporation, Cerritos, CA 90701

[17]. Nextel 440 fiber, composition 70wt% alumina-28 wt% silica-2 wt% boria, from 3M, St. Paul, MN 55114

As expected, early attempts to achieve continuous fiber sintering uncovered problems which were not important for sintering short fibers. As discussed in Section 2.2, post-drawn green fiber tends to shrink and distort when heated past the polymer melting point. This is a nuisance for short fiber sintering, but intolerable for continuous sintering because it breaks the fiber. It was necessary to prepare green fiber with no spin draw or post draw. Shortly after 125-micron as-spun green fibers were made at AIResCo, a 1-meter long bare fiber was successfully sintered in the RTC.

Sintering one-meter lengths of fiber in the RTC demonstrates the feasibility of continuous sintering of these fibers, since they are significantly longer than the RTC furnace hot zone. Presently we are limited to these lengths because we are unable to do both binder burnout and sintering in a single pass through the RTC. Instead we send the fiber through the furnace three or more times. This "semi-continuous" sintering will continue until the profiles for binder removal and sintering are defined well enough to add more heating sections to the furnace during the next quarter. Until then we are limited to producing 1-2 meter lengths of wire by semi-continuous sintering. These, however, are adequate for testing the electrical and mechanical properties.

A typical schedule involves three passes. The first pass accomplishes the early stages of binder removal, exiting the RTC at up to 310°C. The second pass at 330-900°C completes binder removal and presinters the filament. The third pass completes sintering at 960° for Ag/Pd co-firing or 980°C for bare Y-123 fiber. At the exit end of the furnace belt, the partially sintered fiber is transferred to a 2-meter long aluminum channel. The fiber is taken to the entrance end and pulled off the channel by the

furnace belt. Since the fragile fiber must push or pull itself along the length of the channel, this step frequently breaks the fiber. This is presently a practical length-limiting problem. A second belt assembly is being constructed to remedy this problem.

A more serious problem currently limiting wire length is related to binder removal. Under conditions where most of the fiber has satisfactory burnout, there are occasionally local problem regions where the fiber breaks due to a binder burnout problem. These include bloating, curling, and similar local defects. We have not yet determined if these are caused by the furnace or if they are due to defects in the green fiber. We expect to be faced with a series of length-limiting problems as the continuous sintering process is developed.

It is encouraging that the fiber is robust enough to survive this handling. It is also encouraging that the actual densification of the Y-123 fiber at the peak temperature is apparently no problem. It seems that the hot fiber either accommidates the axial shrinkage associated with densification, or else shrinks primarily in the radial dimension.

Preliminary data on the critical current of the semi-continuously sintered Y-123 filaments show that the transport critical current is similar to zone sintered filaments. A sample taken from a 60-cm long semi-continuously sintered Ag/Pd co-fired filament had a self-field critical current of $1413A/cm^2$.

## 2.4 Filament Cladding and Wire Fabrication

### 2.4.1 Introduction

Cladding developments have been directed in three areas: 1) producing silver alloy co-fired filaments; 2) developing the ribbon wire solder cladding process; and 3) evaluating several metal deposition methods. The first two activities are directly related to the in-house wire process development. The metal deposition work is carried out with collaborators to allow us to explore the fundamentals of metallization of Y-123 while evaluating a possible alternative cladding process.

2.4.2      Silver Coated Filaments

Both the ribbon wire and the monofil wire are based on co-firing Y-123 fibers with silver alloy coatings. They differ only in the desired alloy coating thickness, which reflects the differing functions. For the monofil wire, the silver alloy is the entire cladding, so the coating thickness must be appropriate for the desired metal/superconductor ratio. For a ratio of one, which is assumed for the mechanical properties, the target thickness is about 20 microns for a 100 micron fiber. Coatings this thick will require a rather long oxygen anneal, which will be conducted on spools of as-fired wire. The primary functions of the silver alloy coating for the ribbon wire is to render the filament surface wettable by solder, and to act as a barrier preventing direct contact between the Y-123 and the solder. The silver alloy coating can be as thin as a few microns, which may be compatible with continuous in-line annealing. However, in the near term, the braided filaments for the ribbon will be batch annealed, so a thicker coating will be applied to strengthen the filaments for spooling.

The coating process has been developed to the point where about one hundred meters of the 125 micron green fiber can be continuously coated.

The coating process requires de-spooling the fiber and drawing it past a series of guides in the coating unit. Friction and abrasion during handling tended to break the fiber, so it was necessary to build a coating unit with motorized rollers and a de-spooler. More development of the coating materials and process is necessary to improve control of the thickness and uniformity of the coating, particularly for the monofil wire.

The initial co-firing involved silver coatings, which is satisfactory for sintering temperatures below 930°C. Figure 2.4.1 shows the polished cross section of a silver coated Y-123 fiber (made from CuO-excess Rhône-Poulenc powder) co-fired by zone sintering at 925°C. Above this temperature, it was found that the silver remains solid for a brief time, but eventually melts. For example, for zone sintering at a peak temperature of 955°C (below the 961°C melting point of pure silver), the coating was solid after the first two passes, but melted after the fourth pass. This is probably the result of slow dissolution of oxygen into the silver, which results in the formation of the $Ag\text{-}Ag_2O$ eutectic at 931°C.

This is too low to densify the phase pure Y-123 fibers in a conveniently short time, so higher melting silver-palladium alloy coatings were developed. The composition of the silver palladium alloys are chosen by their liquidus temperature which, for constant particle size, largely determines the sintering temperature. The primary concern is avoiding melting during cofiring. The apparent temperature[18] at which melting becomes a problem is significantly lower than the liquidus. The Ag-15Pd alloy, with a

---

[18] The actual temperature experienced by the fibers during zone sintering is not crisply defined. The fibers are always being heated or cooled, so the temperatures experienced may depend upon the emmisivity. "Peak temperature" is defined by the reading of a fine thermocouple traveling with the specimens.

1065°C solidus, is useful up to 1000°C and the Ag-18Pd composition, 1090°C

solidus, is useful up to 1030°C. We find that silver powders with finer

particle size melt at lower temperatures, presumably because of more rapid

formation of the Ag-O eutectic.

Silver palladium alloys appear to be non-reactive with Y-123 up to

a temperature around 970°C. On samples annealed at 960°C, the interface

between Y-123 and Ag-15Pd appears sharp, with no visible evidence of reaction.

X-ray diffraction of a 50% Y-123/50% Ag-15Pd pellet, annealed at 960°C, showed

only the Y-123 phase and silver alloy. Above about 970°C, however, some

reaction occurs to degrades the Y-123.

Fortunately, it is possible to achieve satisfactory densification

of the Ag-Pd coated fibers in the RTC below 970°C. Figure 2.4.2 is a fracture

surface of a semi-continuously co-fired Ag-Pd coated filament after sintering

in the RTC at 960°C. The density is satisfactory. This particular filament

had a self-field critical current above 1400 A/cm$^2$.

The physical properties of the silver alloy clad filaments are

quite different from bare Y-123 sintered fibers. With thick silver coatings,

they look and behave much like silver wire. They are much stronger than bare

filaments and much easier to handle. We have not yet measured their

mechanical properties. This work is planned for later this year when

continuous wire is available. The clad filament bends as if it were ductile,

although the substrate Y-123 core inside is certainly damaged by bending. They

can be directly electroded with solder.

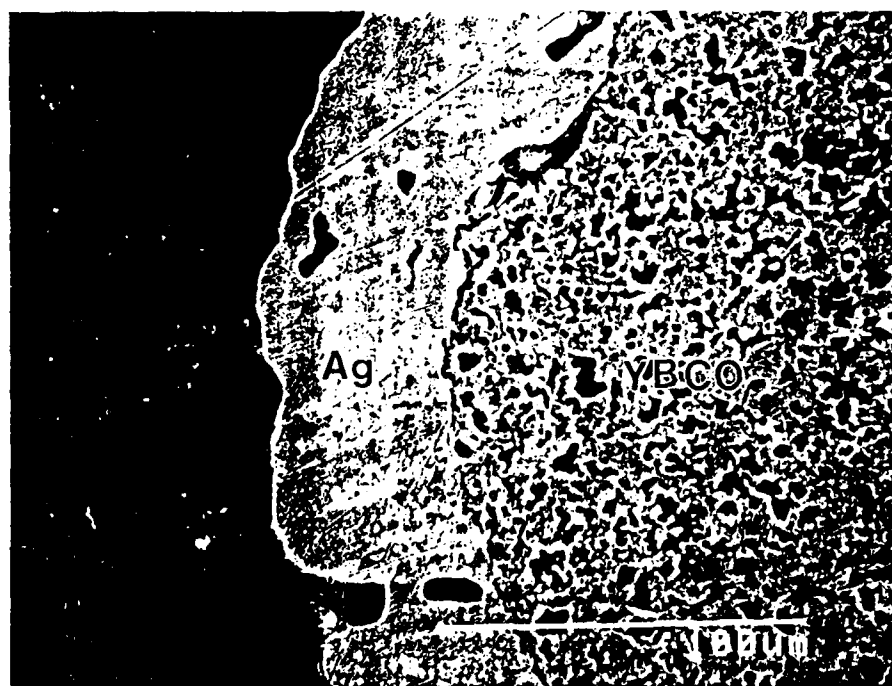Figure 2.4.1        Polished Section of Silver Coated Y-123 Green
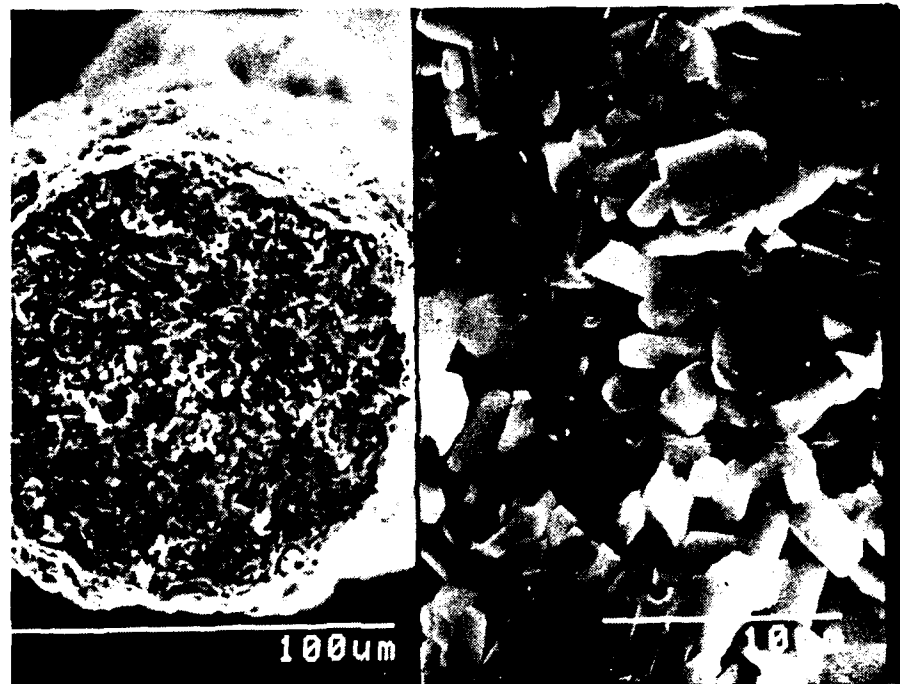                    Fiber Co-Fired by Zone Sintering at 925°C

66



Figure 2.4.2        Fracture Surface of Semi-Continuously Co-Fired
                    Ag-Pd Coated Y-123 Filament

## 2.4.4    Development of the Ribbon Wire

Our present approach is to manufacture of the flexible ribbon conductor using a simple solder reflow step. The anticipated product of this process is shown in Figure 2.4.3. The key is to treat the surface of the $YBa_2Cu_3O_{7-\delta}$ fiber with the silver alloy coating so it can be wet by solder and bonded to a copper strip. It is preferable to have a very thin or even porous silver coating, sufficient to render the filament able to be wet by solder, but not so thick as to present a diffusion barrier during the oxygen intercalation anneal.

The reflow bonding process involves sandwiching an array of sintered silver-coated filaments (preferably as a flat braid) between two solder clad copper strips, and heating the assembly so the solder flows around the filaments, bonding the filaments and joining the copper strips. This cladding process has a number of advantages: it is a simple process, it can be carried out continuously, it is not likely to degrade any superconducting properties, and it can be scaled up to commercial production. Solder clad copper strips are commercially available from several vendors. The ribbon conductor can be produced in any desirable width and thickness in continuous lengths. Also, by a judicious choice of solder which melts at high temperature, a compressive state of stress can be induced around the filaments.

For cryogenic applications it is important to choose a solder based on a face centered cubic lead-tin alloy, since the body center tetragonal alloys undergo a ductile-to-brittle transition. This implies a Pb-Sn composition with at least 80% lead. After some experimentation, we have

chosen a solder composition of 97.5% Pb, 1% Sn, and 1.5% Ag, which has a eutectic temperature of 309°C. Because it contains silver, this solder bonds well to silver without leaching it from the substrate.

The copper strips for the ribbon wire are 5 mm wide, 100 micron thick strips of oxygen free C10200 soft anneal copper overlaid with 50 microns of the 97.5% Pb- 1% Sn- 1.5% Ag solder, produced by Handy and Harman, East Providence, RI.

Small coupons of the ribbon wire were fabricated by hand by arranging a small number of sintered Y-123 filaments between copper strips and conducting the reflow in box furnaces. Figure 2.4.4 shows the cross section of a prototype ribbon composite made with a copper channel which could be sealed after placing the solder strips and the filaments inside it. The wetting of the silver clad filament by the solder is very good; no large voids can be seen in the solder. These were heated in $N_2$ or a $N_2$-5% $H_2$ atmosphere to avoid oxidation of the solder or copper. Attempts to reflow in air failed because as both solder and the copper oxidized. In these early trials, the reflow treatment involved rather long heating in box furnaces. Oxidation is not expected to be a problem in the cladding module, since we will use a protective atmosphere and much more rapid heating and cooling.

## 2.4.3 Development of the Cladding Module

The cladding module is a stand-alone unit which accepts two spools of the solder overlaid copper foil strips. The foil strips are pulled into an alignment unit which places them over and under the sintered fibers, pulls the assembly into a reflow unit, past a cooling zone, and onto a 61 cm diameter spooler. The speed control of the cladding module can be synchronized with the

sintering furnace. The reflow unit consists of stainless steel blocks heated to 350°C with 200 watt cartridge heaters. This unit has been tested successfully in preliminary trials. The solder overlaid copper strips can be continuously reflow bonded when pulled through the heated blocks at 5-8 cm/minute. A design feature of the reflow unit is an arrangement to contain the molten solder between the copper strips, allowing a symmetrical ribbon wire to be directly produced.

At the end of the fourth quarter, all major components of the module had been fabricated, and the module was assembled. Tests of its ability to bond the copper strips to short lengths of sintered filaments will be conducted during the coming quarter.
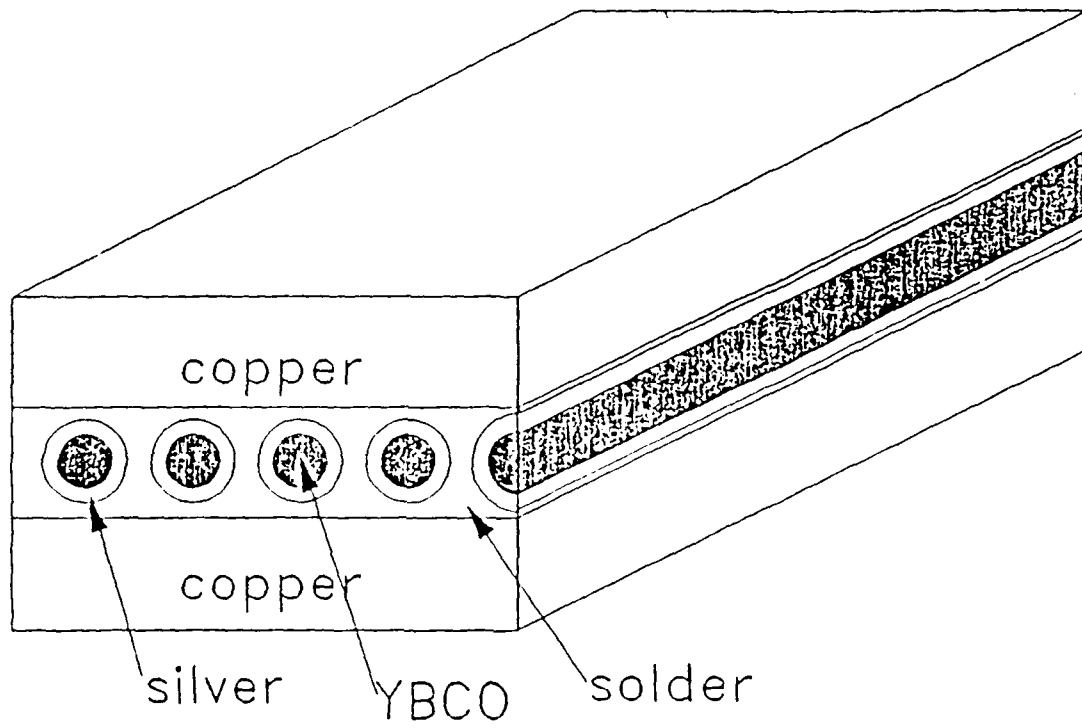
Figure 2.4.3    Ribbon Conductor Fabricated by Solder Reflow Bonding to Copper Strips.
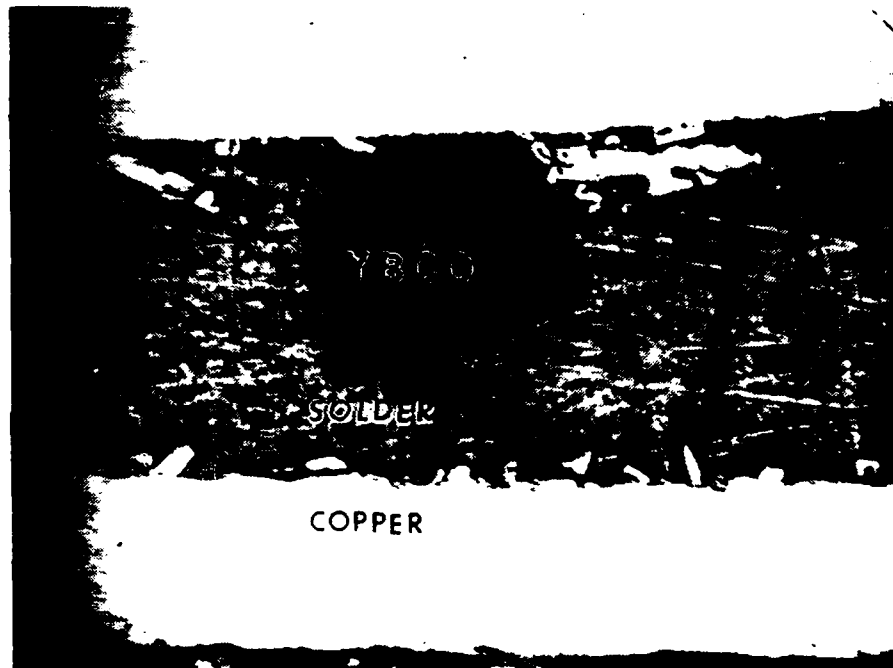
Figure 2.4.4        Prototype Coupon of Ribbon Composite

2.4.4        Other Cladding Methods

In addition to the silver alloy co-fire and solder reflow cladding methods being investigated in-house at CPSS, several other methods have been explored in collaborative programs. These include chemical vapor deposition investigations at Advanced Technology Materials, non-aqueous electrodeposition at National Institute for Standards and Technology, and aqueous electrochemical methods at SUNY-Buffalo.

2.4.4.1        Aluminum cladding by chemical vapor deposition

Dr. Ward Stevens of Advanced Technology Materials, New Milford, CT, undertook an exploratory project to produce aluminum claddings on sintered $YBa_2Cu_3O_{7-x}$ filaments using metallorganic chemical vapor deposition (MOCVD). The superconducting filaments were sintered from dry spun fibers made from Rhône-Poulenc powders provided by CPSS. The electrical characterization was performed at CPSS. The primary objective was to obtain aluminum coatings about 1 mil thick in several minutes residence time, without degrading the superconducting properties of the $YBa_2Cu_3O_{7-x}$. Deposition temperatures were to be kept as low as practical.

Two aluminum MOCVD reagents were utilized for deposition, triiso-butylaluminum and triethylaluminum, with the bulk of the work employing the former. Several modifications of the MOCVD process were examined including hot-wall and cold-wall deposition, as well as novel methods proprietary to Advanced Technology Materials. With limited experimentation in each method, cold-wall reactors yielded the best coating, a smooth, dense conformal coating. Other techniques produced coatings that had nodular or sooty

morphologies. Observations of cold wall reactor deposits suggest that one micron thick coatings can be grown within minutes.

Run times for the hot-wall depositions were two hours in both of the above examples. In the reduced concentration run a glass fiber was included along with the superconducting filaments. As seen in Figure 2.4.5, the growth morphology is much more coarse, perhaps an indication of fewer nucleation sites during the initial stages of growth. The deposit thickness on the glass filament is approximately 40 microns while the deposit on the superconductors averaged 20 microns. The differences in thickness may be due to differences in the growth modes and their relative densities.

By heating just the substrate, as in a cold-wall reactor, gas phase nucleation can also be controlled. Reagent enters the deposition chamber and composes directly on the substrate. In this fashion, very smooth coatings of aluminum were deposited on the superconducting filaments, as shown in Figure 2.4.6. However, the thickness of these deposits was limited to about 1 micron. Observation of the growing surface suggested that these films grew within about 20 minutes, after which no additional growth appeared to occur. These results require verification by parametric experiment. If this were the case, nucleation aids might be employed to sustain reasonable growth rates.

Conformal, dense aluminum deposits could be applied to superconducting filaments by MOCVD using triisobutylaluminum via hot-wall and cold-wall deposition schemes. Thin, one micron, hermetic coatings could be applied within minutes and may be useful as a starting point for alternate metal deposition processes, C' ) or others.

Only the filament processed in the cold-wall reactor exhibited Meissner effect. An attempt was made to measure the transition temperature of this filament. However, the measuring current passed through the metal only and no transition was observed. This could be due to an insulating layer of at the filament-aluminum interface. More details are given in the section on electromagnetic characteristics.
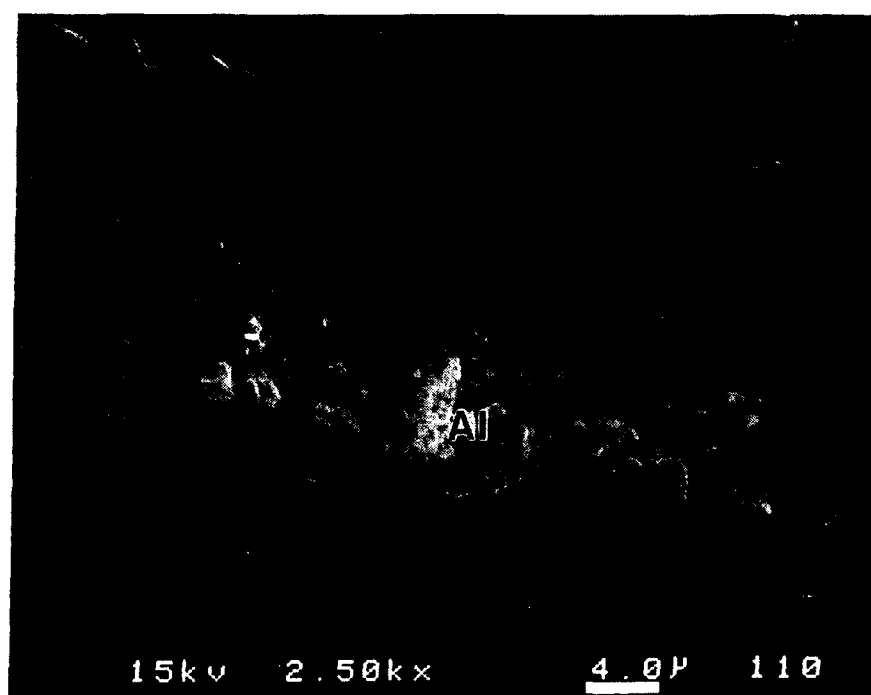
Figure 2.4.5    Morphology of MOCVD Aluminum Deposit on
                $YBa_2Cu_3O_{7-x}$ Filament Produced at ATM in a Hot Wall
                Reactor
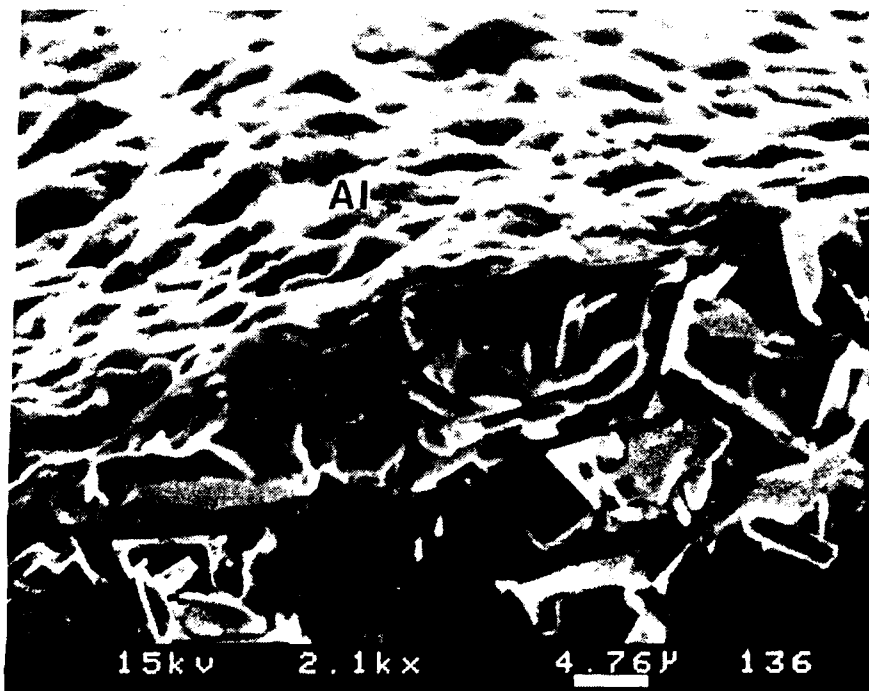
Figure 2.4.6          MOCVD Aluminum Deposit on $YBa_2Cu_3O_{7-x}$ Filament
                      Produced at ATM in a Cold Wall Reactor

2.4.4.2    The electrodeposition of an aluminum-manganese metallic glass from molten salts

This work was performed by Dr. Gery Stafford of the Institute for Materials Science and Engineering at the National Institute of Standards and Technology, as part of a collaboration with Dr. David Lashmore. The superconducting filaments were sintered dry spun fibers made from Rhône-Poulenc powder at CPS Superconductor Corporation. This section of the report is prepared from the report written by Dr. Stafford. An aluminum alloy was deposited onto superconducting filaments from a $MnCl_2$ doped $2AlCl_3$:NaCl electrolyte.

All melts were at the eutectic composition, 2:1 mole ratio $AlCl_3$:NaCl. The powders were thoroughly mixed in a dry box before being transferred to the cell. The temperature of the mixture was increased to 150°C and the resultant melt was pre-electrolyzed for 48 hours using a platinum screen working electrode held at a potential of +0.01 volt with respect to the aluminum wire in the same electrolyte. The desired amount of $MnCl_2$ was then added. The melt temperature for all experiments was 175°C. Potential control was maintained with a PAR Model 363 Potentiostat/Galvanostat and a PAR Model 175 Universal Programmer. The counter and reference electrodes were 2 mm aluminum wire.

The $YBa_2Cu_3O_{7-x}$ filament was lowered into the molte.. salt electrolyte while at a potential of +0.1 volt with respect to an Al wire. This cathodically protects the filament until it reaches thermal equilibrium. At this potential, a cathodic current of 20-40 $\mu A$ was generally observed. This current level is very low and indicates that the system is relatively

stable. A rest potential of +1.856 v vs. Al was observed, indicating that the $YBa_2Cu_3O_{7-x}$ is quite resistant to anodic reactions in this electrolyte.

Deposits were obtained using DC as well as pulsed deposition. The best deposits were obtained using a pulsed deposition (10 msec - 3 v/Al; 110 msec - 1 v/Al) and with 1.9 wt% $MnCl_2$. Figure 2.4.7 shows the structure of the deposit. Estimated thickness of this deposit is 4.7 $\mu$m and the estimated composition is 31 wt% Mn (from standardless semi-quantitative analysis in EDS) and rest aluminum. Based on the estimated deposit concentration, it should be entirely amorphous.

The aluminum plated filaments gave indications of a strong Meissner fraction. Unfortunately, these wires had no resistive transition. Apparently the aluminum coating is separated from the superconducting core by a resistive barrier. This suggests that aluminum alloys are too reactive to directly deposit on $YBa_2Cu_3O_{7-x}$. Transport and magnetic characterization are presented in Section 2.5.

Figure 2.4.7    Electrodeposited Aluminum-Manganese Alloy on a
$YBa_2Cu_3O_{7-x}$ Filament Produced at NIST

## 2.5        Electric and Magnetic Characteristics

### 2.5.1        Measurement Techniques

The instrumentation and measurement technique for determining the resistivity versus temperature is described in detail in previous quarterly reports. Briefly, the resistivity measurement involves scanning temperature between 140 and 77°K in a liquid nitrogen cryostat controlled by a Lake Shore 805 temperature controller. Temperature is measured with a silicon diode thermometer. Sample excitation is with 1.12 Hz 10 mA square waves with 440ms plateaus, supplied from a Kiethley 228 voltage/current source. Voltage is monitored with a Kiethley 196 digital multimeter. The algorithm for data acquisition includes averaging over several positive and negative voltages to eliminate thermal voltages. For typical filaments, "zero" resistivity is lower than $10^{-7}$ $\Omega$-cm.

A great deal of effort was expended developing reliable techniques for mounting the fine filaments and applying electrodes. For metal clad filaments, contact is simply made to the metal cladding with silver paint, to provide a low resistance contact. Electroding bare Y-123 filaments is more difficult. Two techniques are now preferred: "fired-on" silver contacts and silver paint contacts applied to sputtered silver pads.

Fired-on contacts are made by applying silver paint electrodes to the as-sintered tetragonal Y-123 filaments. These are fired at 850-925°C in the tube furnace or the RTC furnace. The filaments are later given a conventional oxygen anneal. Typically, four fired-on contacts are prepared for four-point measurements. Occasionally up to six contacts are applied for multiple contact experiments. Certain filaments are entirely coated with

either silver or Ag/Pd alloys to prepare "re-fired" filaments to simulate the behavior of co-fired clad wires. The sample is electroded in a four-point geometry using silver epoxy over the fired-on silver contacts.

Fired-on contacts have the disadvantage of obscuring the relationship between sintering conditions and transport properties, since an additional heat treatment is required. This is avoided by the second electroding method, in which contact pads are produced by sputtering silver onto the bare Y-123 filaments. Silver paint on the sputtered pad usually makes a satisfactory contact.

Figure 2.5.1 shows the resistive transition for a good bare Y-123 filament (027042C) made from jet milled powder in the form of a dry spun fiber sintered at 996°C in the tube furnace, and annealed two hours at 500°C in oxygen. This filament appears to be high quality Y-123, since it has quite low normal state resistivity for bulk Y-123, 60 $\mu\Omega$-cm at 100°K and 154 $\mu\Omega$-cm at 258°K. The temperature dependence in the metallic region is essentially linear at 0.53 $\mu\Omega$-cm/°K, which is similar to high quality single crystal Y-123[19]. The transition is sharp with an onset at 92.7 and zero resistance at 90.2°K.

The critical current measurements are done in a liquid nitrogen bath. Until very recently, all measurements were in zero applied field, reflecting self-field conditions. We are now beginning to collect data in an applied field up to one tesla. Filaments are mounted on a sample holder in a four point configuration. A computer controlled data acquistion system, operating on an algorithm described in the quarterly reports, increases the DC

---

[19]. J. Greybeal, M.I.T. personal communication

current in a step wise fashion to record voltage response as a function of current. This is converted to electric field vs. current density, with the critical current defined by an electric field criterion of 1 $\mu$V/cm. The data is taken well out into the normal regime to establish the "n-value" for the voltage-current relationship:

$$V/V_o = [I/I_o]^n$$

An example of the electric field-current density data for one of the more extensively studied filaments (3306C3) is displayed in Figure 2.5.2. The one microvolt/cm criterion is satisfied at about 720A/cm$^2$, which cannot be clearly distingushed on the scale of this plot. Data in the range of the criterion is more clearly displayed in a semilog version of the same data, Figure 2.5.3, which indicates the precision with which $J_c$ is defined and the noise level of the voltage gradient below the critical current density.

## CPS SUPERCONDUCTOR

DATE: 2−7−89

Tc
fiber #027042C



Tc $(\rho=0)$ = 90.2K
Tc (onset) = 92.7K
$\rho$ (100K) = 60 $\mu\Omega-$cm
$\rho$ (258K) = 154$\mu\Omega-$cm

TEMPERATURE (K)
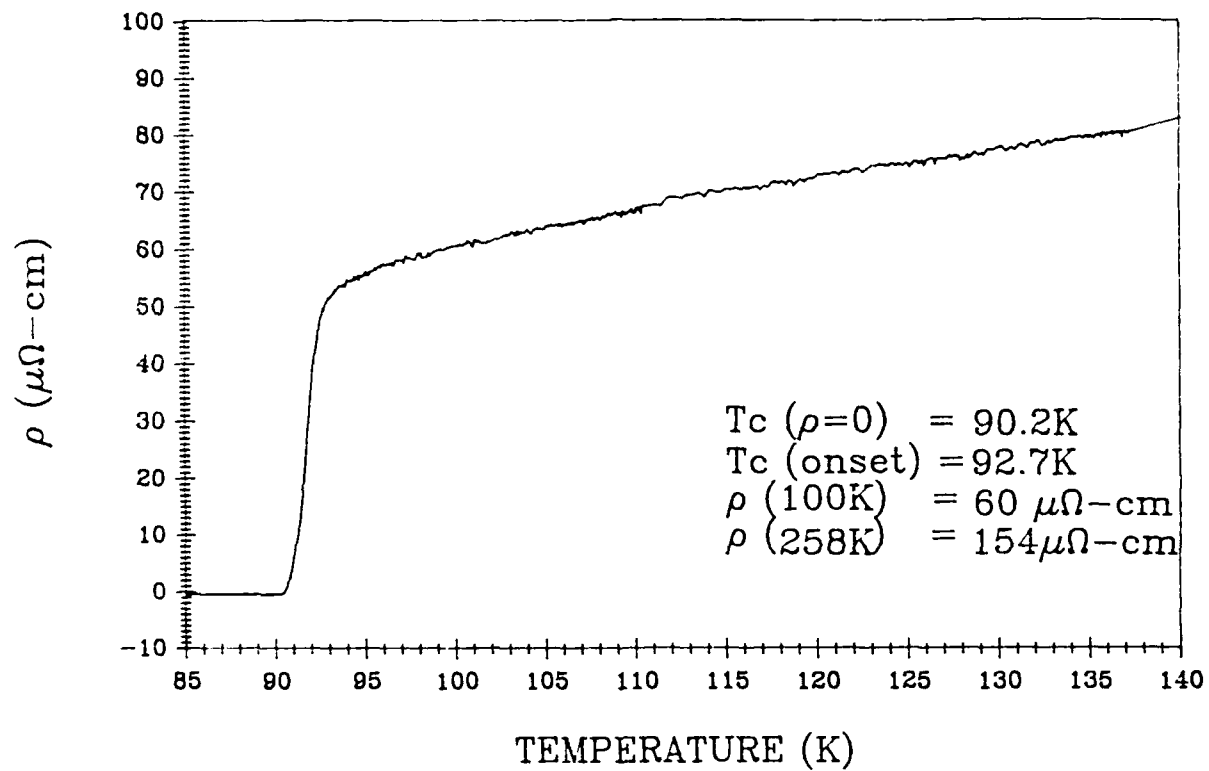
Figure 2.5.1    Resistive Transition for Bare Y-123 Filament Number 027042C
Made from Jet Milled Powder as a Dry Spun Fiber
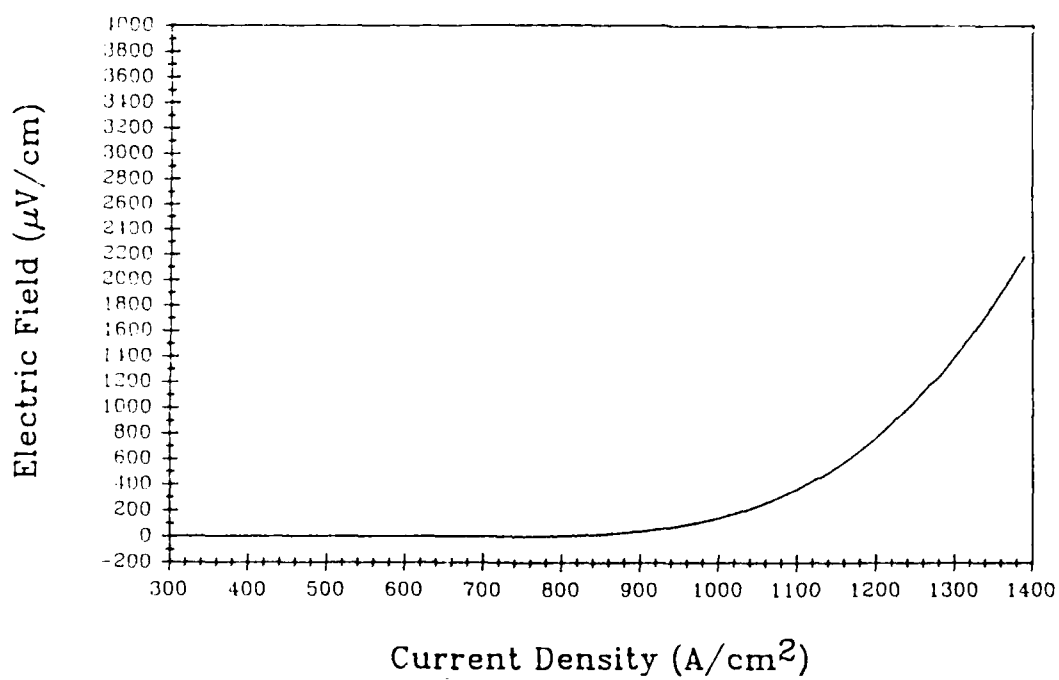
Figure 2.5.2    Electric Field versus Current Density for Filament 3306C3, A
                Melt Spun Fiber from Jet Milled Powder Sintered for Six
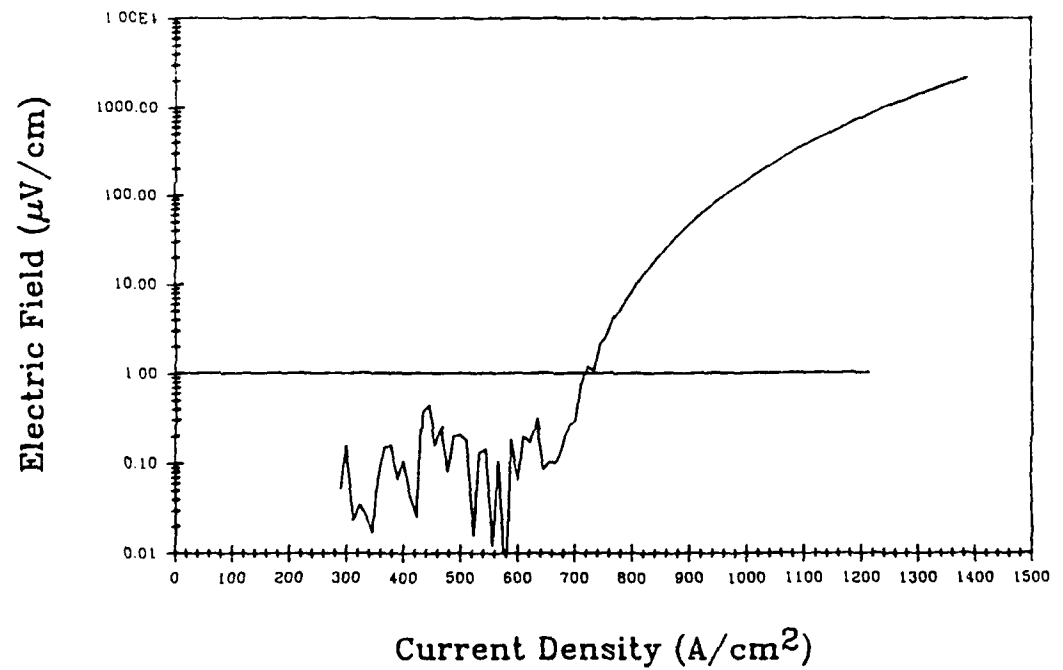                Passes At 996°C, with Fired-on Silver Contacts

Figure 2.5.3     Semi-Logrithmic Plot of Electric Field versus Current Density for Filament 3306C3

## 2.5.2    Critical Current Data for Single Pairs of Contacts

Refired filaments made from jet milled powder have displayed  some of the largest critical current densities yet seen in this program.  Specimen 2760C was made from a 140 micron diameter dry spun fiber prepared with the jet milled powder.  The filament was sintered in the tube furnace for the typical six passes at 996°C, and annealed for two hours at 500°C. After painting on a striped pattern of silver electrodes, the specimen was refired at 925°C for six passes, and given a second oxygen anneal. This specimen has an unusually sharp resistive transition and carried a critical current of 0.379 A, corresponding to a critical current density of 2450A/cm$^2$.  The electric field-current density data for this filament is shown in Figure 2.5.4.  A number of similarly processed filaments had critical current densities between 1500 and 2000A/cm$^2$.

These are higher self-field $J_c$ values than previously produced with other Y-123 powders. We are tempted to attribute the increase in $J_c$ to the use of the jet-milled powder, since recent data using jet-milled powders in melt spun fibers have similar current densities in both zone sintered and RTC sintered conditions.

Refired contacts were typically applied as stripes, with the major part of the Y-123 filament left bare.  This eliminated interference from a continuous metallic path, which complicates analysis of the resistive transition.  The bare filament surfaces were also thought to assist oxygen intercalation.  Several experiments were conducted with continuous silver coatings, however, which showed that complete oxygen intercalation can take

place through a continuous silver coating. Figure 2.5.5 shows the electric field vs. current density data for a filament which was completely coated with silver, refired, and oxygen annealed as before. The two traces show the apparent current density, using the total cross section, and the actual current density in the Y-123 after correcting for the metal/superconductor ratio of 1.1. The filament had a critical current density around 1300 $A/cm^2$, which is similar to bare filaments.

The first samples of the semi-continuously co-fired filaments appear to have similar transport properties as the filaments produced by zone sintering short fibers in the tube furnace. Figure 2.5.6 shows electric field vs. current density for a 100-micron diameter filament with a thin Ag/Pd cladding, sintered at 970°C in the RTC furnace, using the technique described in Section 2.3. This 4-cm long sample was taken from a 60-cm long filament and oxygen annealed at 550°C for 48 hours. The self-field critical current is 1413 $A/cm^2$.

Critical current measurements in applied magnetic fields are performed with a similar technique, with the sample immersed in liquid nitrogen in a simple cryostat. Fields between 25 and 10,000 gauss are applied with a Walker HSV-4H electromagnet. The magnetic field is measured with a Walker MG-3D gaussmeter with a transverse Hall probe inserted between the poles on the outside of the cryostat. The filament axis is perpendicular to the magnetic field. Figure 2.5.7 shows $J_c$ as a function of magnetic field for a zone sintered filament made from the most recent grade of 125-micron green fiber. This filament (3358) had the highest self-field $J_c$ produced to date-2600 $A/cm^2$. As expected, $J_c$ drops dramatically to about 10 $A/cm^2$ at 200 G, where it levels out up to fields of 800 G.
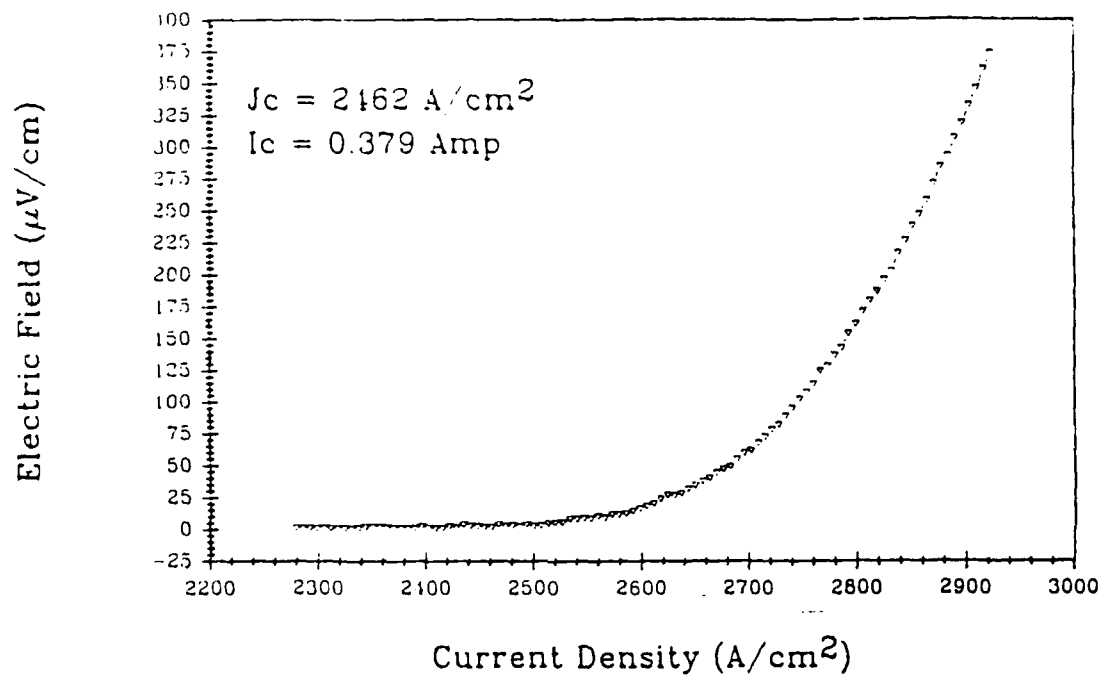
Figure 2.5.4    Electric Field versus Current Density for Filament 2760C
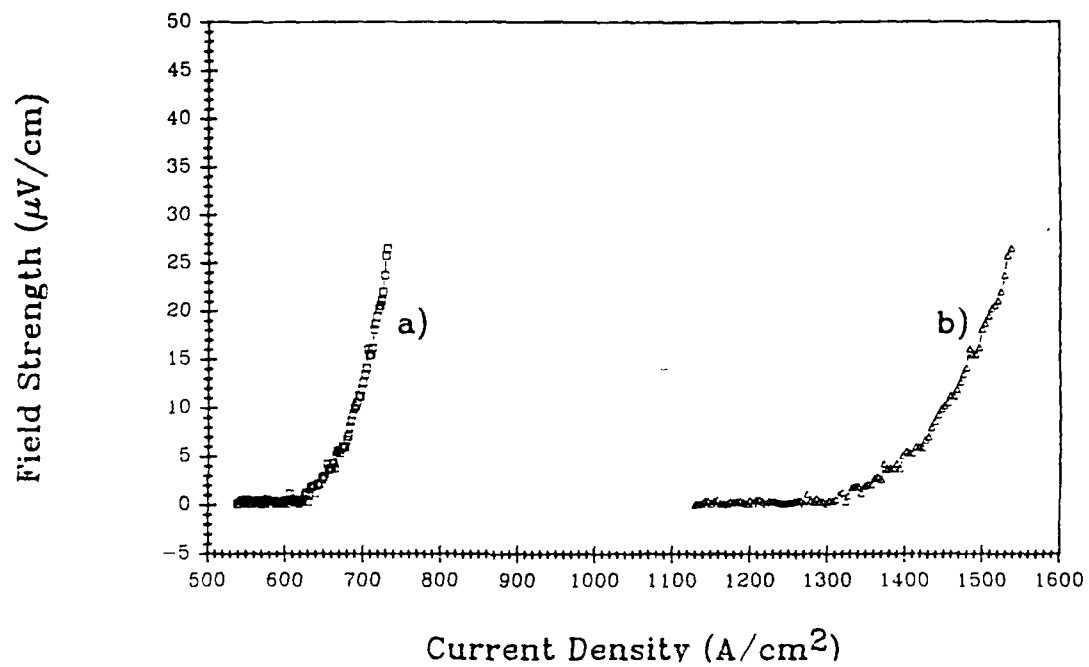
Figure 2.5.5      Electric Field versus Current Density data for Silver Clad Filament 2793A  a) Based on Total Cross Section b) Based on Y-123 Core Cross Section

DATE: 6-28-89

CPS Superconductor
Jc @ 0.5 Gauss
Fiber: 3499-1

$Jc = 1413 \ A/cm^2$
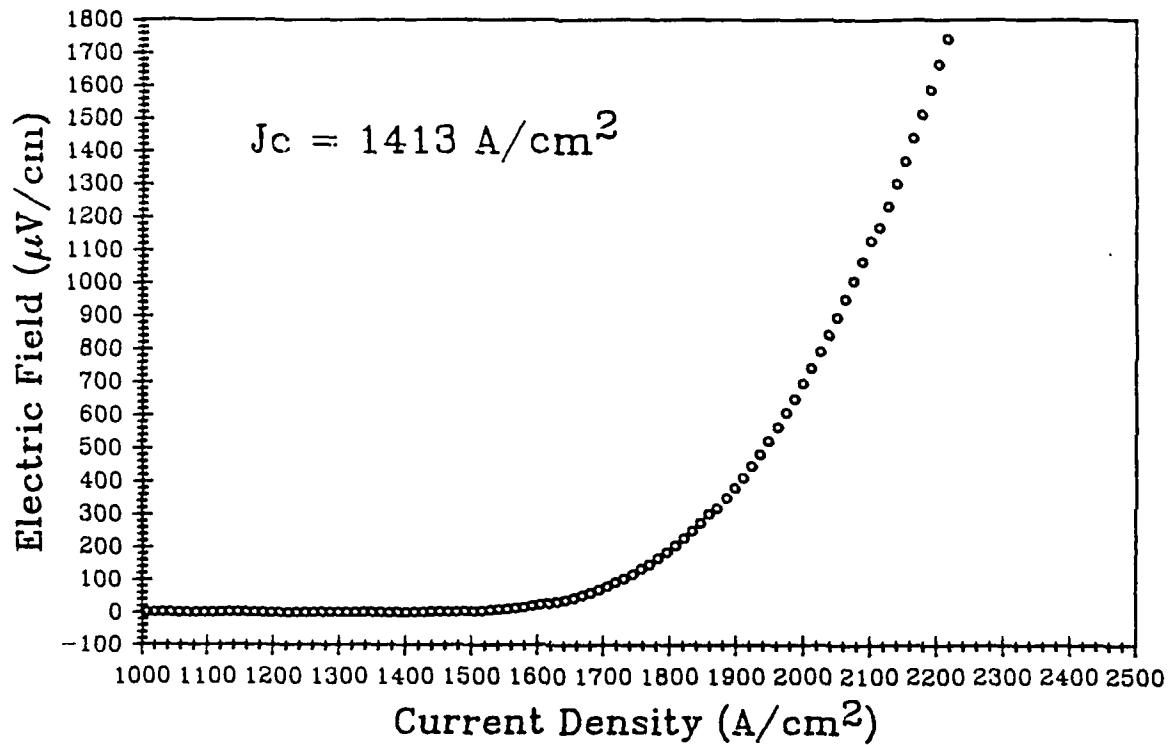
Figure 2.5.6    Self-Field Critical Current Density at 77°K for Ag/Pd
Clad Filament Semi-Continuously Co-fired at 970°C

DATE: 6–28–89

CPS Superconductor

Fiber: 3358
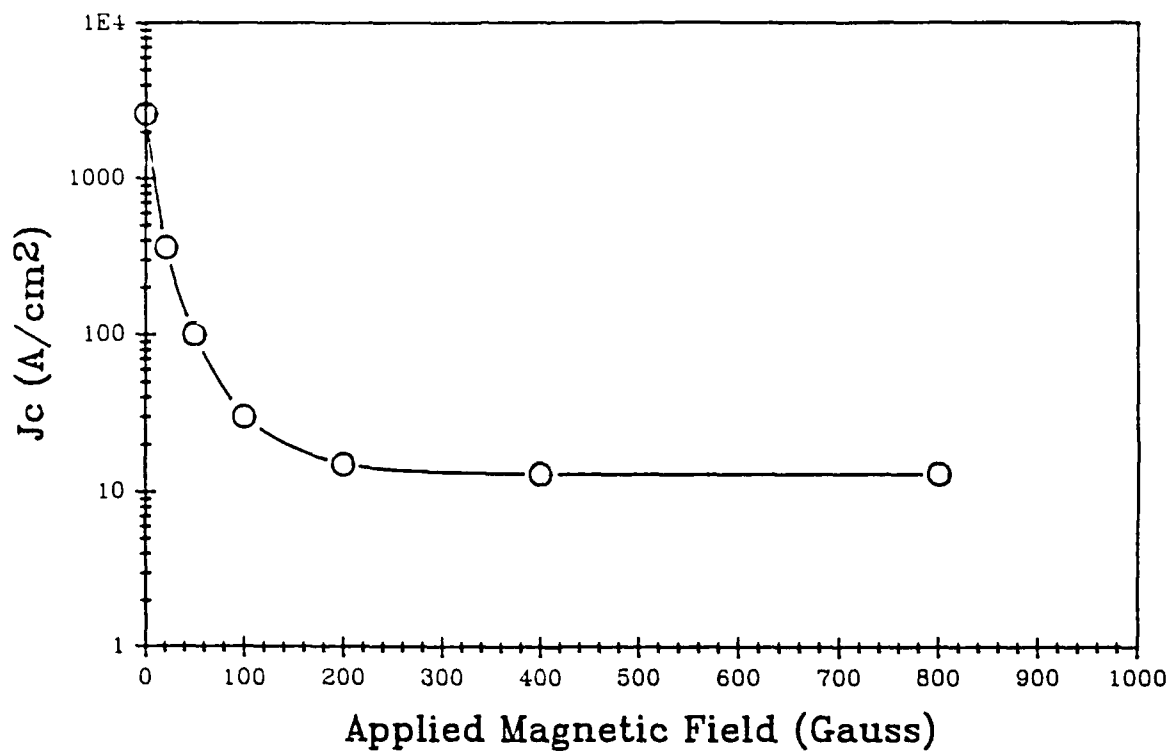


Figure 2.5.7      Critical Current Density vs. Magnetic Field for Bare
Y-123 Filament Zone Sintered for Six Passes at 996°C

2.5.3      Multiple Contact Experiments

A series of experiments were done with multiple measurements on single filaments provided with six contacts, so that up to five different segments could be characterized by permuting the voltage tap leads. This revealed, in some cases, a surprising variation in $J_c$ between different segments of the same filament. In the most uniform specimen, the critical current densities varied only 7% between the segments. The least uniform specimen had up to 60% variations in critical current density.

These experiments are conducted by painting six striped electrode contacts on a sintered filament and re-firing the filament as described above. The contacts were about 1 mm wide spaced 21 mm apart in the central segment, and 3 mm apart for the right and left segments. Contacts 1 and 6, at the ends of the filaments, were typically used for current leads. One pair of the remaining contacts (numbers 2,3,4, and 5) were chosen to determine the critical current density by the usual technique. A complete analysis involved measuring all the unique pairs, providing $J_c$ data for contact pairs 2-3, 3-4, 4-5, 2-4, 2-5, and 3-5. Repeated $J_c$ over the same voltage taps showed good reproducibility, even if the current leads were changed.

Figures 2.5.8 to 2.5.10 show the results of the multiple contact experiments for three filaments made from melt spun fiber containing jet milled powder. These all were zone sintered for six passes at 990°C, followed by a 2 hour oxygen anneal at 500°C. The re-fire conditions were six passes at 925°C, followed by another oxygen anneal. The first filament, 34008A, shown in Figure 2.5.8 has a critical current density of about 800A/cm² in the middle and left segments, while the right segment (segment 2-3) has a critical

current density of 750A/cm$^2$. The critical current measured across the whole specimen, between contacts 2 and 5, is about 760 A/cm$^2$, reflecting the fact that it intersects the low J$_c$ segment 2-3.[20]. Figure 2.5.9 shows that the right segment of filament 34008, with a J$_c$ of 640A/cm$^2$, determines the critical current of the whole filament, even though the center segment carries 720A/cm$^2$.

Filament 3306C3 has a similar history, but has a much larger range of J$_c$ values. Figure 2.5.10 shows that the center and left segments have values of 710 and 770A/cm$^2$, but the right segment 2-3 has a much larger critical current density of 1710A/cm$^2$. The J$_c$ of the whole filament, 2-5, is close to the worst segment.

Filament 3306C3 also exhibits differences in critical temperature from one location to another. Figure 2.5.11 shows the resistive transitions measured on over three segments of the filament. The T$_c$ is only 85°K over the center segment (measured between contact 3 and 4) and the left segment (contact 4 and 5), while there is a sharper transition at 88°K in the right segment of the filament (between contacts 2 and 3). As described above, the critical current density differs by a factor of 2.4 between the best and worst segment. The normal state resistivity is high for all segments, and is about

---

[20]. The values for the large spans, such as 2-5, should be slightly larger than the minumum J$_c$ for the intervening short spans. The discrepancy arises from the "electric field criterion", which assumes a uniform voltage distribution in the filament. This is not the case for an inhomogenous filament, since all of the voltage is dropped across the resistive segments. The 3 mm short span 2-3 reaches the 1 microvolt/cm criterion with a voltage drop of 0.3 microvolt. The 28 mm long span 2-5 does not reach the apparent electric field criterion until the voltage drop exceeds 2.8 microvolts. Thus there is bias in the criterion which makes the J$_c$ values slightly larger for larger spans.

40% higher in the center and right segments. We are attempting to identify the reason for the difference in these properties.

We are continuing multiple contact experiments for several reasons. First, we hope to use them to pinpoint the poorer regions of the filaments, which can then undergo detailed microstructural examination in an effort to relate microstructure to properties. Secondly, it is an economical way to gather data on the statistical variation of $J_c$ with segment length. This data is particularly important. We must use short length specimens to characterize continuous wire, so the theoretical basis for such extrapolation must be established. It may be that "weak linked" superconductor filaments, with the critical current for the entire filament governed by its worst segment, would have $J_c$ values distributed according to extreme value statistics. This could lead to a Weibull distribution function governing the $J_c$ statistics. This has serious implications for producing long lengths of weak link wire able to carry even the modest critical currents seen in short filaments.

VOLTAGE TAP NUMBER
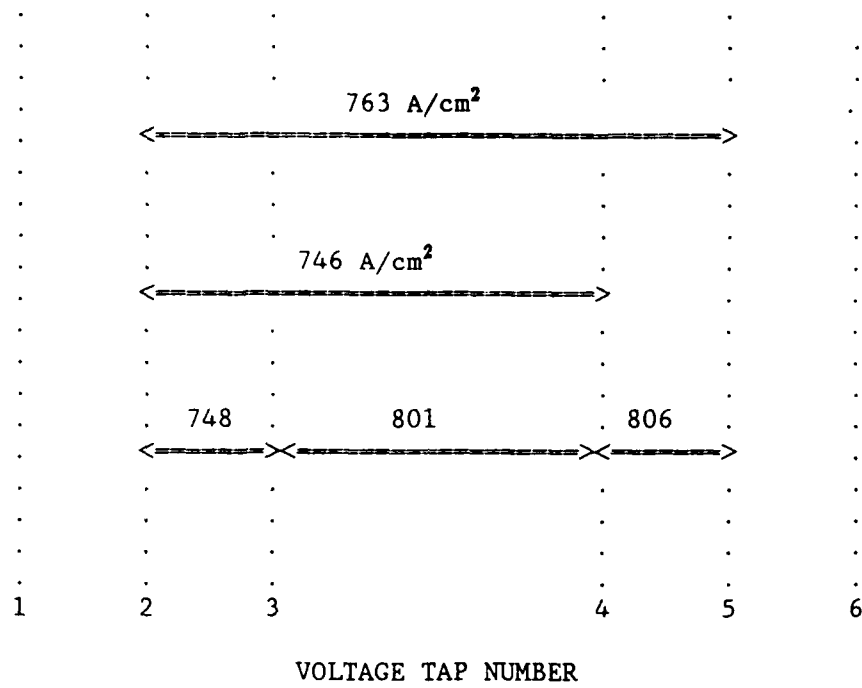
Figure 2.5.8     Critical Current Density Measured Between Multiple
                 Pairs of Voltage Taps on Filament 34008A

640 A/cm$^2$

690

1710    710    770

1        2              3              4              5        6

VOLTAGE TAP NUMBER

Figure 2.5.9        Critical Current Density Measured over Multiple Pairs
                    of Voltage Taps on Filament 34008

760 A/cm$^2$

640     720     710

1     2             3             4             5     6
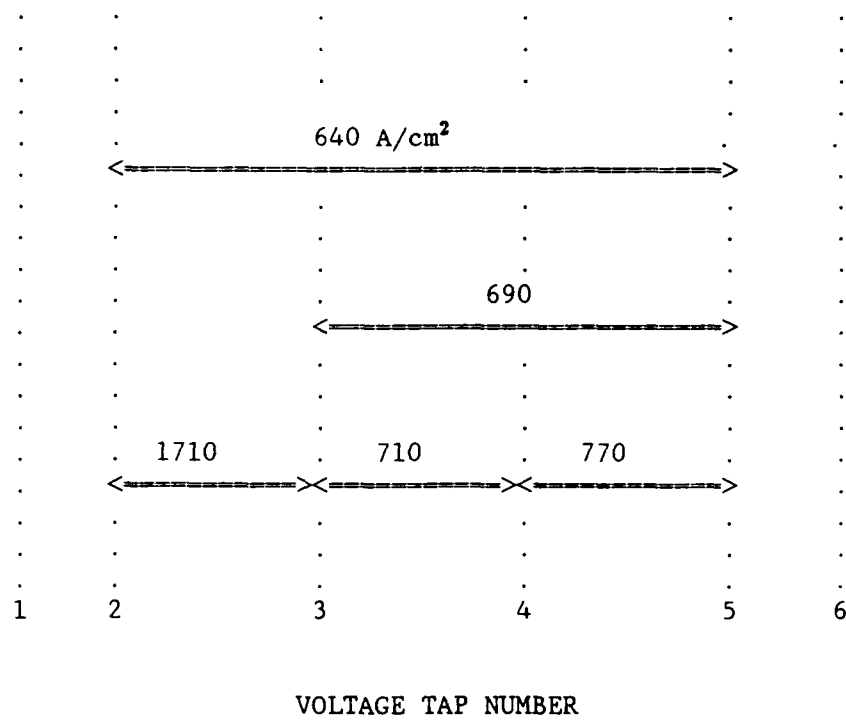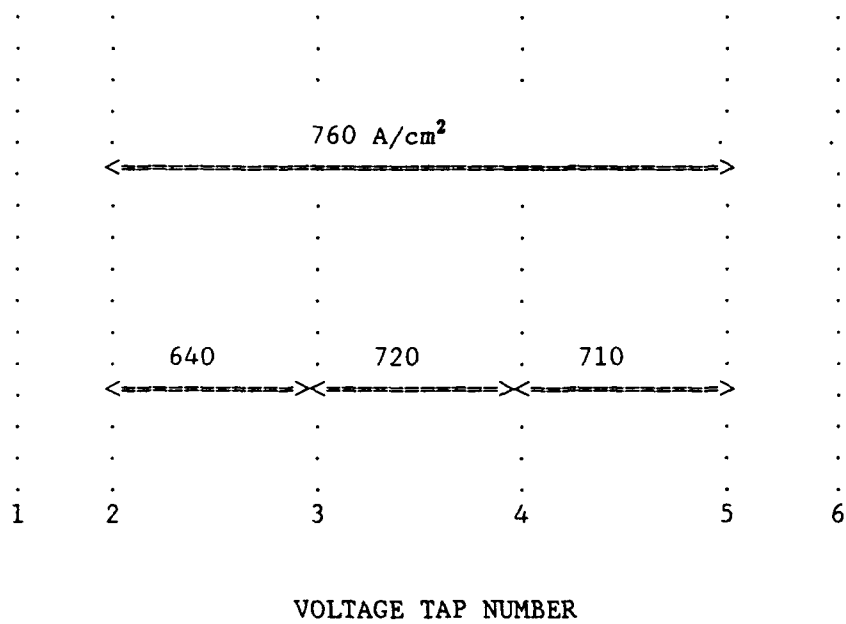
VOLTAGE TAP NUMBER

Figure 2.5.10     Critical Current Density Measured over Multiple Pairs
of Voltage Taps on Filament 3306C3
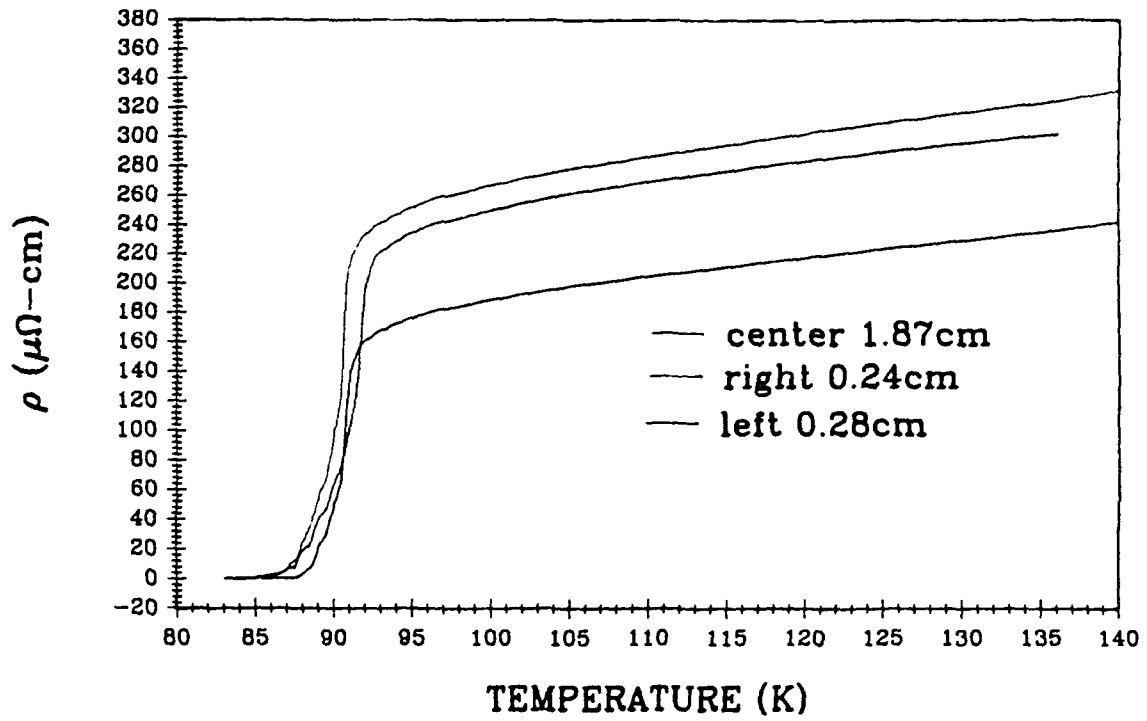
Figure 2.5.11       Resistive Transitions Measured over Multiple Pairs of
                    Voltage Taps on Filament 3306C3

2.5.4        Electrical Properties of Filaments with Deposited Base Metals

The transport properties of a number of filaments which had been clad with various metals by outside collaborators have been characterized.  As discribed in Section 2.3, Lashmore and Stafford of NIST successfully deposited an aluminum alloy coating from a $MnCl_2$ doped $2AlCl_3:NaCl$ molten salt electrolyte.  The claddings were dense 4.7 micron thick adherent deposits of an amorphous alloy of approximate composition 70 wt% Al-30 wt% Mn.  No evidence of microstructural damage could be found by SEM examination.

The substrate filaments were still superconducting after molten salt deposition of the Al-Mn, as indicated by our simple float test.  More quantitative data was provided by Lydon Swartzendruber of NIST, who measured the magnetization of bare and clad filaments at 77°K.  Swartzendruber's data are presented in Figure 2.5.12.  The magnetization of the Al-Mn clad filament suggested a Meissner fraction of 38% at 0.05kOe and 28% at 0.30kOe.  This was actually higher than bare filaments from the same batch, which showed Meissner fractions of 42% at 0.05kOe and 10% at 0.30kOe. The bare filament, however, had been exposed to laboratory air for more than five months before measurement.

In spite of the superconducting Y-123 substrate, the clad fiber displayed no resistive transition.  Figure 2.5.13 is the resistivity trace for the Al-Mn clad filament, indicating normal metallic behavior with no hint of any change around the critical temperature.  The room temperature resistivity of 25 $\mu\Omega$-cm was calculated assuming that all of the current was carried in the 5 micron thick coating.  Apparently a highly resistive or insulating barrier

has formed between the base metal alloy and the Y-123 which prevents current transfer to the superconducting core.

Similar behavior was found with Y-123 filaments clad with aqueous electrochemical methods. Professor Stanley Bruckenstein of SUNY-Buffalo deposited copper directly onto the Y-123 by electroless plating. When these were found to be no longer superconducting, he developed a procedure to deposit silver onto the Y-123, followed by copper on the silver. We received for analysis two types of specimens of clad 230 micron Y-123 filaments. One set was clad with a thin 2-3 micron coating of silver with a globular morphology, while the second had a thick 7-8 micron silver coating with a two micron copper overlay. The microstructure of the thicker coating suggested it was a strongly adherent brittle metal deposit. Both types of clad filament were superconducting by the float test. Figure 2.5.14 shows the resistivity data for these samples, which have no indication of a resistive transition, demonstrating that current is not being transfered from the cladding to the substrate Y-123 filament apparently due to a high resistance barrier at the metal/ceramic interface. These are apparent resistivities using the total filament cross section. The lower value for the the specimen with the silver plus copper cladding probably reflects the thicker cladding. Specimens with the thinner silver cladding were measured as received and after annealing at 500°C in an attempt to remove the suspected insulating barrier. The anneal did not remove the insulating barrier, but did decrease the normal resistivity, probably by consolidating the globular silver layer. In more recent experiments, areas were masked from the deposited cladding so that electrical contact could be made to the Y-123 substrate. This demonstrated that the

quality of the bulk Y-123 filament beneath the insulating layer is not affected by the deposition.

With the help of several collaborators, we have now had preliminary evaluations of CVD aluminum, electrodeposited aluminum, electrodeposited copper and electrodeposited silver. All have developed resistive barriers. It is clear that base metals cannot be directly deposited on Y-123. For future work, we will supply our collaborators with Y-123 filaments with co-fired silver coatings to act as diffusion barriers between the superconductor and the deposited metal.
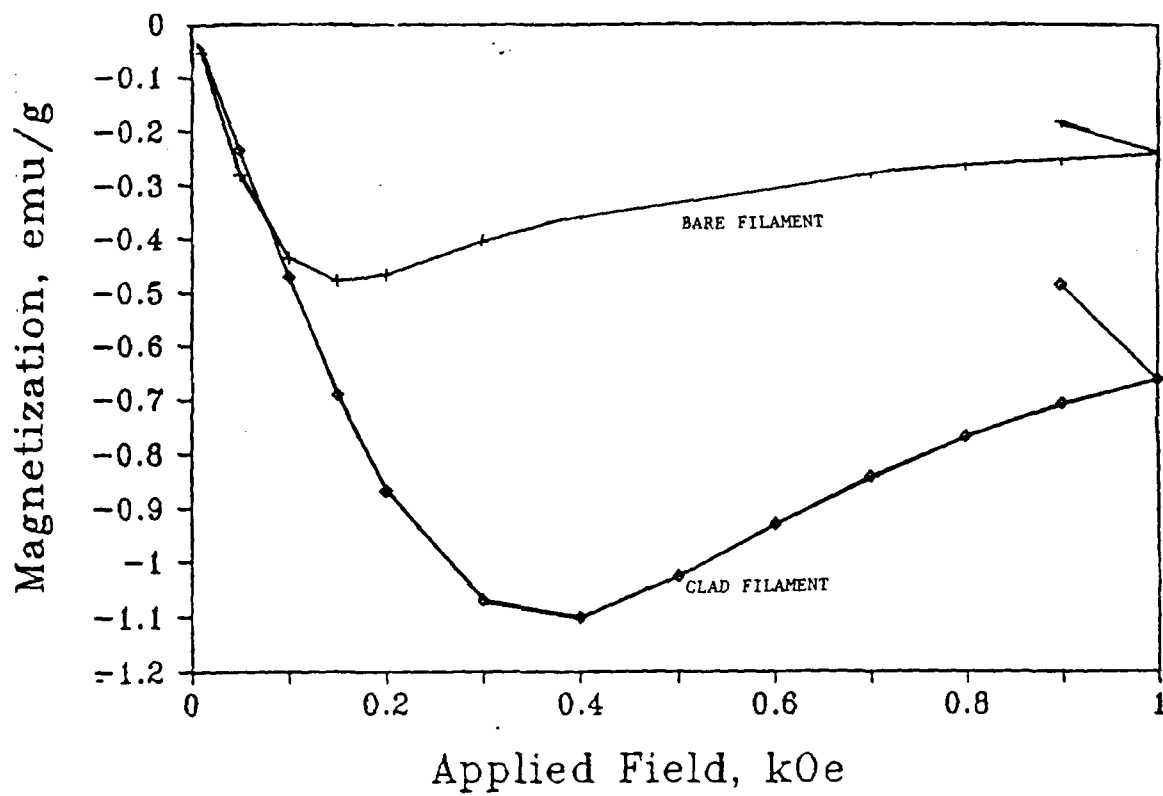
Figure 2.5.12     Magnetization at 77°K for Bare and Al-Mn Clad Filament
                  Produced at NIST by Stafford and Lashmore. Data
                  Provided by Lydon Schwartendruber
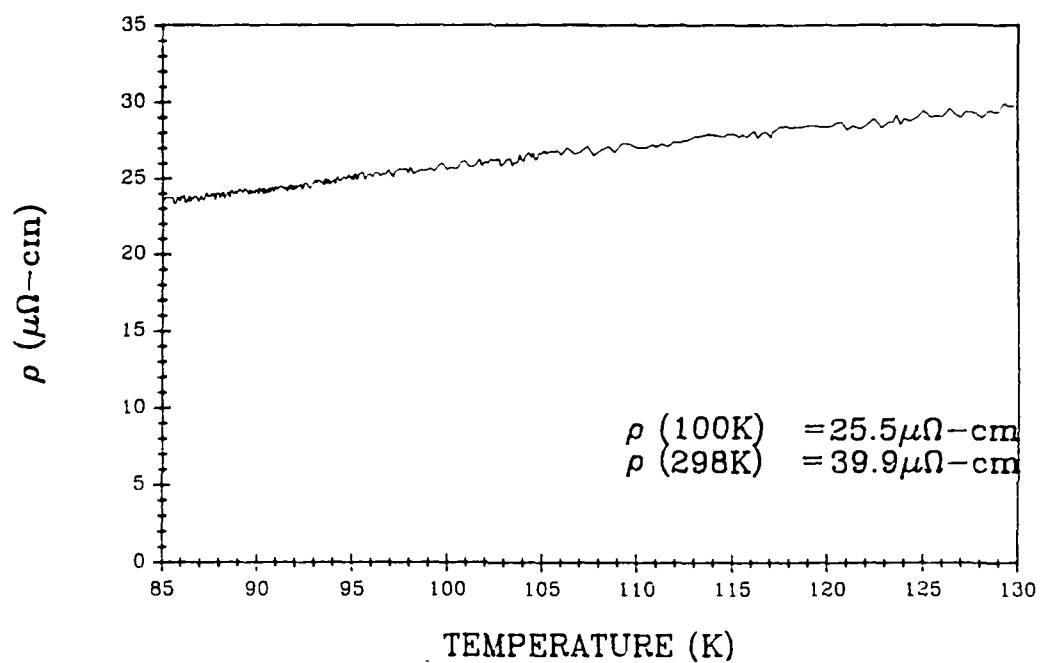
Figure 2.5.13      Resistivity versus Temperature for the Y-123 Filament
Clad with Electrodeposited Al-Mn at NIST
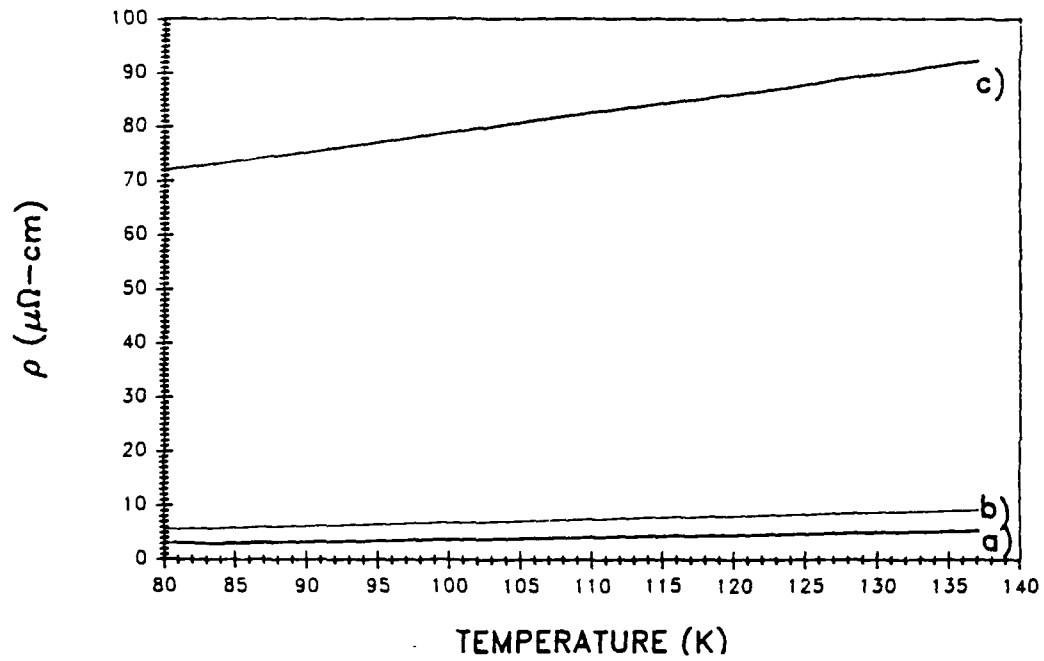
Figure 2.5.14    Resistivity versus Temperature for Y-123 Filaments with Plated Cladding for SUNY-Bufallo  a) Cu Deposited on Ag  b) Thin Ag Coating After Anneal  c) Thin Ag Coating As-Deposited

2.5.5        AC Susceptibility of Y-123 filaments

Susceptibility tests were performed on a silver coated Y-123 filament and Y-123 powder using a Model 7000 Susceptometer at Lake Shore Cryotronics in Westerville, Ohio.  Figure 2.5.15 shows the temperature sweep of the volume susceptibility for a post fired zone sintered Y-123 filament. The 110-micron diameter filament was about 1.3 cm long, which corresponds to a mass of 0.8 mg. The filament axis was aligned nearly parallel to the magnetic field by placing it into a glass capillary tube of 300 micron outside diameter (280 $\mu$m ID) and placing the capillary tube into a 500 $\mu$m diameter hole which had been drilled down the center of the nylon sample holder.  Using this configuration, the filament can be no more than 1.63° off axis.  The angular dependence of the demagnetization factor is not known, but we can estimate an upper limit to the demagnetizing effect by assuming that tilting the cylinder has the effect of shortening the fiber length and increasing its diameter. Demagnetization factors, D, for long thin ellipsoids of rotation can be approximated, when k >> 1 (where k is the ratio of length to diameter) by [21]

$$D = (\ln(2k) - 1)/k^2$$

using this equation, $D_|$ = $3.2 \times 10^{-4}$ for the parallel case and $D_\backslash$ = $4.08 \times 10^{-3}$ if the filament is off axis.  Calculating $X_{int}$ from $X_{ext}$ = -1.0813 (The value measured for this filament at 10.10K) gives $X_{int,|}$ = -1.0809 and $X_{int,\backslash}$ = -1.0766.  The error from being off axis is much less significant than other errors.  Presumably the most significant of these is the estimation of the diameter of the Y-123 filament under the silver coating.

---

[21]   S. Chikazumi and S.H. Charap:**Physics of Magnetism**(Robert E. Krieger Publishing Co., Malabar Fla, 1986)

It is possible that the slope of the transition is adversely affected by using a frequency of 200 Hz and a field of 80 A/m. These values were chosen to enhance the signal, but can in some cases artificially broaden the transition.

Data was also taken with a piece of this filament approximately 3 mm long oriented perpendicular to the field at 4.2K. Using D – 0.5, the $X_{int}$ was 0.92. Data taken at four different field strengths yielded the same value for susceptibility to within 1%, but it should be noted that the transition broadening field effects do not have a noticeable effect far from the transition. The imaginary part of the data ($X''$) shows the expected peak at the transition, which can be used to measure the width of the transition.

The significant aspects of this data are that it is possible to acquire susceptibility data on a small piece of a single filament held approximately parallel to the field. The data show that the silver coated filament was completely superconducting with a transition beginning between 92°K and 90°K and approximately 90% complete by 80°K.

Magnetic susceptibility has been proposed as a method to characterize the quality of HTSC powders, so the behavior of CPSS Y-123 powder was determined for two types of powder made by jet-milling the calcined Y-123 described in Section 2.1. The measurements were done on powders which had received an additional anneal at 500°C in oxygen. Both were fully orthorhombic. The finer powder was the standard 1.7-micron jet milled material, and the coarse powder was jet milled to an average size of 4.6 microns. Figure 2.5.16 shows the data from those samples. Neither of the powder samples show perfect diamagnetism, nor do they display a peak in the imaginary susceptibility. The real part of the susceptibility has a significant particle size effect between 1.7 and 4.6 microns.

Sample 2987A:  D = 0

Fixed Point, 200 Hz, 80 A/m
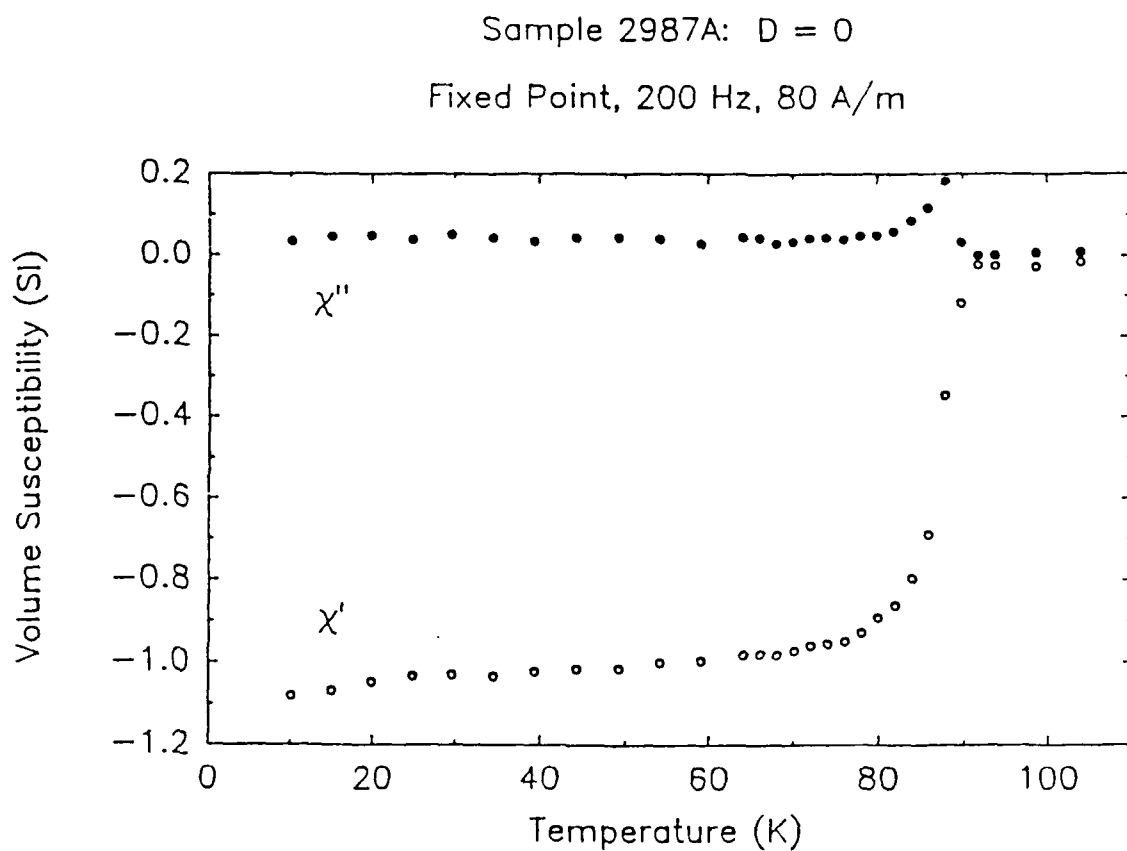


Figure 2.5.14A    Real and Imaginary Volume Susceptibility of Y-123
                  Filament as a Function of Temperature. The 0.124 $mm^3$
                  Filament Was Oriented Parallel to the Field.

Sweep Mode, 100 Hz, 80 A/m
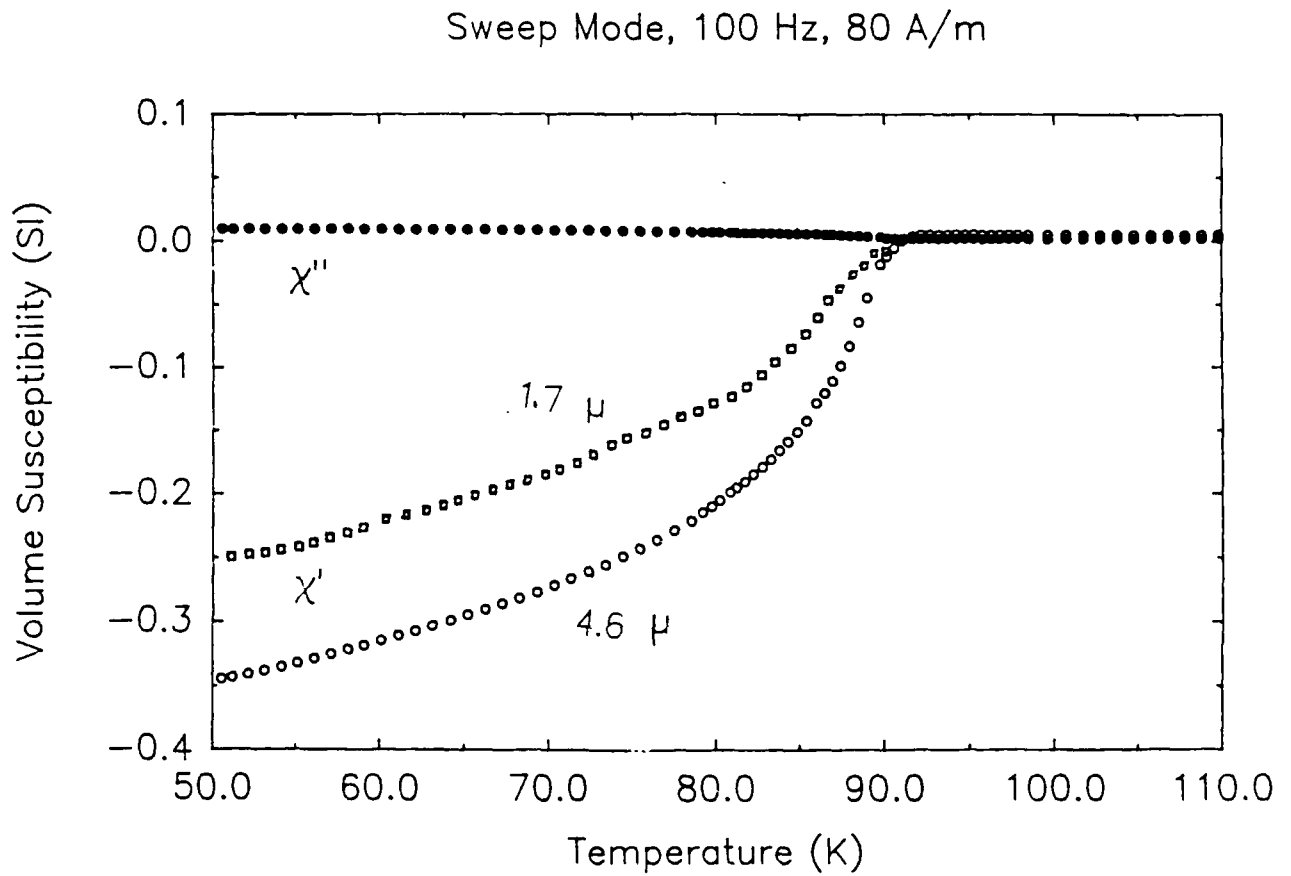


Figure 2.5.15      Real and Imaginary Volume Susceptibility vs.
Temperature for 1.7 micron and 4.6 micron Y-123 Powder

Recent studies[22,23] have shown that high temperature superconductor powders, produced by crushing good superconducting material, show a weaker diamagnetic signal than the parent sintered sample, apparently due to the unconsolidated nature of the powders rather than an intrinsic lack of superconductivity. The low diamagnetism and particle size dependence of these powders are probably caused by a similar artifact.

2.5.6    Mechanical characterization of sintered Y-123 filaments

The thrust of the wire manufacturing task is to produce Y-123 wire flexible enough to be wound into coils in its final state. In the absence of actual data, theoretical calculations have been performed to relate filament diameter to the bend radius which can be tolerated before failure. Confirming these results with real data is a high priority task. As soon as continuously sintered Y-123 filaments were available, a simple bend test was devised to directly determine the tolerable bend radii, and derive tensile strain at fracture. The ends of sintered filaments, 100 microns in diameter, were fixed onto a flexible metal rule with adhesive tape. The rule was bent over a chart which indicated its radius of curvature in increments of 0.5 cm, and the sharpest radius prior to fracture was recorded. Sintered specimens were measured in their as-sintered tetragonal state and after oxygen annealing to the superconducting orthorhombic state. (These specimens were from the same lot that produced 2600 $A/cm^2$.)

---

[22]   T.L. Hylton and M.R. Beasley, Phys. Rev. B 39, 9042 (1989).

[23]   D.-X. Chen, R.B. Goldfarb, J Nogués, and K.V. Rao, J. Appl. Phys. 63, 980 (1988).

The data for these bend tests are presented in Table 2.5.1 for as-sintered tetragonal filaments and in Table 2.5.2 for orthorhombic filaments made by oxygen annealing the sintered material. The elastic strain prior to fracture is calculated from the bending radius using Equation 2.1. This can be considered an accurate value for strain near fracture. The apparent "strength" in Tables 2.5.1 and 2.5.2 are nominal values for the fracture strength obtained by multiplying the strain by Loehman's values of elastic moduli for the tetragonal and orthorhombic Y-123. These should not be considered accurate due to the irreproducibility of elastic constants for ceramic Y-123. The lower "strength" of the orthorhombic filaments largely reflects the much lower elastic modulus. The average strain before fracture of both types of filaments is actually the same, at 0.121%. The fracture surfaces of two of the tetragonal filaments are shown in Figure 2.5.16. There appear to be no obvious defects, such as large voids or oversized grains, so it can be presumed that the strength limiting defects are typical microstructural features.

These data can be fit to a Weibull distribution function[24] for the probability of fracture as a function of normalized length, L (= specimen length/1 meter), and fracture strain, $\epsilon$, to derive the Weibull modulus, m, and characteristic strain, $\epsilon_o$:

$$F = 1 - \exp(-L(\epsilon/\epsilon_o)^m)$$

The Weibull distribution parameters for the tetragonal filament, obtained by least squares fitting the data of Table 2.5.1, are: m=6.2 and $\epsilon_o = 0.00076$. The characteristic strain $\epsilon_o$, is equivalent to a characteristic radius of curvature, $R_o = 6.4$ cm, i.e., a one-meter length has a 63.3% probability of

---

[24] The use of Weibull functions of this form for describing the strength distribution of glass fibers is well established, see for example, R. Olshansky and R.D. Maurer, J. Applied Physics, 47, 4497, (1976)

failure at this radius of curvature. If the annealed filament data set is plotted with the tetragonal data, the combined distribution parameters are very similar: $m=6.2$ and $\epsilon_o = 0.00078$. However, fitting the orthorhombic data by themselves gives quite different distribution parameters: $m=5.6$ and $\epsilon_o = 0.00038$, which indicate that the orthorhombic filaments are significantly weaker. In this case the characterisitic radius of curvature is 12.4 cm.

A practical coil of HTSC wire requires on the order of a kilometer of wire. A very long extrapolation is needed to predict the survival probability of 1000 meter long wires from data on 5 cm long specimens. However, this is a key issue for the success of the program, so we will hazard this extrapolation and attempt to predict survival probabilites for long coils. Using the Weibull parameters from these preliminary data, the probability of winding a 1000-meter coil without a fracture, or survival probability, P, can be calculated from:

$$P = \exp\{-1000(\epsilon/\epsilon_o)^m\} = \exp\{-1000(R_o/R)^m\}$$

The survival probability for a 1000-meter bare filament is plotted as a function of the radius of the coil in Figure 2.5.16 for bare tetragonal and orthorhombic filaments. To have a 50% chance of success, the 100-micron bare Y-123 filaments can withstand no tighter bending than about 22 cm and 46 cm for the tetragonal and orthorhombic filaments, respectively. Clearly, it is impractical to wind field coils from unclad filaments.

One can roughly model the behavior of the silver alloy clad wire by assuming that the same flaw population dominates fracture, with the only role of the cladding alloy being to apply a compressive axial stress to the brittle filament. In Section 2.1.2.2 it was shown that a Ag/Pd alloy cladding can apply a compressive axial stress on the order of 50 MPa, corrosponding to

a compressive axial strain of $\epsilon_r = -0.00038$. The net strain experienced by the clad fibers is then:

$$\epsilon_{net} = \epsilon(R) - \epsilon_r$$

which modifies the expression for survival probability to:

$$P_{clad} = \exp\{-1000([\epsilon - \epsilon_r]/\epsilon_o)^m\}$$

$$\text{for } \epsilon - \epsilon_r \geq 0$$

The calculated survival probability for the clad wires is also displayed in Figure 2.5.17. The clad wires have high survival probability for curvatures as tight as 10 cm, which is the design radius for the homopolar motor field windings (see Section 3).

This exercise is a long extrapolation from a skimpy database, but serves to illustrate the vital role of the metal caldding. Notice that the effect of the residual strain from the cladding is to define a radius of curvature $R_{eff} = D/(3\epsilon_r)$ at which P =100%, since the residual compressive strain exactly cancels the tensile flexural strain. This is equivalent to truncating the Weibull distribution, so that at R values greater than $R_{eff}$, a a design can be deterministic rather than probabalistic. Operating under conditions where the residual stress dominates, so that $\epsilon - \epsilon_r \leq 0$, will assure that a coil of arbitrary length can be wound.

Table 2.5.1

MECHANICAL PROPERTIES OF 100-MICRON
AS-SINTERED TETRAGONAL Y-123 FILAMENTS

| Bend Radius Before Fracture | Strain | Strength[25] |
|---|---|---|
| cm | % | MPa |
| 6.0 | 0.083 | 109 |
| 6.0 | 0.083 | 109 |
| 5.0 | 0.10 | 131 |
| 4.5 | 0.11 | 145 |
| 4.5 | 0.11 | 145 |
| 4.0 | 0.125 | 164 |
| 4.0 | 0.125 | 164 |
| 3.5 | 0.143 | 187 |
| 3.5 | 0.143 | 187 |
| 3.5 | 0.143 | 187 |
| 3.5 | 0.143 | 187 |
| 3.5 | 0.143 | 187 |

Table 2.5.2

MECHANICAL PROPERTIES OF 100-MICRON
$O_2$-ANNEALLED ORTHORHOMBIC Y-123 FILAMENTS

| Bend Radius Before Fracture | Strain | Strength |
|---|---|---|
| cm | % | MPa |
| 5.5 | 0.091 | 75 |
| 5.0 | 0.10 | 83 |
| 4.5 | 0.11 | 91 |
| 4.0 | 0.125 | 103 |
| 4.0 | 0.125 | 103 |
| 4.0 | 0.125 | 103 |
| 4.0 | 0.125 | 103 |
| 3.5 | 0.143 | 118 |
| 3.5 | 0.143 | 118 |

---

[25]. Apparent strength from stress at fracture using as elastic moduli 131 GPa for tetragonal Y-123 and 82.7 GPa for orthorhombic Y-123. R.E. Loehman et al., J. American Ceramic Soc., 72,(4),669-674, (1989)
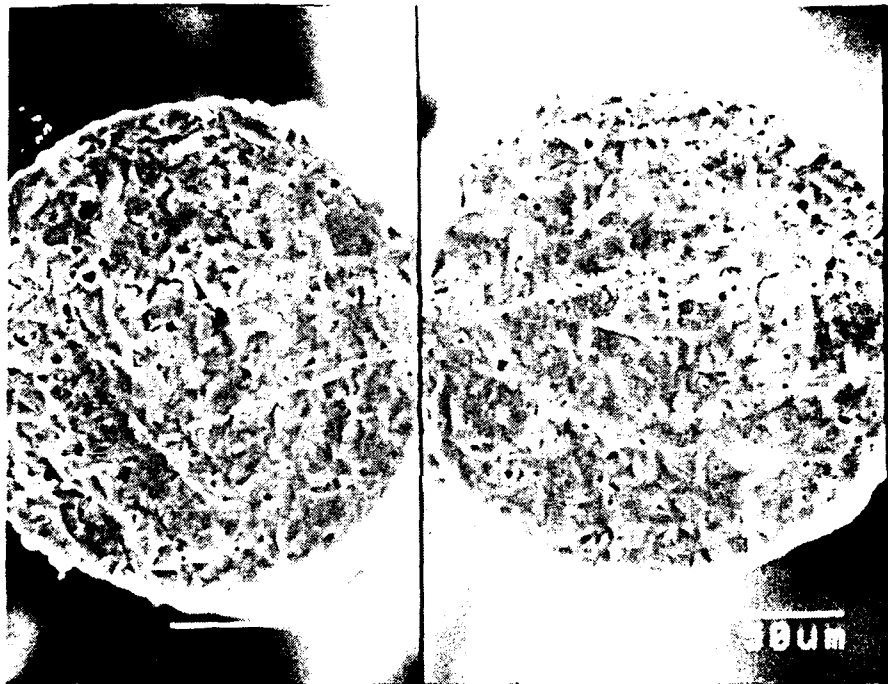
Figure 2.5.16    Fracture Surfaces of Tetragonaly Y-123 Filaments
                 Left: Fractured below 4 cm bending radius
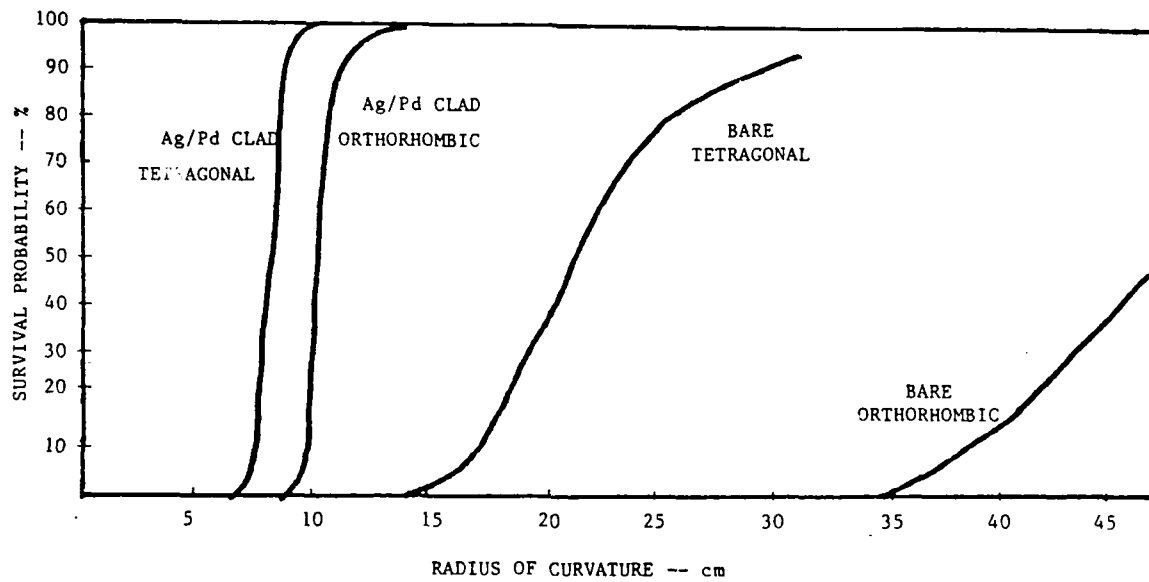                 Right: Fractured below 3.5 cm bending radius

Figure 2.5.17    Calculated Survival Probability for a Coil Containing
                 1000 Meters of 100-Micron Wire as a Function of Radius
                 of Curvature

## 2.6        Summary

Signifiant progress has been made during the first year of this program on the development of composite HTSC wire.  The program is close to the original schedule on all major tasks. Prototype clad wire has been made in about half-meter lengths, and the first coils of wire for the proof-of-principle motor are expected in the second quarter of the coming year.

The design of flexible clad-fiber HTSC wire was refined for both ribbon conductor design and a simpler monofil wire design.  The relationship between diameter and bending radius was quantified, and compared with preliminary data.  The strength of metal clad fiber was calculated. Concepts and methods for producing filament transposition were defined.

A process was placed into operation to manufacture reproducible phase pure Y-123 powder in kilogram quantities.  This powder is made by solid state reaction, controlled to yield at least 98 wt% of the Y-123 phase, with traces of barium carbonate, barium cuprate, and "211".  Jet-milling is used to produce a highly sinterable powder with an average particle size of $1.6 \pm 0.2$ microns and specific surface area of $2.5 \pm 0.3$ m$^2$/gm.  All of the recent Y-123 green fibers are made with this powder.

A novel melt spinning process has been developed at Albany International Research Company to manufacture continuous green fiber containing 50 vol% Y-123 carried in a polymer blend. The melt spun fibers are made with conventional fiber spinning equipment with a process which readily lends itself to scale-up.  Consequently, melt spinning has been adopted as the preferred method of producing green fiber.  The solvent-based dry spinning method is used only for small experimental lots.

A large number of thermoplastic resins, carrier polymer-lubricant blends, and processing conditions have been explored. The evaulations were based on processibility, binder burnout behavior, and properties related to continuous sintering of fibers. High density polyethylene-based systems presently make the best green fiber with Y-123. Melt spun green fiber has been prepared with diameters ranging between 50 and 330 microns at lengths up to about 0.5 kilometer. The current standard green fiber diameter is 125 micron in diameter. This grade of fiber is being used to supply the cladding and sintering operations. Development efforts continue to reduce fiber diameter down to about 10 microns, to allow a more flexible wire to be produce.

The feasibility using braided Y-123 green fiber to produce multifilamentary wire with transposed filaments has been supported by recent success in producing continuous braids from the HDPE-based green fiber using a conventional braiding machine. Earlier work on simple braids showed that binder burnout and sint ing is possible with braided green fiber.

The Y-123 green fiber can be coated with a silver or Ag/Pd alloy coating, which can be co-fired with the Y-123 during sintering. For the ribbon wire, the silver alloy coating provides a wettable surface for adhesion of the solder and acts as a barrier isolating the Y-123 from the solder. For the monofil wire, the silver alloy coating is the primary metallization, and serves all of the functions of the stabilizing metal. Presently about 100 meters of fiber are coated continuously. The system is still being developed to produce thicker, more uniform coatings.

The green fibers are sintered by two techniques. The older method, multiple zone sintering, produced 10-cm long samples by moving the fiber through the hot zone of a small tube furnace. Typically, a Y-123 fiber was exposed to about six repeated passes through the furnace, each involving

0.5- 5 minutes at peak temperature. Zone sintering was used to simulate continuous sintering, and to evaluate the sinterability of experimental powders and fibers, and to produce dense Y-123 filaments with self field critical currents as high as 2600 A/cm$^2$. Microstructure development during zone sintering has been characterized.

A commercial belt furnace was modifed make it suitable for continuous sintering of fibers. This is currently being used to develop a process for continuous sintering of bare and Ag-coated Y-123 fiber. Green fibers are fed into a belt furnace for binder removal and sintering. This process is the prototype for reel-to-reel manufacture, and has replaced the zone sintering method. To progress from the tube furnace to the belt furnace it was necessary to overcome a number of practical problems related to the burnout characteristics of the green fiber, adhesion of the fiber to the belt cover, and some mechanical difficulties with the furnace itself. At present, fibers can only be semi-continuously sintered. The filament length was limited by the present need to pass the fibers through the belt furnace several times for binder burnout, presintering, and sintering.

The achievement of semi-continuous fiber sintering is significant because it demonstrates that coated green fiber an be carried through binder burnout and densification continuously without breaking. This indicates that the manufacture of composite wire from green fiber is feasible. Experiments on meter-length samples are in progress to define an optimal heating schedule. Based on these results, additional heating zones will be installed on the belt furnace so it can operate in true reel-to-reel mode.

A solder reflow method was developed to clad fibers to make the ribbon wire. A cladding machine has been built to do continuous cladding of continuous sintered Y-123 filaments. This machine is designed to fabricate

the ribbon by sandwiching a sintered fiber array between copper foil strips and solder bonding them. The cladding module is presently being tested.

Techniques were developed to directly measure the transport properties of single Y-123 filaments. The resistive transition show that the quality of the 100-micron filaments is equivalent to the best polycrystalline Y-123. Filaments have been produced with self-field critical currents up to 2600 $A/cm^2$, with typical performance around 1500 $A/cm^2$, both bare and metal clad specimen. These filaments, like all bulk Y-123, are weak-linked, so the $J_c$ drops to around 10 $A/cm^2$ at 800 G.

Preliminary data on the mechanical properties of sintered Y-123 filaments indicate a fracture strength of 75-180 MPa. This data has been used to predict that long coils, with a 10-cm radius of curvature, can be wound from Ag/Pd clad 100 micron diameter filaments.

SECTION 3

HIGH TEMPERATURE SUPERCONDUCTOR

MOTOR DESIGN AND FABRICATION

ALAN CRAPO AND JERRY LLOYD

EMERSON MOTOR COMPANY


MOHAMED HILAL

UNIVERSITY OF WISCONSIN

## 3.1     Introduction

The Emerson Motor Division (EMD) of Emerson Electric Company is responsible for the design, construction, and testing of HTSC motors, and related engineering activities in the application of superconducting wire to motor technology.  In designing and building HTSC motors, there are two major objectives.  The first is to develop a motor or motors which will test the HTSC wire produced by Ceramic Process Systems (CPS) to verify that the wire meets its performance goals in a real motor.  The second major objective is to design and build a motor or motors that are optimized to take advantage of the characteristics of the newly developed HTSC wire.

While CPS is working toward short term and long term goals of wire performance, EMD is working on motor designs based on the near term and long term wire performance goals.  The long term goal for wire is a critical current density of 100,000 A/cm$^2$ in a field of three Tesla with a bending radius of one cm.  Long term, high performance motor designs are based on this

wire goal. In this report, DC homopolar or acyclic motors and DC heteropolar motors are evaluated.

The short term goal for superconducting wire is a critical current density of 1000 A/cm$^2$ in a field of 100 Gauss or 0.01 Tesla with a bending radius of 10 cm. Current motor designs of homopolar and induction motors that could be used as test bed motors to evaluate wire, are based on these near term wire goals. A homopolar motor design and an induction motor design are discussed in this report as proof of principle motors.

The work Dr. Mohamed Hilal has done on the eddy current and hysteresis components of AC losses and the conductor stability of multifilamentary ribbon conductors are analyzed and presented.

Since the ceramic fibers in HTSC wire are fragile, stress on the wire during the winding process is a great concern. Discussions of the relative merits of the most common winding methods are reported.

## 3.2    Application Study

In the past two decades, there have been many magnets, motors, and generators that have been built using NbTi superconducting wire at liquid helium temperature (4.2°K). Most of these magnets, motors, and generators have been smaller, lighter, and more efficient than their room temperature copper counterparts. These smaller and lighter devices have been made possible with NbTi's high critical current density in a high magnetic field. Current densities of 300,000 A./cm$^2$ and fields of 6 Tesla are common. High current densities and flux densities allow these motors and generators to be made with non-magnetic or "air" flux paths, making them small and light.

Our long term goal for HTSC wire is 100,000 A./cm² in a 3 Tesla field. When this high performance wire becomes available, high performance HTSC motors can be built. Initial application studies of high performance HTSC motors were done on a homopolar motor and a DC heteropolar motor. HTSC field windings were considered for each.

### 3.2.1 Homopolar Motor

The homopolar motor is the only electric motor without time varying magnetic fields. This "true DC" machine, first built by Michael Faraday in 1831, in its simplest disc form consists of a disc of electrically conducting material in a magnetic field parallel to the axis of rotation (figure 3.2.1.1). Torque is produced by current in the radial direction within the disc as shown in figure 3.2.1.2 and can be calculated per Fleming's rule.

$$T = B \times I \cdot (r_2 - r_1) \cdot (r_2 + r_1)/2 - \text{friction}$$

Where: T is the torque

B is the flux density

I is the current in the disc

$r_1$ is the radius of the inner current collector

$r_2$ is the radius of the outer current collector

$(r_2 - r_1)$ is the conductor length

$(r_2 + r_1)/2$ is the effective mean disc radius

The back EMF is determined by the flux between current collectors and the speed.

$$V_{Back\ EMF} = N \, d\phi/dt$$

Where N = 1 turn for a single disc motor

$$V_{Back\ EMF} = \phi \cdot RPM/60$$
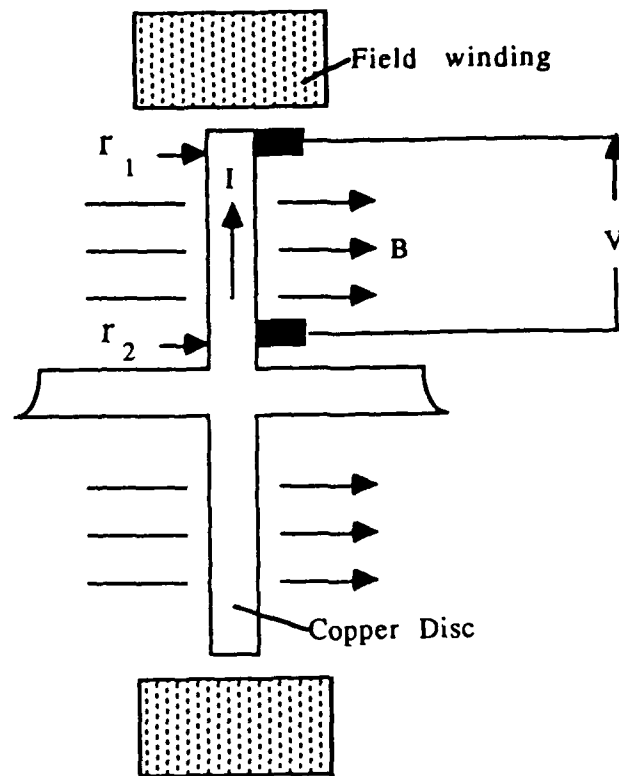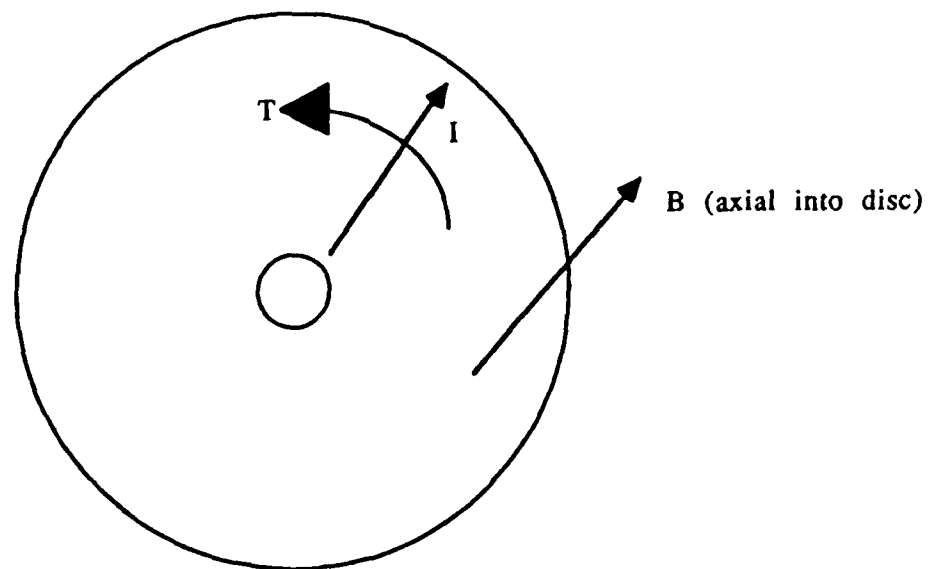
Figure 3.2.1.1     Side view of homopolar disc motor.



Figure 3.2.1.2     Axial view of disc.

$V_{Back\ EMF} = B \cdot \pi (r_2^2 - r_1^2) \cdot RPM/60$

Motor terminal voltage $= V_{Back\ EMF} - IR$ drop

The design goal for this potential HTSC motor application is as follows:

$B = 3$ Tesla (DC Field)

$J_c = 10^5$ A/cm$^2$

Output $= 50$ Hp @ 2000 RPM

The three Tesla DC field is to be produced by a superconducting field coil wound by HTSC wire.

For the sake of simplicity on the first level of design, the following assumptions have been made:

a. no friction,

b. no copper loss and no voltage drops in the current collectors,

c. The inner current collector radius $(r_1)$ is ten percent of the o...er current collector radius $(r_2)$.

The torque to produce 50 horsepower at 2000 RPM is 178.1 N.m. From the torque equation, the required current is a function of the rotor radius.

178.1 N·m $= 3$ Tesla x $I \cdot (r_2 - .1r_2) \cdot (r_2 + .1r_2)/2$

or $I = 119.9/r_2^2$

From the voltage equation, the back EMF is a function of the rotor radius.

$V = 3$ Tesla $\cdot \pi \cdot (r_2^2 - (.1r_2)^2) \cdot RPM/60$

or $V = 311r_2^2$

The current and voltage are plotted versus rotor radius in figures 3.2.1.3 and 3.2.1.4.

# 1 DISC HOMOPOLAR MOTOR VOLTAGE
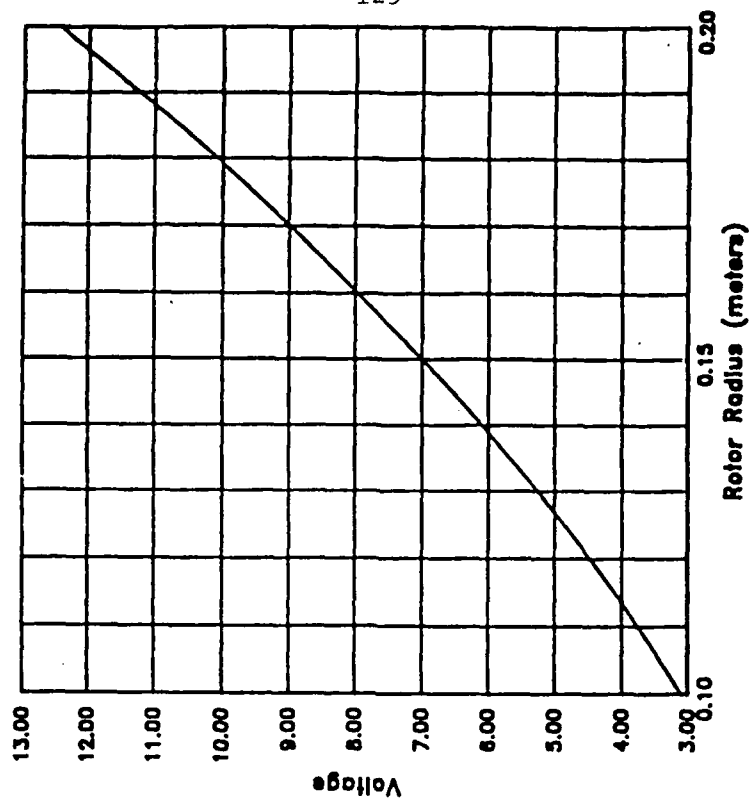
## (50 Horsepower at 2000 RPM)

Figure 3.2.1.4  Voltage vs Rotor Radius

# 1 DISC HOMOPOLAR MOTOR CURRENT

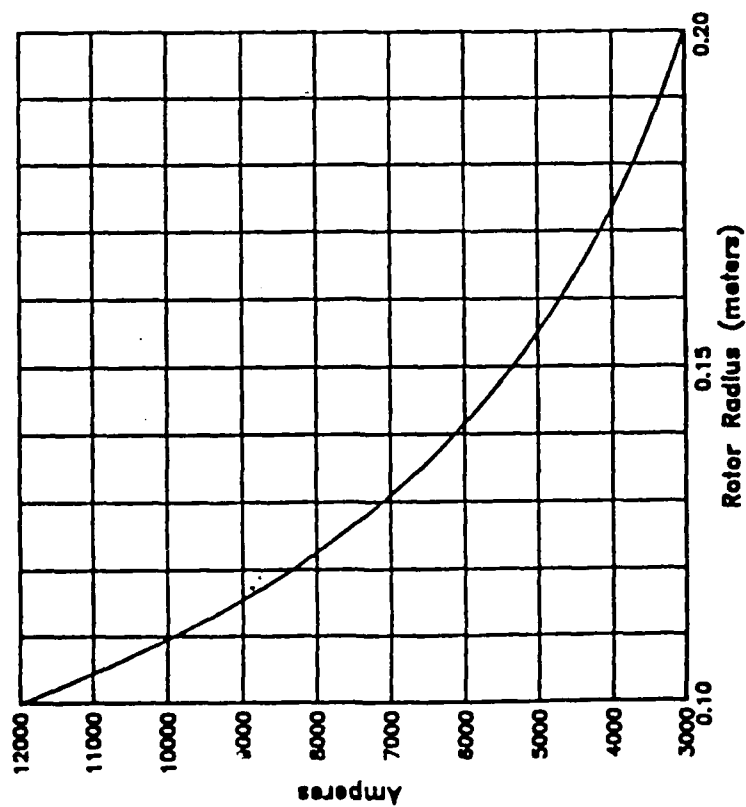## (50 Horsepower at 2000 RPM)

Figure 3.2.1.3  Current vs Rotor Radius

A 5 Volt, 7460 Ampere motor would have a single disc diameter of 0.254 meter or 10 inches. If multiple discs were in series, or multiple turns on a drum type motor, the rotor diameter would be about half of the above motor. The smaller version at a rotor diameter of 0.127 meter or 5 inches is smaller than a conventional 50 horsepower, 2000 RPM motor.

### 3.2.2 DC Heteropolar Motors

A high performance HTSC DC heteropolar motor would be designed with an operating flux density of 3 Tesla at the armature windings. The conventional DC machine would operate with a flux density of 0.75 Tesla in the air gap. Four times higher flux density greatly increases the power to size ratio of the armature. This allows the volume of the armature diameter to be reduced to one fourth of the original.

For initial consideration, we have referenced a conventional 50 horsepower 1750 RPM DC brush type motor. The standard motor has the following basic characteristics.

> Rotor Diameter = .194m (7.625 inches)
>
> Active Length = .241m (9.5 inches)
>
> Outside Diameter = .406m (16 inches)
>
> Rated Voltage and Current:
>
> > Armature: ·500 Volts and 83 Amperes
> >
> > Field: 300 Volts and 2.25 Amperes

For the superconducting field version of this motor, we reduce the armature diameter to 0.123 meters (4.8 inches) and the length is reduced to 0.152 meters (6.0 inches). The iron is replaced with a light weight non-magnetic material.

The field coil design and analysis was done using a finite element model. A plot of the flux lines for 1/4 of a machine is shown in figure 3.3.2.1. The field coil of 300,000 Amperes turns per pole produces a radial flux density of over three Tesla on the surface of the armature. The peak flux density in the superconducting field winding is 5 Tesla.

This motor would be lighter than the conventional motor because most of the steel would be replaced by a lightweight non-magnetic material. The only steel required would be a shell which acts -- a flux shield. The outside diameter of the flux shield would need to be about the same diameter as the conventional DC motor in order to contain the flux. The major improvement would be a lighter weight motor with 8 to 10 times lower armature inertia.

The field winding would have 300,000 Ampere turns. This would probably be 2 to 3 Amperes and 100,000 to 150,000 turns of superconducting wire 0.05 mm (0.002 inch) diameter.

3.3     Near Term Proof of Principle Motors

Two near term proof of principle motors will be built to evaluate HTSC wire as it becomes available from CPS. The first motor will be an iron core homopolar motor with HTSC field coils. The second motor, to come later, will be a three phase AC induction motor with HTSC stator windings. The low critical current density and low magnetic field for the HTSC wire operating conditions, require that any near term HTSC motors have steel flux paths if much torque is to be produced. The two motors considered, both have steel magnetic circuits.
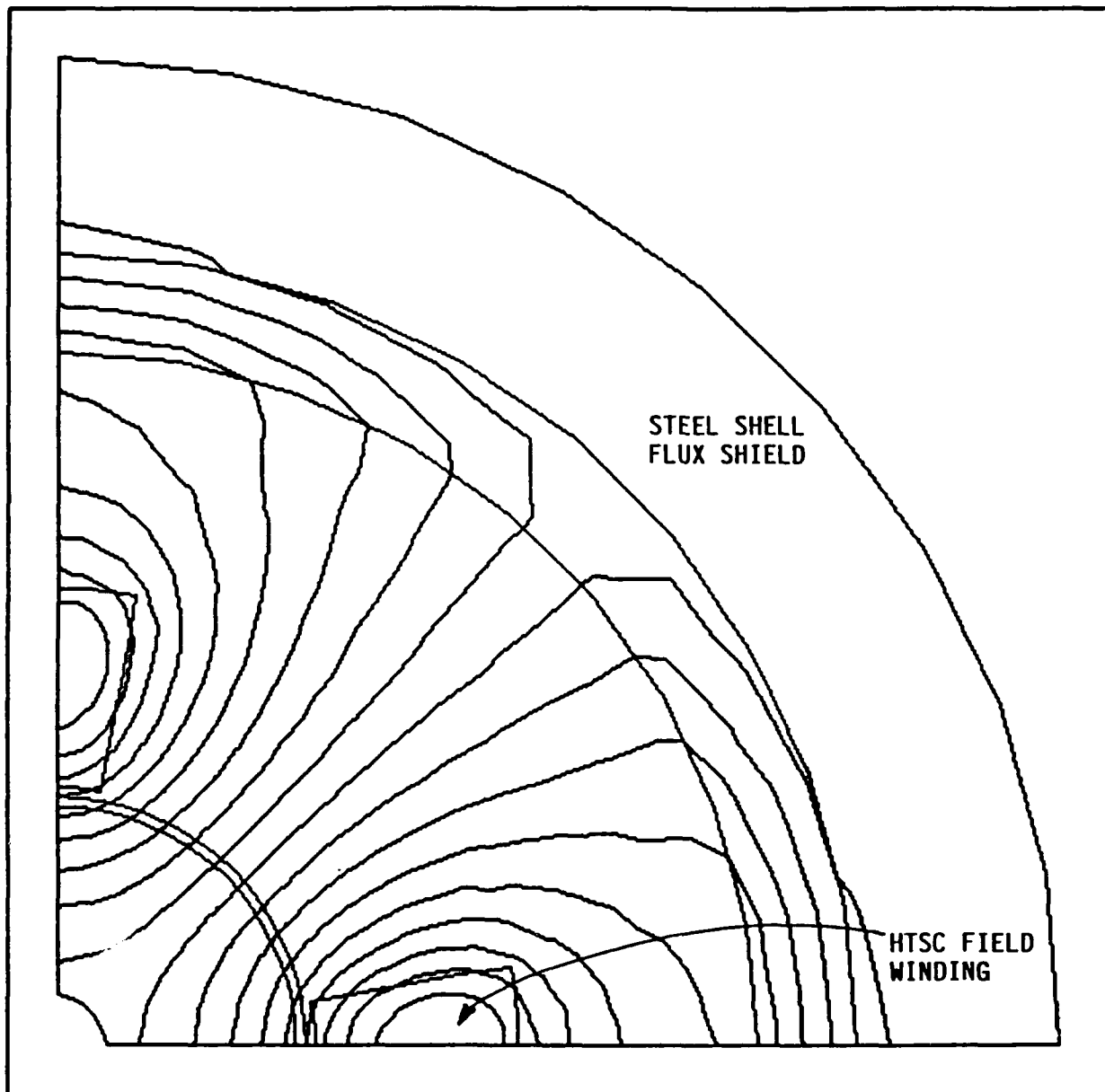
FIGURE 3.2.2.1  FLUX PLOT OF SUPERCONDUCTING FIELD FOR DC HETEROPOLAR MOTOR.

### 3.3.1  Iron Core Homopolar Motor

The near term goals for HTSC wire performance sets several constraints on the design of a homopolar motor.  The minimum bending radius, maximum current density and maximum magnetic field force a design which has a low power rating for its size.  Since the main purpose of the first motor is to test HTSC wire, a high power output motor is not necessary.

The following constraints are imposed on the design by the wire:

1.  The bending radius on the HTSC field coil must be greater than 10 cm.

2.  The magnetic flux density on the HTSC wire is to be less than 100 Gauss.

3.  The current density in the superconducting core of the HTSC wire should be 1000 amperes/cm$^2$.

4.  In order to meet two and three above and have as much flux as possible to produce torque, the flux path needs to be made of high permeability steel with as small an air gap as possible.

5.  To best meet four above, the current path in the rotor or armature should be in the steel that also carries the flux.

Figure 3.3.1.1 shows the cross sections of a homopolar motor with steel flux paths and steel current path in the rotor.  Figure 3.3.1.2 shows a plot of the flux in the motor from a finite element model with the flux density in the air gap of 0.77 Tesla.

The back EMF and the torque constant are both proportional to the flux produced by the HTSC field winding.

$$VBack\ EMF = \phi \cdot RPM/60$$

BRUSHES

SLIP RINGS

BRUSH
HOLDER

STEEL
RETURN
PATH

STEEL
ROTOR

HTSC
COILS
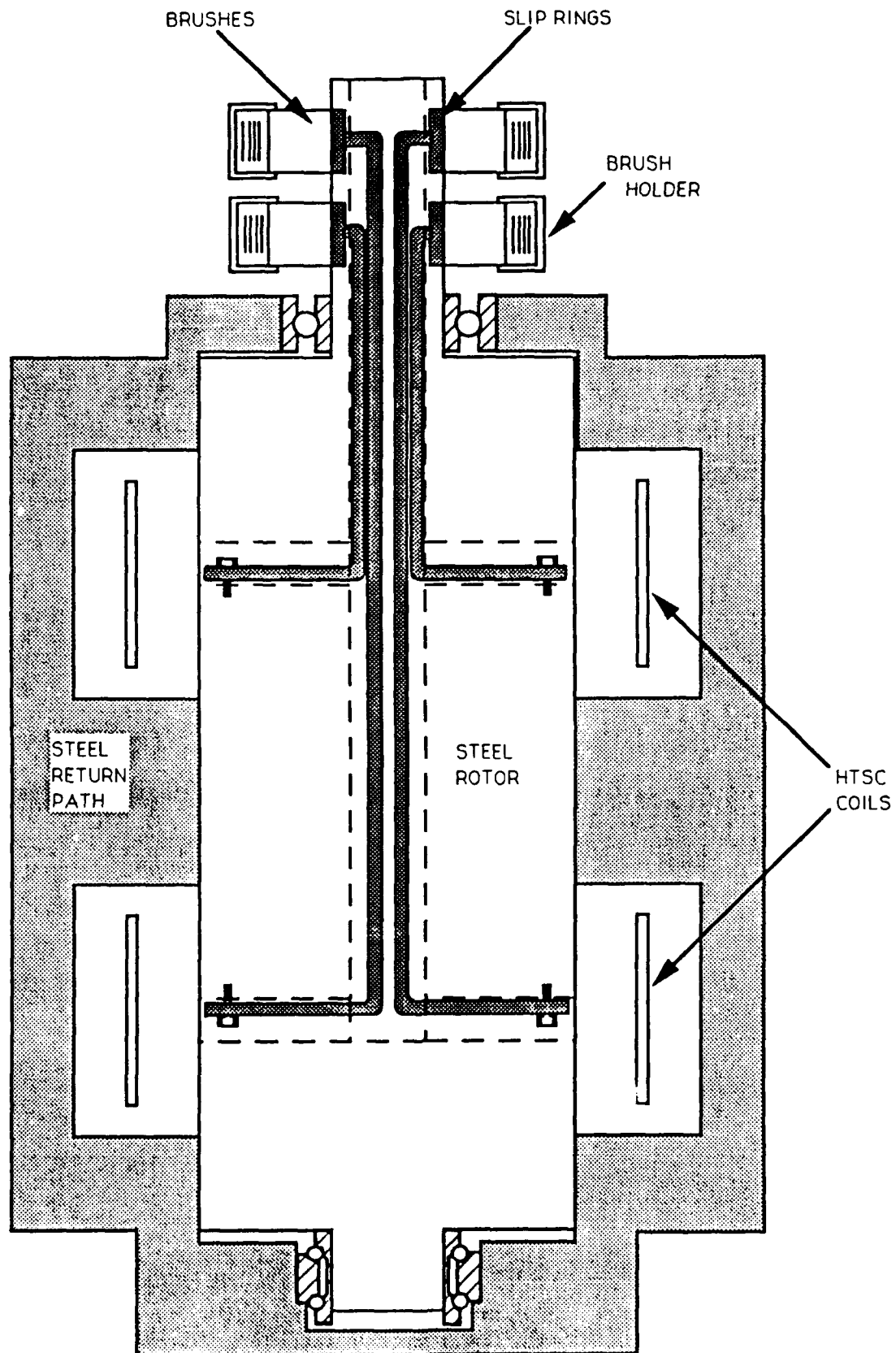
FIGURE 3.3.1.1  STEEL ARMATURE HOMOPOLAR MOTOR WITH HTSC FIELD WINDINGS

$$\text{Torque} = B_{radial} \cdot I_{axial} \cdot \text{effective radius} \cdot \text{effective}$$

path length of current in field.

The flux produced by the ampere turns of the field winding is limited by the steel saturation. The ampere turns the HTSC coil can support is limited by the critical current density and the magnetic field at the coil. The above design produces about 100 Gauss at the coil for a current density of 1000 A./cm$^2$. Lower current densities will produce a lower field at the coil. The armature voltage controls the speed of the motor and the current controls the torque. Figure 3.3.1.3 shows the horsepower output versus current density in the superconducting field winding for various armature currents at 1000 RPM. Figures 3.3.1.4 and 3.3.1.5 show the same curves for 2000 RPM and 3000 RPM.

The brushes for the proposed current collection system would be made of metal graphite sliding on slip rings. The current path from the shaft mounted slip rings to the torque producing part of the rotor is through the hollow shaft and out through radial ducts.

The windings would be cooled by submerging the entire motor in a tank of liquid nitrogen. Nitrogen flow over the coils will insure that the HTSC wire remains below the critical temperature Tc.

The bearing system to operate in liquid nitrogen will not be elaborate. The bearings will be standard ball bearings that have been cleaned so that there is no grease left. Liquid nitrogen will then act as the lubricant. The bearings will have a short life of possibly only 1000 hours. Since the main purpose of this motor is to test wire, the short life should not be a problem. Bearings can be made to have a long life in liquid nitrogen, but that is beyond the scope of this program.
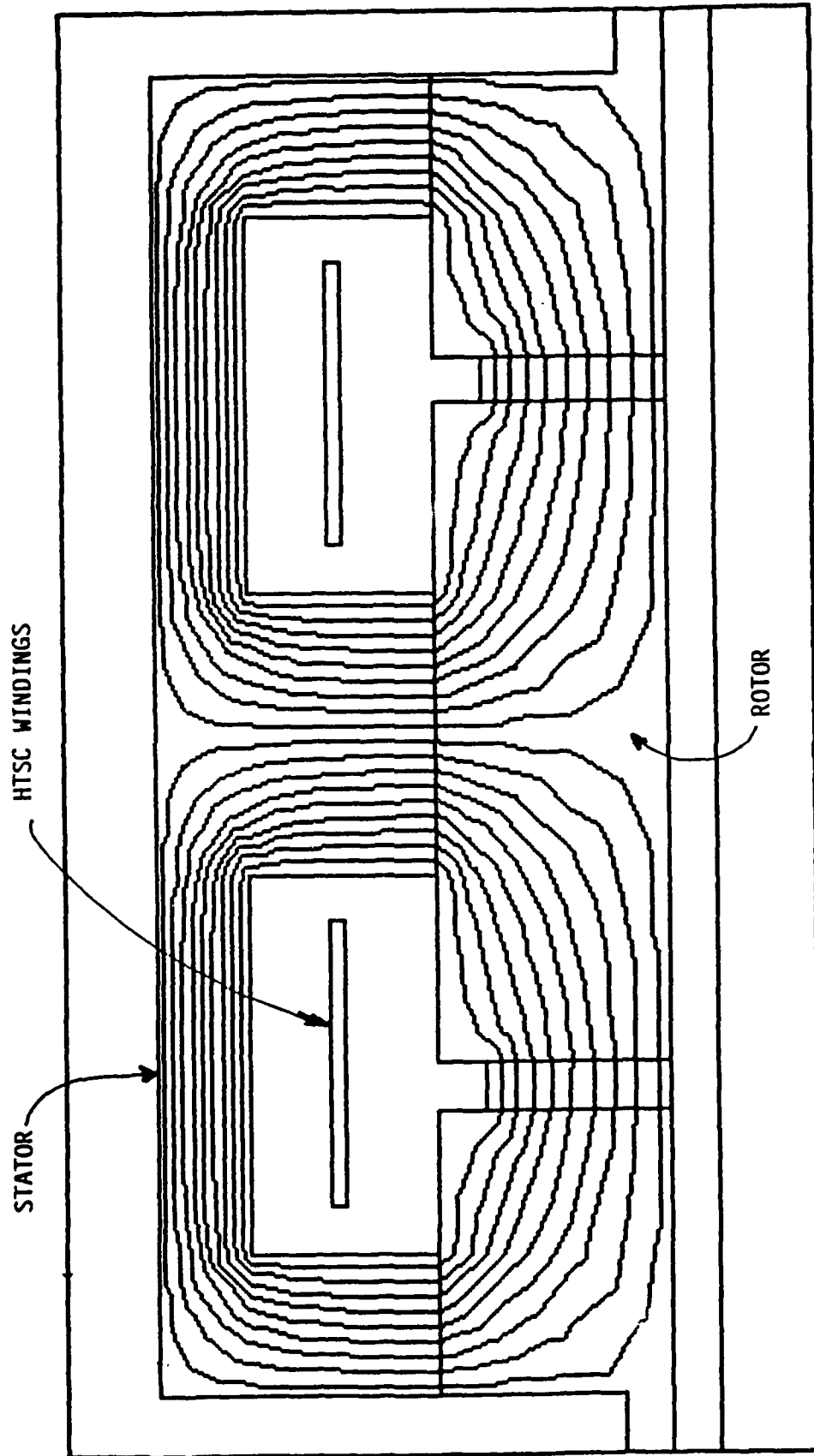
FIGURE 3.3.1.2  FLUX PLOT OF IRON CORE HOMOPOLAR MOTOR WITH STSC FIELD WINDINGS.

# 1000 RPM
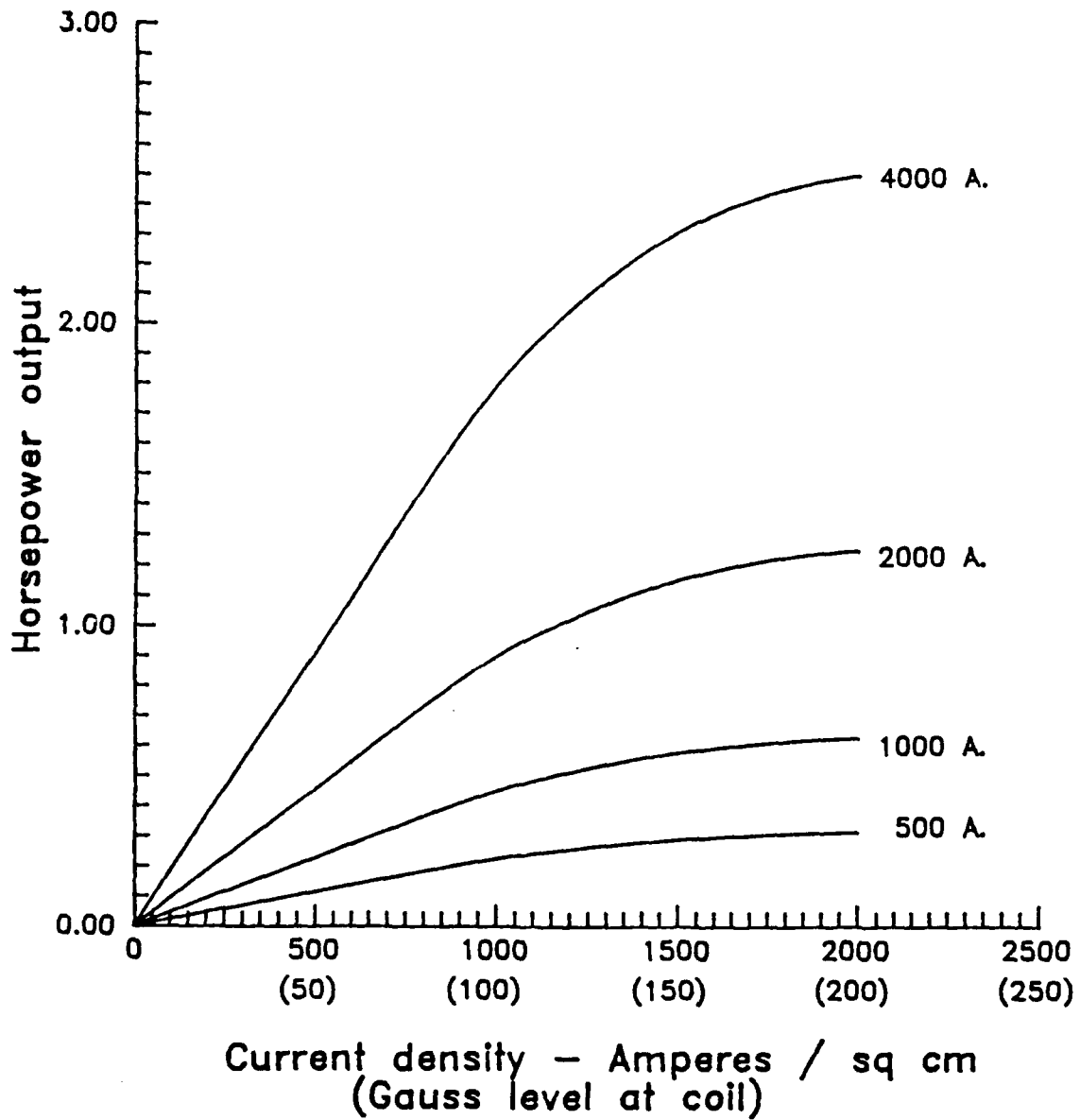


Figure 3.3.1.3   Horsepower output versus current density in the superconducting field conductor for various armature currents at 1000 RPM

## 2000 RPM
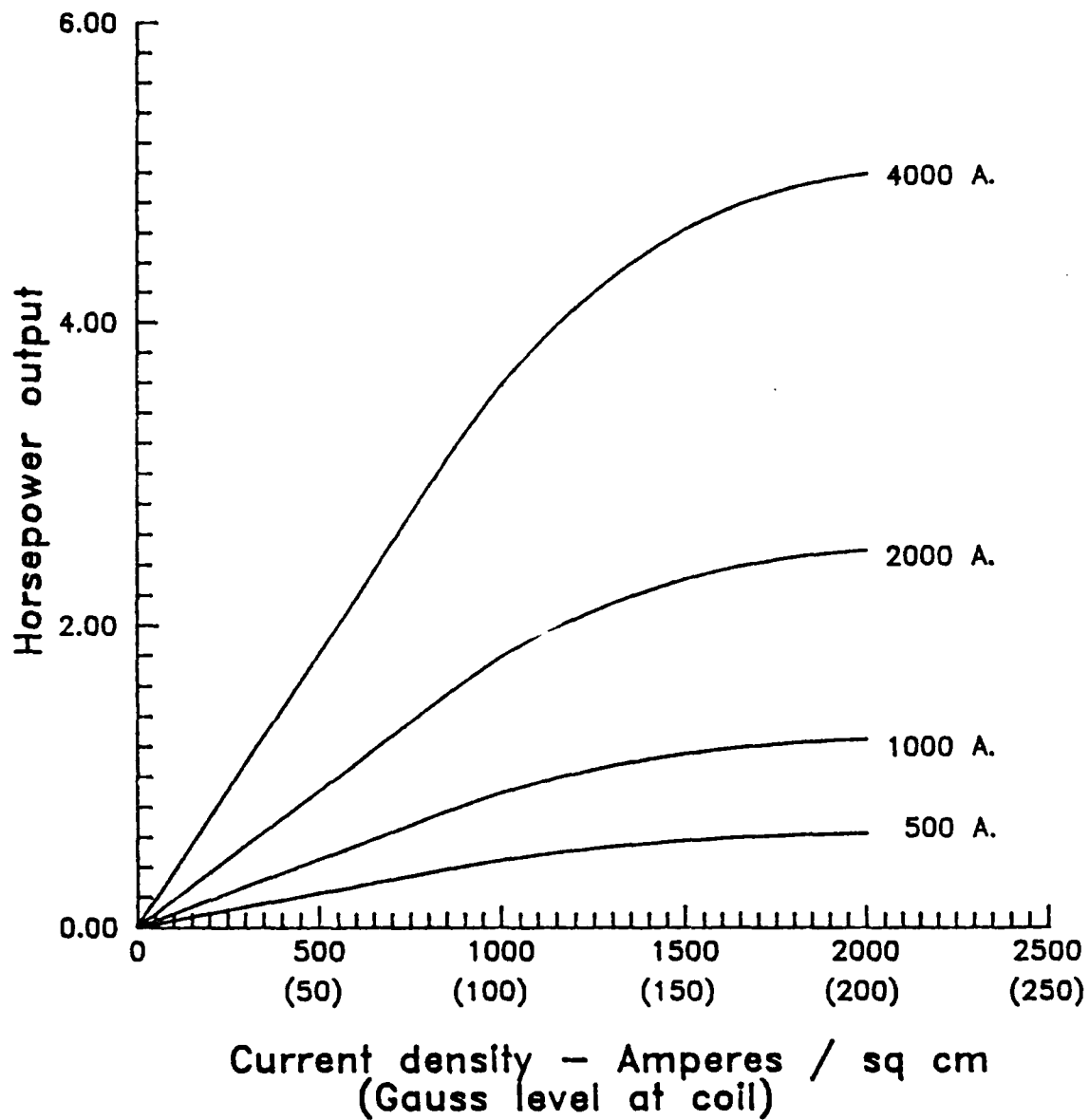


Figure 3.3.1.4 Horsepower output versus current density in the superconducting field conductor for various armature currents at 2000 RPM

## 3000 RPM
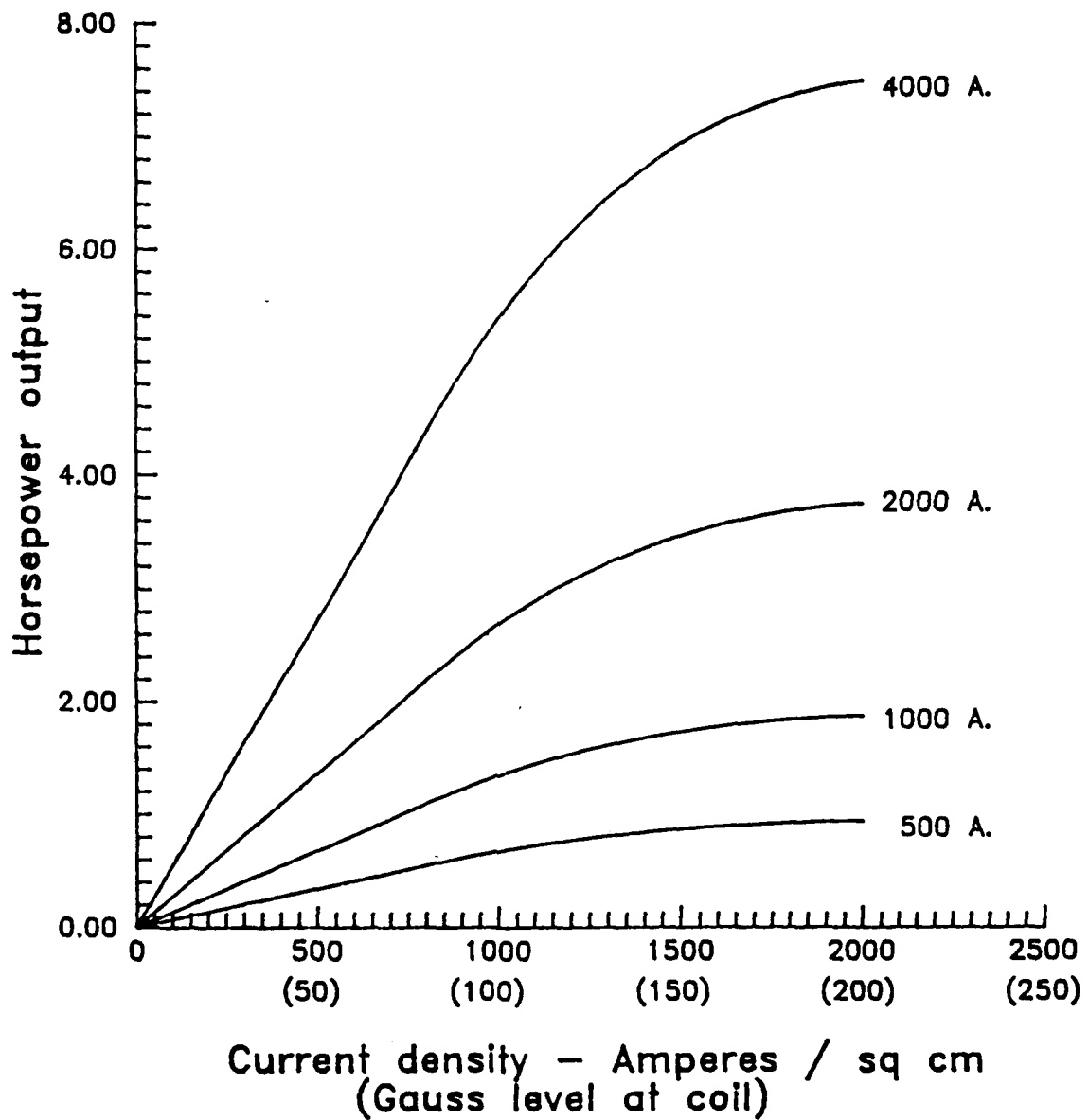


Figure 3.3.1.5   Horsepower output versus current density in the superconducting field conductor for various armature currents at 3000 RPM

### 3.3.2 HTSC Induction Motor

The second proof of principle motor will be an induction motor with HTSC wire in the stator. This motor would also operate submerged in liquid nitrogen. Other than the careful handling of the HTSC wire, the induction motor is not a difficult motor for Emerson to build. We already make rotors and stators for conventional cryogenic induction motors designed to run in liquid nitrogen at U.S. Electrical Motors.

U.S. Electrical Motors (USEM) is a division of Emerson Motor Company that makes medium and large sized induction motors. One of USEM's products is a line of motors marketed under the genetic heading of "Cryogenics". These motors are designed to operate submerged in a liquified gas with the gas flowing over, around, and through the winding. The extreme cold and thermal transfer properties of these liquified gases are used to minimize temperature rise in both the stator and rotor; thus allowing a design which approaches the theoretical maximum H.P. limits for a given frame size and stack length.

The term "cryogenic" normally is used to designate an operating temperature of -160° centigrade or colder. In practice, USEM uses the term to refer to any motor, totally submerged in any liquid gas, which uses that gas as a primary cooling medium. We have designed and manufactured motors for fluids as warm as JP-4 jet fuel at +27°C and as cold as liquid neon at -246°C.

While the basic electrical design concepts are the same on cryogenic motors as on air motors, some specific items are unique. One of the major differences is the special care given to the insulation for cryogenic applications. With thermal cycling between room temperature and cryogenic temperatures, there is a great deal of expansion and contraction. The

windings are protected from abrasion and also given extra strength to maintain integrity over a long life.

The standard copper windings carry a current density of 1200 to 1500 A/cm$^2$ at 77°K. With HTSC windings, the current density would be a little less with wire available this year but the resistance would be essentially zero.

The wire parameter that has the main impact on the size of the motor is the bending radius. With a bending radius of 6 cm, a 180 frame with a stator outside diameter of 19 cm and a rotor diameter of 12 cm is the smallest standard induction motor size that can be built without over-bending the wire.

Depending on the axial length, this 180 frame HTSC induction motor should produce two to five horsepower at 1795 RPM with 480 volts three phase AC. The three horsepower version would have a current of 3.8 amperes.

## 3.4 AC Losses

While high temperature superconductors with practical current densities are under development, their characteristics must be investigated theoretically. At the University of Wisconsin, AC loss and stability models are being developed, taking into account the impact of the weak link characteristics of the material.

### 3.4.1 Eddy Current Losses in Twisted Multifilament Composite HTSC Conductors

All the newly discovered HTSC materials exhibit anisotropy in critical current density, having higher critical current density in two directions and lower current density in the third normal direction. This will have an impact on the nature and magnitude of the induced eddy currents.

### 3.4.1.1 Critical Twist Pitch

First we consider as an example the conductor design using a low temperature superconductor. It is necessary in this case to use a multifilamentary form to reduce flux jumps and obtain intrinsic stability. These filaments will be strongly coupled in a time varying field, which can result in excessive AC losses. To decrease coupling and reduce loss the filaments are twisted so that the critical current density is not exceeded anywhere along the superconductor filaments. The critical twist pitch is defined as the maximum twist pitch at which critical current density is not exceeded anywhere along the conductor.

In AC applications, it will also be necessary to have twisted HTSC multifilamentary conductors to interrupt filament decoupling and reduce eddy current losses. Our initial analysis shows that this will also be required to have intrinsically stable HTSC conductors.

To determine the critical twist pitch for HTSC conductors, we assume that the critical current density in the longitudinal direction, $J_{cl}$, is greater than the critical current density in the transverse direction, $J_{ct}$. Due to this anisotropy, three critical twist pitches can be defined which correspond to the following conditions:

1) Transverse critical twist pitch, $L_t$

The transverse critical twist pitch is reached when the current density in the transverse direction of the superconductor is equal to the transverse critical current density at a point along the twist pitch but the longitudinal current density anywhere along the filament is less than the longitudinal critical current density.

2) Longitudinal critical twist pitch, $L_c$

If $L_c$ is exceeded, the superconductor current is equal to the critical current at a point along the twist pitch, whereas the transverse current density is below $J_{ct}$.

3) The anisotropic critical twist pitch, $L_{ct}$

As the twist pitch $L_{ct}$ is reached, the superconductor current is equal to the critical current at a point along the twist pitch and the transverse current density exceeds $J_{ct}$ along part of the twist pitch.

The three critical twist pitches are functions of the time rate of change of the magnetic field, dB/dt, the transverse matrix effective resistivity, and the conductor geometry. For AC motor applications the values of $L_t$ and $L_c$ can be calculated from the data given in Table 3.4.1.1 to be 0.11 mm and 0.74 mm, respectively, for wire with a copper matrix. Using a 70Cu-30Ni alloy matrix increases these two twist pitches to 20 mm and 9.9 mm, for $L_t$ and $L_c$, respectively. A high resistivity matrix will increase both the transverse and longitudinal critical twist pitch.

The longitudinal and transverse critical twist pitch values are plotted against applied field of a 60 Hz AC field in Figure 3.4.1.1 for the case of $J_{ct}/J_c = 0.01$. The $L_{ct}/L_c$ ratio is plotted versus the dimensionless group G [where $G = (L_c/d)(J_{ct}/J_c)$] in Figure 3.4.1.2.

With these twist pitch values it is possible to calculate the eddy current losses in the superconductor and the stabilizer. It can be shown that power loss, P, can be expressed in the form: $P = [2(\delta B/\delta t)^2/\mu_o]\tau$ , where the time constant, $\tau$, incorporates the dependence upon the critical current densities, critical twist pitches, and the parameter G. The Third Quarterly Report presents expressions for the time constants appropriate for eddy currents in the

superconductor and the stabilizer. Figure 3.4.1.3 shows the total eddy current losses, stabilizer losses, and superconductor losses, as a function of the variable G. At small G, most loss occurs in the stabilizer, but superconductor losses become important at large G.

Table 3.4.1.1

Parameters for Calculation of Critical Twist Pitch

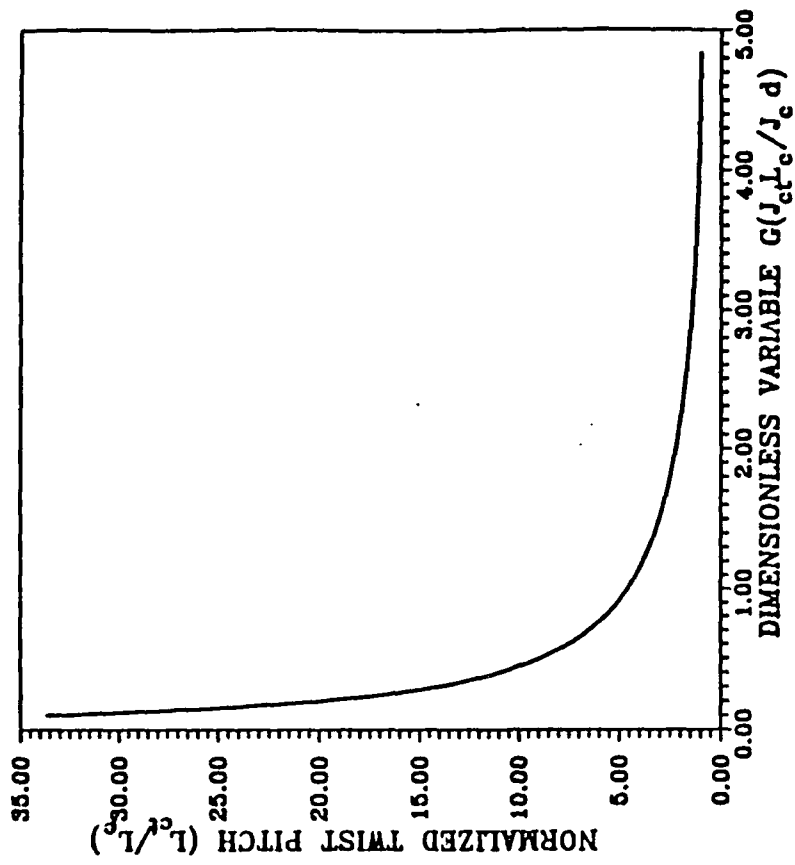|  | Copper | 70 Cu – 30 Ni |
|---|---|---|
| $\rho_e$, $\Omega$, m | ~ $2 \times 10^{-9}$ | $36 \times 10^{-8}$ |
| B, Tesla | 3 | 3 |
| frequency, $sec^{-1}$ | 60 | 60 |
| $J_c$, $A/m^2$ | $10^9$ | $10^9$ |
| d, m | $10^{-5}$ | $10^{-5}$ |
| $J_{ct}$, $A/m^2$ | $10^7$ | $10^7$ |
| $L_c$, m | $7.4 \times 10^{-4}$ | $9.93 \times 10^{-3}$ |
| $L_{ct}$, m | $1.1 \times 10^{-4}$ | $2 \times 10^{-2}$ |

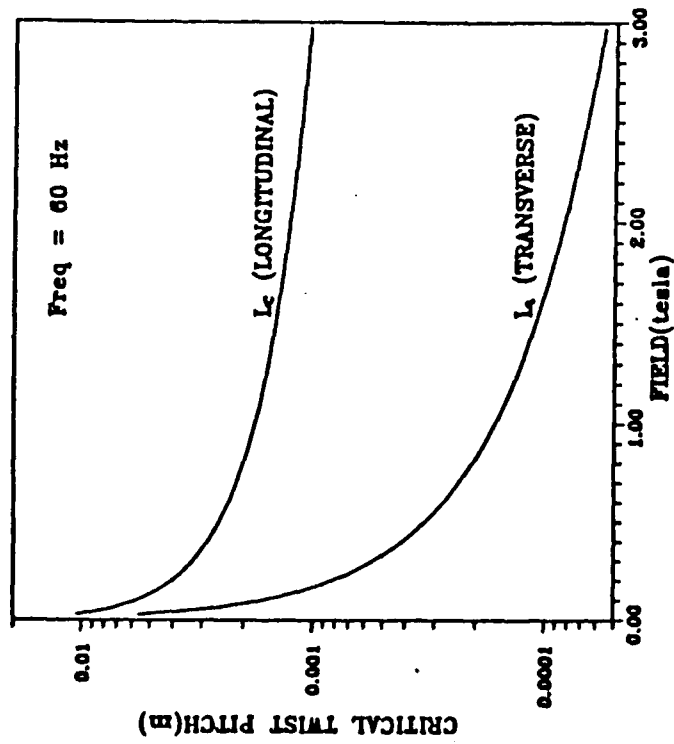Figure 3.4.1.2   Twist Pitch versus G
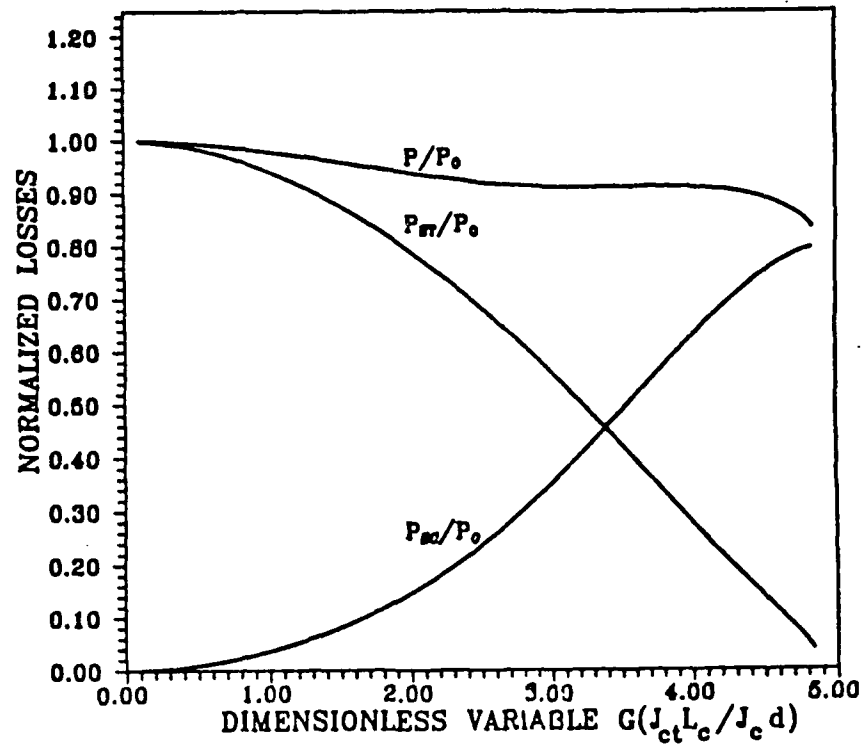


Figure 3.4.1.1 Field Dependence at 60 Hz

Figure 3.4.1.3    Normalized Total, Stabilizer, and Superconductor Losses versus G

3...2    Hysteresis Losses in High Temperature Superconductors

The critical state model has been extensively used to characterize the magnetization behavior of low temperature superconductors and is used here to describe the magnetization characteristics of HTSC.

### 3.4.2.1 HTSC Magnetization Model

Whereas the magnetization and transport critical current density of low temperature superconductors are the same, they can differ by orders of magnitude for high temperature superconductors. The transport critical current density $J_c$ of HTSC is significantly less than the magnetization critical current density, $J_M$, due to the presence of weak links between grains.

Due to the difference between $J_M$ and $J_c$ the model developed to describe LTSC magnetization cannot be used for high temperature superconductors. We have developed a magnetization model for HTSC which takes into account the presence of minor current loops which exist within the individual grains and the presence of major current loops due to the transport current flowing across the grains. The HTSC magnetization is determined as a function of the two critical current densities $J_c$ and $J_M$. A slab geometry, figure 3.4.2.1, is considered in applying the model. The following distinct regimes are considered as the field increases:

a.    Full grain penetration

Figure 3.4.2.2 shows a part of the slab where the individual grains are fully penetrated. The magnetic field and the current density distribution across the individual grains are shown in the same figure.

b.    Partial grain penetration but full field penetration

Figure 3.4.2.3 shows that the grain is partially penetrated by the field. The magnetic field, however, penetrates the sample inducing magnetization current in a number of grains. The sample is thus fully penetrated by field.
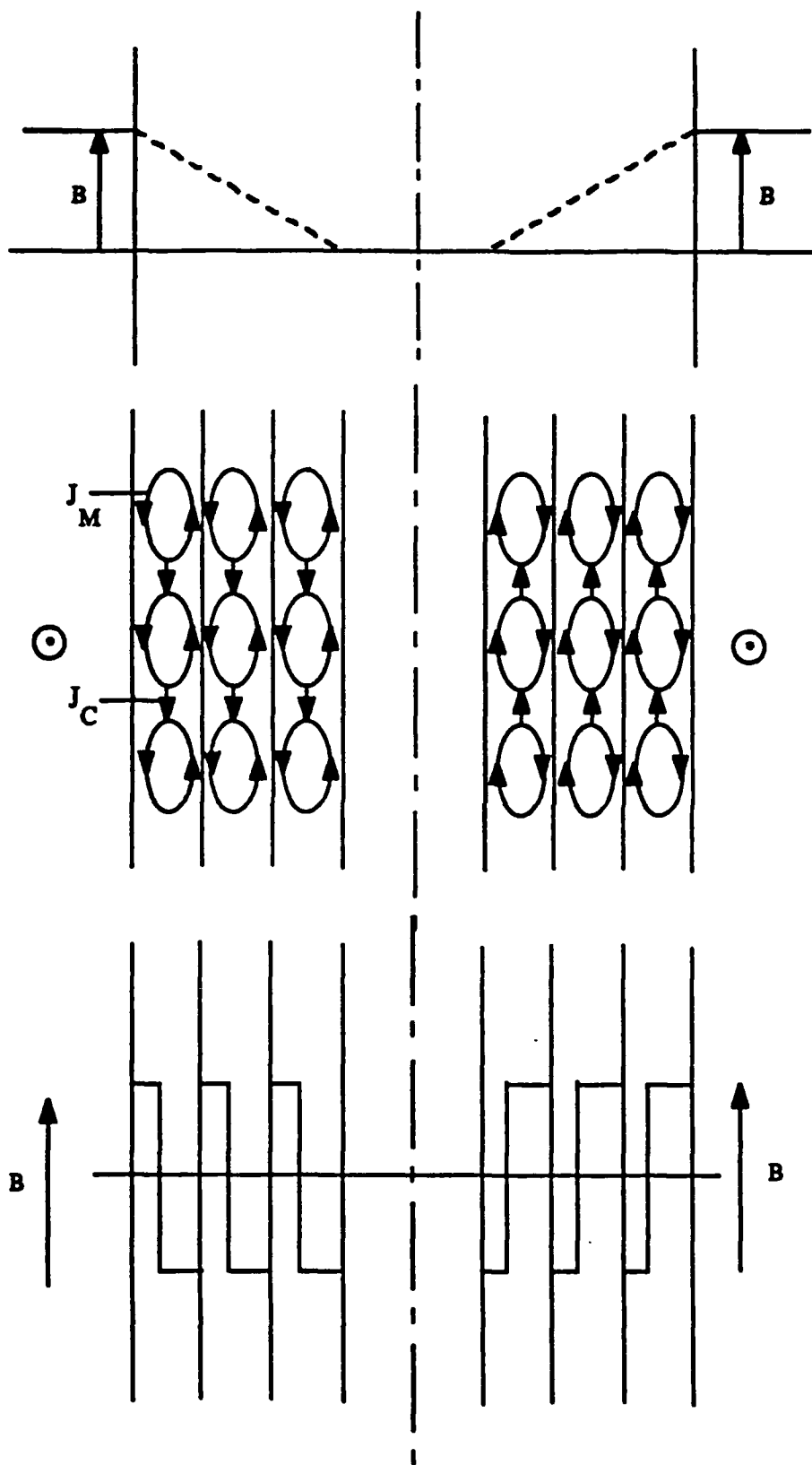
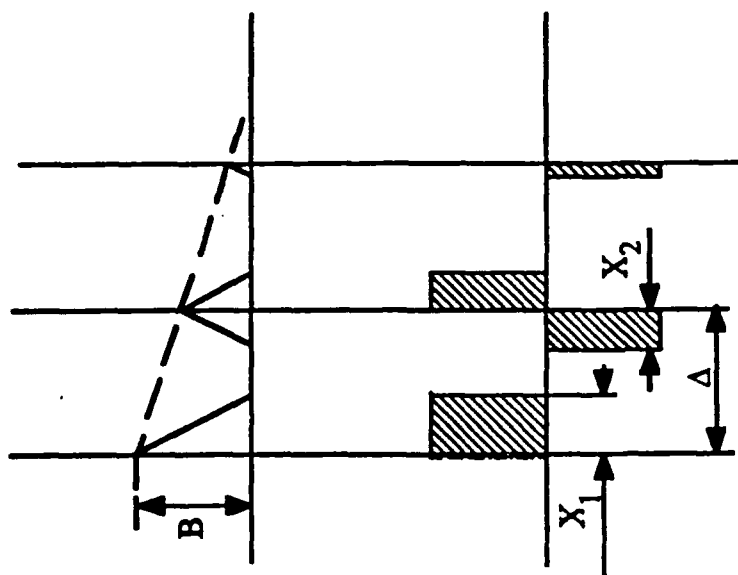**FIGURE 3.4.2.1.   MINOR AND MAJOR CURRENT LOOPS IN HTSC**

FIGURE 3.4.2.3.    GRAINS ARE PARTIALLY PENETRATED,
BUT FULL FIELD PENETRATION

FIGURE 3.4.2.2.    GRAINS ARE FULLY PENETRATED AND
FIELD PENETRATION

c. Partial grain penetration and partial field penetration

This region represents the last grain penetrated by the field. It thus consists of one grain in each half of the slab.

### 3.4.2.2 HTSC Magnetization Analysis

The slab is divided to a large number of thin slabs representing the sample grains. The sample magnetization is determined as the magnetic field increases taking into consideration the three regions described above. The magnetization loops are calculated assuming different $J_c$, $J_M$ grain size and sample size.[1] We consider both the Bean model, where $J_c$ is assumed independent of field and the Kim- Anderson model, where $J_c$ is assumed to be inversely proportional to the field. Magnetization curves using Bean's model are shown here as an example. Actual curves will be produced when more data is available for the superconductor. Figure 3.4.2.4 shows magnetization loops for different size samples for the case when the magnetic $J_M$ is taken to be $10^5 A/cm^2$ and grain size is 10 microns. Figures 3.4.2.4 A-D show how the magnetization loops change as the $J_c$ increases to $10^3$, $10^4$, and $8 \times 10^4$ $A/cm^2$, respectively. The magnetization loop area is small for low $J_c$ (note the scale change in the Figure). Sample size has a major effect on loss, although the dependence on sample size is not simple. Figures 3.4.2.5 A-D is a similar series, showing the variation in magnetization loops with grain size for a constant sample size of $10^{-4}$ m. Grain size only has an important effect on loss for low critical current

---

[1]. The rather lengthy derivation of this model is presented in detail in the Third Quarterly Report
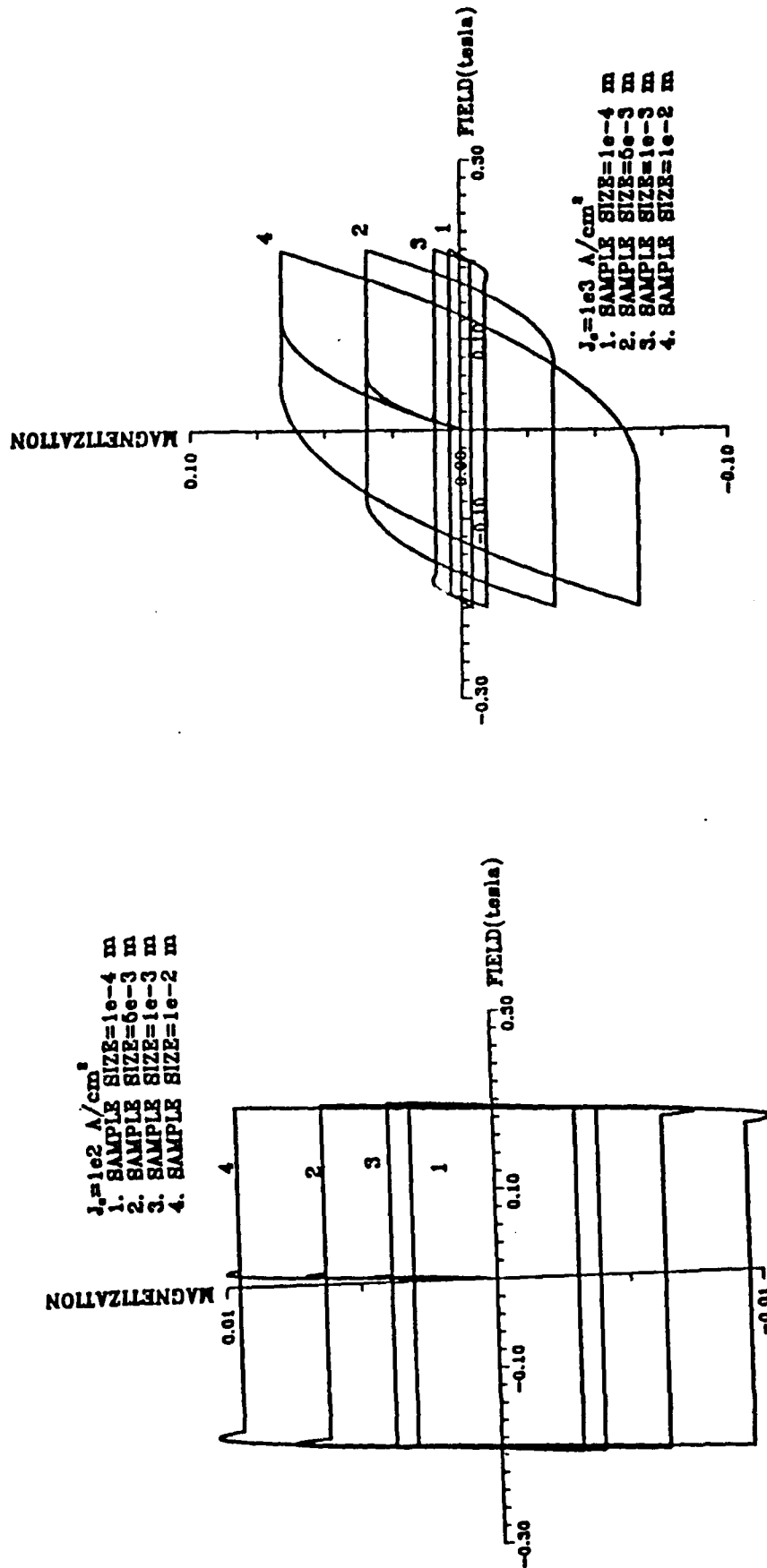
Figure 3.4.2.4    Magnetization Loops for HTSC Material with 10-Micron Grain Size, As a Function of Sample Size
A) $J_c$ – 100 A/cm² B) $J_c$ – 1000 A/cm²
C) $J_c$ – 10,000 A/cm² D) $J_c$ – 80,000 A/cm²

Figure 3.4.2.4   Magnetization Loops for HTSC Material with 10-
Micron Grain Size, As a Function of Sample Size
A) $J_c$ – 100 A/cm² B) $J_c$ – 1000 A/cm²
C) $J_c$ – 10,000 A/cm² D) $J_c$ – 80,000 A/cm²

Figure 3.4.2.5    Magnetization Loops for HTSC Material, Sample Size
                  $10^{-4}$ m, As a Function of Grain Size
                  A) $J_c$ = 100 A/cm$^2$    B) $J_c$ = 1000 A/cm$^2$
                  C) $J_c$ = 10,000 A/cm$^2$    D) $J_c$ = 80,000 A/cm$^2$
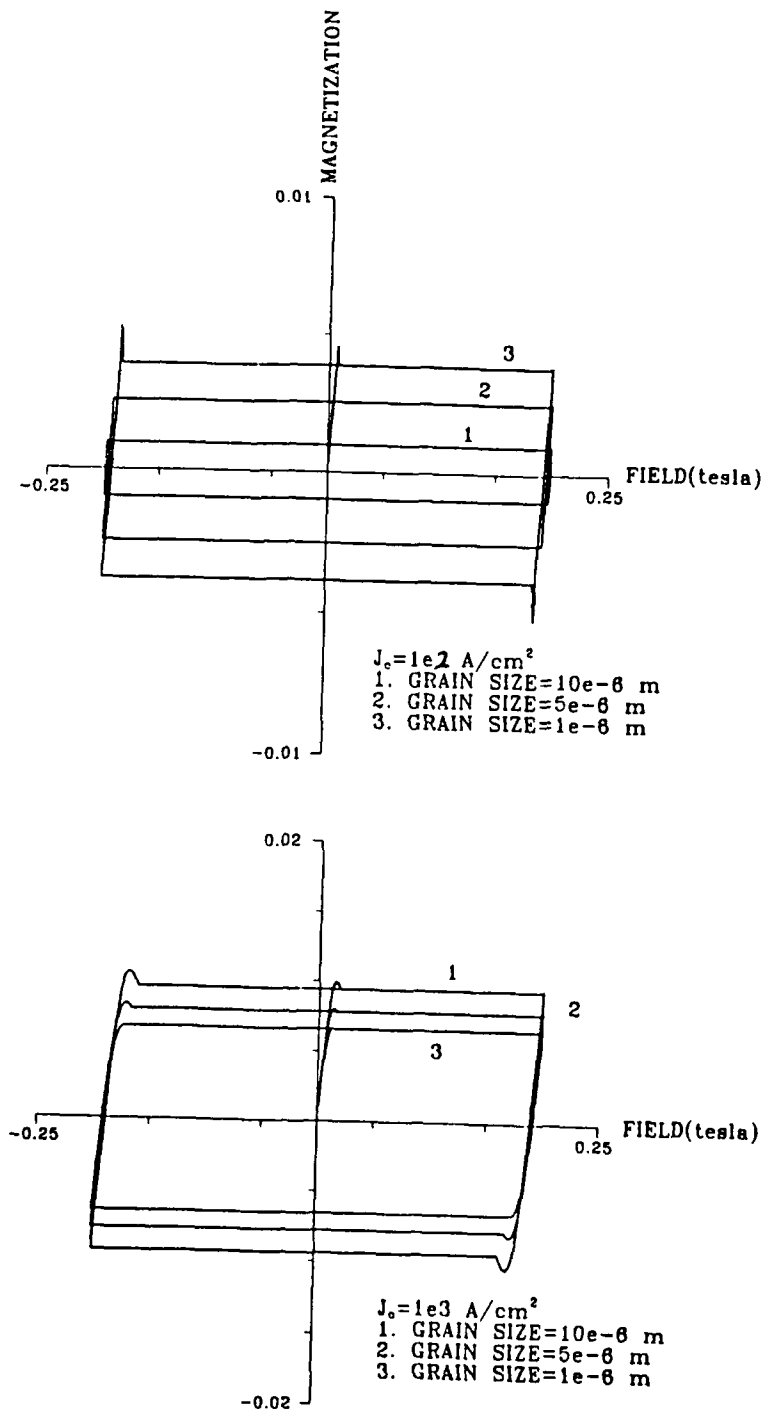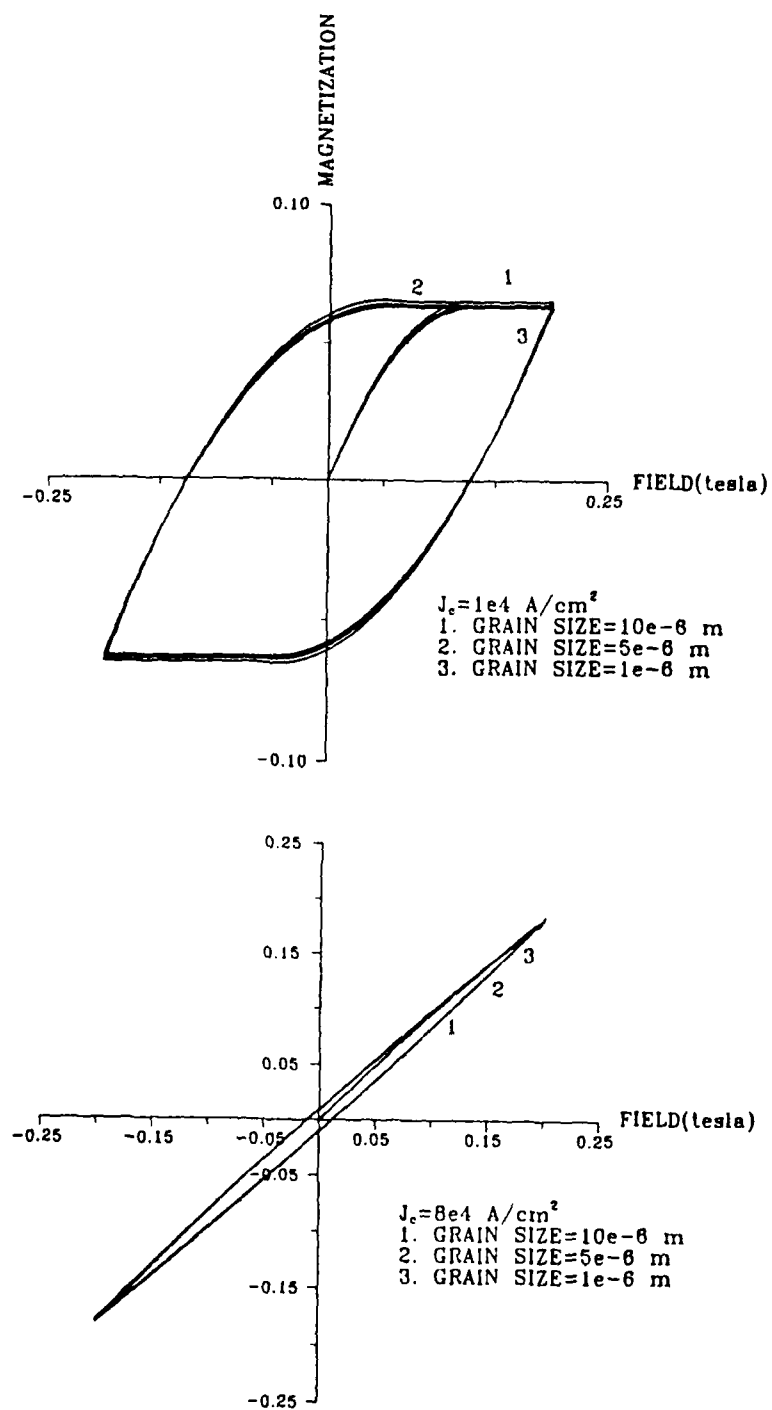
Figure 3.4.2.5    Magnetization Loops for HTSC Material, Sample Size
                  $10^{-4}$ m, As a Function of Grain Size
                  A) $J_c$ – 100 A/cm$^2$    B) $J_c$ – 1000 A/cm$^2$
                  C) $J_c$ – 10,000 A/cm$^2$    D) $J_c$ – 80,000 A/cm$^2$

cases. Finally, the influence of transport current density $J_c$ is shown in Figure 3.4.2.6 for a $10^{-4}$ m sample with 10 micron grain size. Loop area, and hence loss, increases gradually with $J_c$ up to 5000 A/cm$^2$ in the full field penetration/partial grain penetration regime. At 10,000 A/cm$^2$ the loop abruptly collapses, as the system transitions from full field penetration to partial field penetration. Loss again increases wi... $J_c$ at 80,000 A/cm$^2$, as magnetization increases, approaching full field/full grain penetration.

## 3.5 Conductor Stability

The proposed ribbon conductor consists of multiple silver coated filaments soldered to copper foils. We consider the case where there is no twisting or transposing of the strands. In an effort to optimize design, the adiabatic and dynamic stability of the ribbon are evaluated.

## 3.5.1 Conductor Adiabatic Stability

Flux jumps, a source of intrinsic instability, may occur in low temperature superconductors and have been extensively investigated. The low temperature composite conductors are designed to prevent flux jumping from taking place. We assume that flux jumping is also a source of instability for high temperature superconductors and should be prevented. The critical-state model, which is found to be applicable for low temperature superconductors, is used for HTSC stability analysis.

The superconductor critical state may become unstable due to the interaction between two inherent properties of superconductors:

(a) Flux lines pinning forces decrease as the superconductor temperature increases which results in lower critical current densities;

(b) Flux motion within the superconductor generates heat.

Flux jumping and adiabatic stability are two consequences of the above superconductor characteristics which are assumed to be applicable for HTSC.
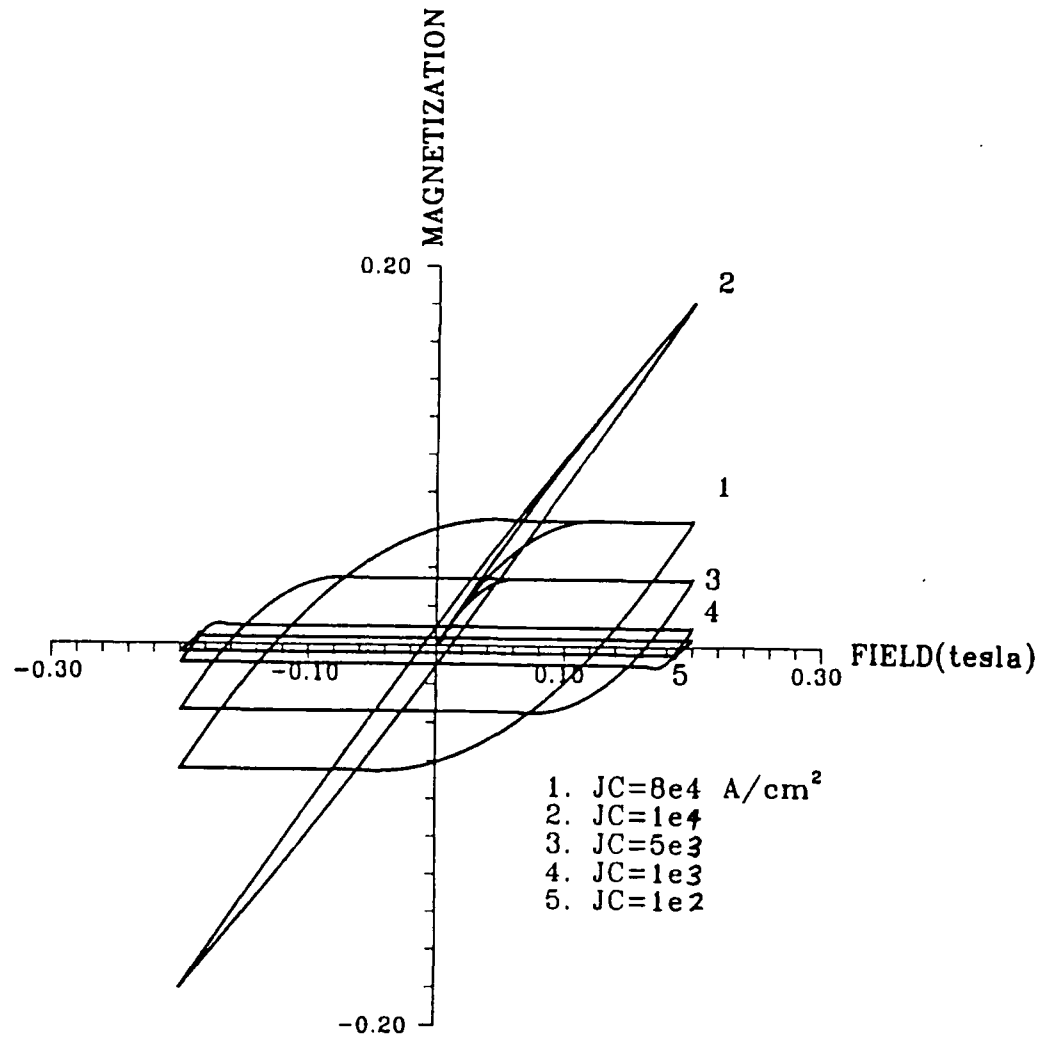
Figure 3.4.2.6        Magnetization Loops for HTSC Material as a Function
                      of Critical Current Density, for 10-Micron Grain
                      Size, And $10^{-4}$ m Sample Size

An intrinsic disturbance results in reducing the pinning forces, in causing the flux lines to flow ,and in lowering the critical current density. The induced flux motion results in generating heat and in raising the slab temperature.

The heat generated during a flux jump is uniformly dissipated in the case of LTSC. For high temperature superconductors losses occur mostly in the weak link region which will result in hot spots. The temperature rise of the weak link regions depends on its volume. [Note: The adiabatic stability of high temperature superconductor considering current both within the grains and through the weak links is still in progress.]

The ribbon width is plotted versus $J_c$ in Figure 3.5.1.2 for $f = 0.02$, 0.1, and 1. It is assumed that the transport current is 0.85 of the critical current and no safety factor is considered. Figure 3.5.1.3 is the same as Figure 3.5.1.2 but assuming a factor of safety equal 2. It can be seen from these figures that ribbon conductors will be adiabatically stable for high current density if weak links are eliminated which correspond to the case of having $f=1$. Weak links exist in all polycrystalline high temperature superconductors and f less than unity should be assumed. It will be practical to use high temperature superconductors for $J_c \gtrsim 10^4$ A/cm$^2$. Table 3.5.1.2 gives the ribbon dimensions at different values of f, safety factor, and $J_c$.

The ribbon width predicted by the above criterion is conservative since the heat capacity of the copper foils are entirely ignored. A less conservative criteria, dynamic stability, is discussed in the following section. It is assumed in obtaining the adiabatic stability criteria that the thermal diffusion process within the weak link region is fast resulting in uniform temperature. This is not necessarily true for HTSC as discussed later.

## Table 3.5.1.1
### Material Properties Used in Stability Analysis

|  | 78°K | 4.2°K |
|---|---|---|
| **Copper** | | |
| C (J/kg-°K) | 175 | 0.10 |
| density (kg/m$^3$) | 8900 | 8900 |
| resistivity (Ωm) | 2.8 x 10$^{-9}$ | |
|    B = 0 T | | 10$^{-10}$ |
|    B = 5 T | | 4 x 10$^{-10}$ |
| thermal conductivity (W/m°K) | 441 | |
|    B = 0 T | | 10$^3$ |
|    B = 5 T | | 260 |
| thermal diffusivity (m$^2$/s) | 2.82 x 10$^{-4}$ | |
|    B = 0 T | | 1.1 |
|    B = 5 T | | 0.3 |
| magnetic diffusivity (m$^2$/s) | 1.73 x 10$^{-3}$ | |
|    B = 0 T | | 8 x 10$^{-5}$ |
|    B = 5 T | | 3 x 10$^{-4}$ |
| **Y-123** | | |
| C (J/kg-°K) | 131 | ---- |
| density (kg/m$^3$) | 6300 | ---- |
| flux flow resistivity (Ωm) | 3 x 10$^{-8}$ | ---- |
| thermal conductivity (W/m°K) | 1.34 | ----- |
| thermal diffusivity (m$^2$/s) | 1.6 x 10$^{-6}$ | ----- |
| magnetic diffusivity (m$^2$/s) | 2.47 x 10$^{-2}$ | ----- |

## Table 3.5.1.2
### Adiabatically Stable Ribbon Width

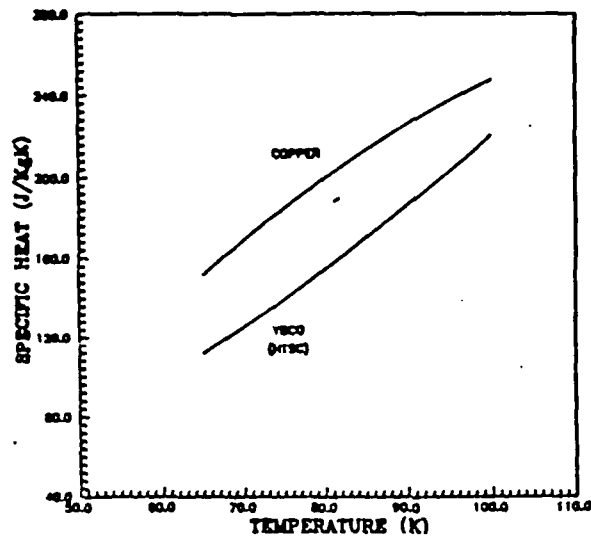| f | Safety Factor | $J_c$ (A/cm$^2$) | W(cm) |
|---|---|---|---|
| 0.02 | 1 | 10$^5$ | 0.096 |
| 0.10 | 1 | 10$^5$ | 0.214 |
| 1.00 | 1 | 10$^5$ | 0.676 |
| 0.02 | 2 | 10$^4$ | 0.484 |
| 0.10 | 2 | 10$^4$ | 1.076 |
| 1.00 | 2 | 10$^4$ | 3.388 |
| 0.02 | 2 | 10$^5$ | 0.047 |
| 0.10 | 2 | 10$^5$ | 0.107 |
| 1.00 | 2 | 10$^5$ | 0.388 |

Figure 3.5.1.1    Specific Heat vs. Temperature for Cu and Y-123

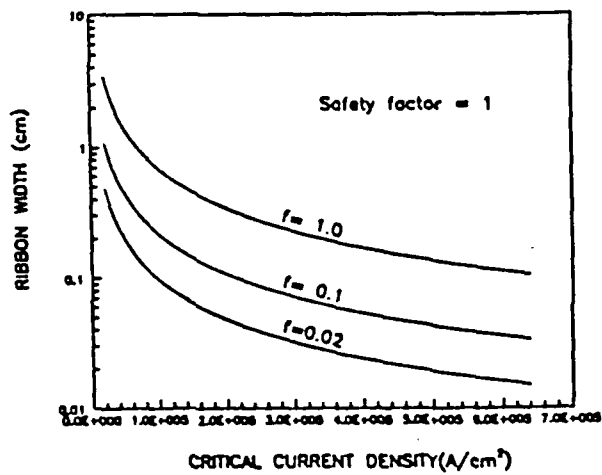

Figure 3.5.1.2    Ribbon Width for Adiabatic Stability,
                  Safety Factor - 1
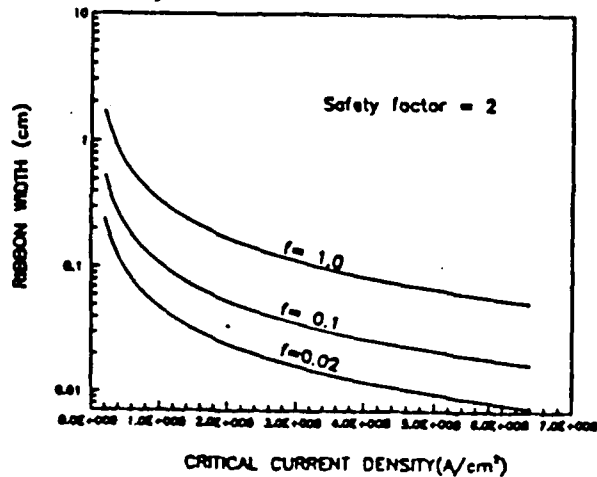


Figure 3.5...3    Ribbon Width for Adiabatic Stability
                  Safety Factor - 2

## 3.5.2   Dynamic Stability of Ribbon Conductors

Magnetic and thermal diffusion are not considered in the adiabatic stability analysis. The adiabatic stability criteria is obtained assuming that the heat generated following a flux jump is uniformly absorbed by the superconductor only. Current transfer to the stabilizing normal metal materials such as copper or silver is ignored. Both thermal and magnetic diffusion are considered in the dynamic stability analysis.

The thermal diffusivity $D_T = k/\gamma C$ and the magnetic diffusivity $D_M = \rho/\mu_o$ for copper are plotted versus temperature in Figure 3.5.2.1. It may be noted that $D_M$ for copper at 4.2 K is 4 orders of magnitude smaller than $D_T$. At liquid nitrogen $D_T$ is one order of magnitude less than $D_M$, Figure 3.5.2.1, resulting in a slower thermal diffusion process. The thermal diffusivity of YBCO is also shown in Figure 3.5.2.1 and it shows that heat diffusion is a very slow process within high temperature superconductors. A magnetic diffusivity value cannot be rigorously determined for the superconductor in the superconducting state when flux jump takes place. A flux flow resistivity $\rho_f$ is usually defined for low temperature superconductors. We assume by way of example that $\rho_f$ is $3 \times 10^{-8}$ $\Omega m$. The superconductor magnetic diffusivity using the same value of $\rho_f$ for high temperature superconductors is estimated to be $2.47 \times 10^{-2}$ $m^2/s$ which is one order of magnitude greater than $D_M$ for copper. The properties of Cu and superconductor at liquid nitrogen are given in Table 3.5.1.1 shown above.

Assume that a stack of ribbon conductors are used to form the superconducting slab shown in Figure 3.5.2.2. Copper foils are interleaved with the conductor and the stack edge is exposed to liquid nitrogen.

The losses in the superconductor depend on the current transfer process and the magnetic diffusion through both copper and superconductor. The ribbon conductor is represented by the normal metal and the superconductor slabs shown in Figure 3.5.2.3. Two cases are considered in this discussion to illustrate the effect of magnetic diffusion.

### Case 1: $D_M$ of the normal metal is large.

Current redistribution within the superconductor and current transfer to the normal metal take place following a flux jump disturbance. As current transfers to the normal metal it flows on the surface diffusing inward. The current density is expected to be uniform across the copper slab (y-direction, see Figure 3.5.2.3) in a short time since it is very thin. For large values of $D_M$ it is also expected that current diffuses fast in the x direction. The magnetic flux within the normal metal is primarily due to magnetic diffusion from the surface within the normal metal. The magnetic diffusion within the superconductor and the normal metal slab can thus be considered independent.

### Case 2: $D_M$ of the normal metal is small

In this case the current diffuses slowly in the normal metal. The current transfer along the normal metal surface will be primarily due to magnetic flux lines diffusing within the superconductor into the normal metal. This will make the stability criteria more restricted and surface cooling can improve conductor stability. The heat transfer coefficient in liquid nitrogen is about 10 W/cm$^2$, but the nitrogen cooling will be limited by thermal diffusion within the superconductor and the normal metal. More cooling can be promoted using a modified conductor design in which the liquid nitrogen can readily penetrated the windings.

Figure 3.5.2.4 shows the stable conductor width versus critical current density for the case where the safety factor is 2, and the copper resistivity ratio (rrr) is 30. Notice that the dynamically stable ribbon size is smaller than the adiabatically stable ribbon size.
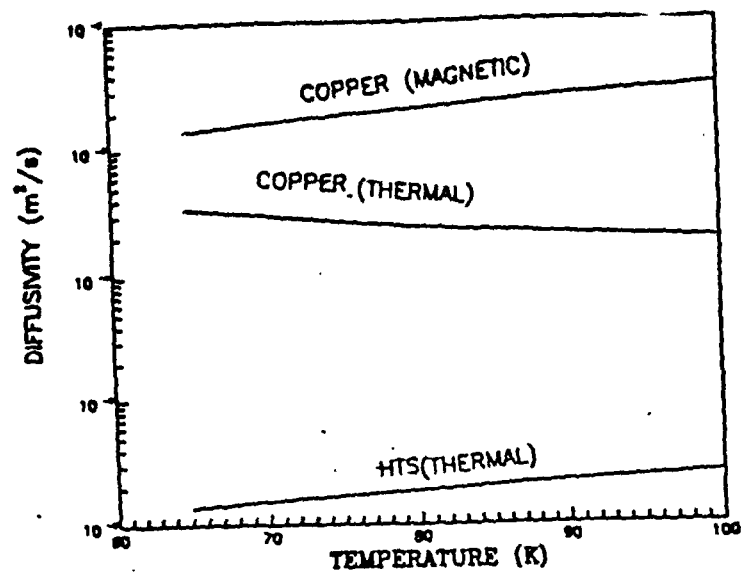
Figure 3.5.2.1    Thermal and Magnetic Diffusivity for Cu and Y-123
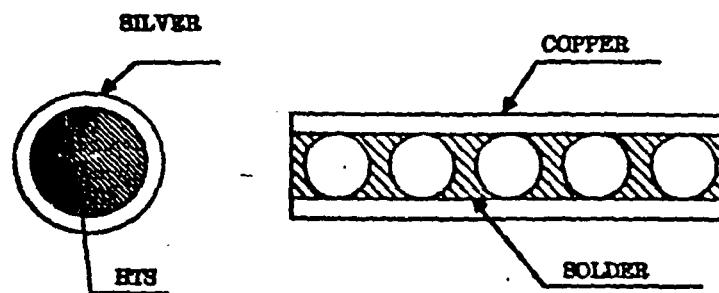


Figure 3.5.2.2    Ribbon Conductor Configuration
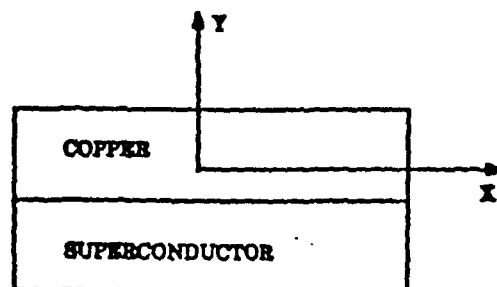


Figure 3.5.2.3    Slab Geometry for Dynamic Stability Model
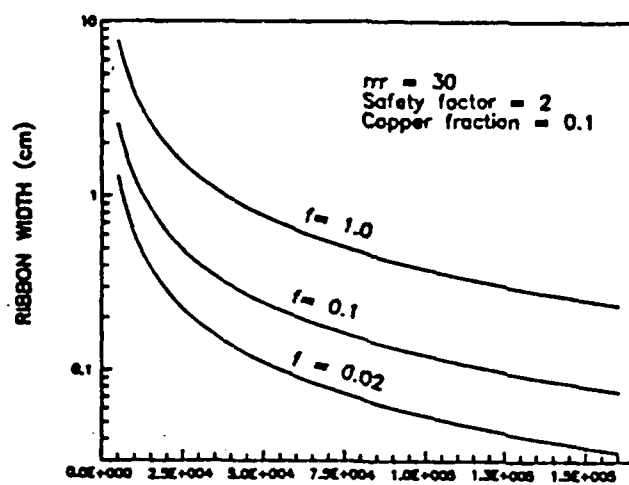
Figure 3.5.2.4    Ribbon Width for Dynamic Stability

## 3.6    Winding Stresses on Wire

A preliminary study was conducted on current winding practices to determine the mechanical stresses the wire encounters under various manufacturing processes. There are five basic methods presently used to wind electric machines:

1.  Manual coil placement or hand winding.

2.  ᴿ⁻e-winding coils and mechanical coil insertion.

3.  Skein wound coils.

4.  In-slot-winding by needle winding machines.

5.  Bobbin winding.

## 3.6.1    Manual Placement

The manual placing of coils into stators is currently only practiced in the manufacture of motors in very low volume batch work, for special motors and large formed coil machines. On small to medium sized machines, this involves winding the coils on winding forms which are designed to give the proper length of turn and approximate coil shape. Depending on the type of motor being wound, these coils can be a simple circle or rectangular in shape. The radius that the wire is bent over is usually greater than 3 mm on the rectangular coils and much larger for circular coils.

When wire is wound on a shaped form, the shape should be maintained even when the coils are removed from the forms. The characteristic that allows this to happen is called the spring-back resilience of the wire and is a function of the wire hardness and tension on the wire during the coil wind process. Experience has shown that in order to produce coils with minimal spring-back, the wire tension needs to be controlled to 65 to 85 percent of

the yield strength of the wire. The yield strength of copper is about 8.4 $kg/mm^2$, so copper windings generally experience a winding force of 5.5 to 7.1 $kg/mm^2$ (7,000 to 10,000 psi).

Winding rectangular coils can also induce additional stress in the wire from the velocity pulsations due to the irregular shape of the coils. Long-narrow forms can impose forces on the wires in excess of 8.5 $kg/mm^2$ if the coil winding speed is not well controlled.

The forces on the wire due to hand placement of the coils in the slots is very dependent on the individual doing the placement and the fullness of the slots. If the slots are above 60 percent full, it is not uncommon for the operator to use a hammer and slot knife to drive the wire to the bottom of the slots. However, this can be controlled with the proper instruction and design.

### 3.6.2 Coil Insertion Process

The second method, pre-winding coils and mechanical coil insertion, is the most widely used method in ac motors today. The forces the wires experience during the coil winding process are the same as above, however, the winding radii are usually a little greater with a 6 mm minimum.

During the insertion process the coils are removed from the formers to a transfer tool. This transfer tool is then positioned onto the coil insertion tooling and the windings are transferred into their insertion slots over the insertion lamella or blades. The insertion lamella are designed to protect the wires as they are inserted into the stator slots. They are highly polished and plated with a hard chrome to reduce the winding forces. The wire generally experiences bending radii greater than 6 mm.

### 3.6.3 Skein Winding

In the previous processes the coils and poles were individually wound on the formers and inserted in the stator. The skein winding process generates all the coils and poles for an entire phase from a single large coil. A large round coil of predetermined diameter is wound with the number of turns of a single coil. This large coil is then placed in a forming machine that forms the coils in a serpentine fashion to define the poles of the stator. These coils are then placed in the stator slots either by hand or with the coil insertion process.

The insertion forces on the wires are the same as the processes described above; however, the bending radii to wind and form the coils are greater than the pre-formed coils. Typical radii are usually greater than 10 mm.

### 3.6.4 Needle Winding

The in-slot-winding by needle winding machines are used on salient pole motors and wound rotors or armatures. The basic process consists of threading the wire through the arm of a gun winder and out a winding needle. The winding needle is then traversed though the slots of the stator or armature as it winds the wire directly in place one turn at a time. The main disadvantage of this process is the small bending radii that the wire will experience as it leaves the winding needle which can be as small as 1 mm.

As in the other processes, the winding tension needs to be near the yield strength of copper, or the material being wound, so that the wires stay in place as the tension is removed. If this is not done, the coils will be

very loose and will be capable of excessive movement during operation of the motor. The winding forces are also very erratic as the needle travels through the slots and around the ends of the core. These forces can be as high as 8.5 $kg/mm^2$.

## 3.6.5    Bobbin Winding

The final method commonly used is bobbin winding. This can be the gentlest process of the five discussed and is used in stepper motors, shaded pole motors, field windings, armature windings for large synchronous machines and homopolar field windings.

In this process an insulated bobbin, which is used in the final stator, is placed on a spindle winder and the wire is wound directly on the bobbin. Depending on the design of the motor, the shape of the bobbin can be either full round or rectangular. The winding tension on this process is typically in the 5.5 to 7.1 $kg/mm^2$ area to wind a good tight coil. However, this force can be reduced without experiencing any significant problems, in that the final turn on the bobbin can be secured to the bobbin prior to releasing the tension on the wire, thus eliminating the problems of spring-back. Based on manufacturing experience, a good bobbin wound coil can be made with half this tension or 2.8 to 3.6 $kg/mm^2$.

## 3.6.6    Winding Process Summary

The needle winding process imposes the highest forces and smallest bending radii on the wire and should be avoided in the design of HTSC machines. The bobbin wind process is the gentlest on the HTSC wire, and would be used for HTSC homopolar field coils. For volume production of HTSC

induction motors, it would be highly desirable to insertion wind the stators in that this is the most widely used and most economical automated process used today.

Based on this analysis, if a HTSC wire is produced with a copper clad shunt, then for small motors, the material needs to withstand forces of at least 3 kg/mm$^2$ and a minimum bending radius of 10 mm for bobbin wound coils. Larger motors could use a larger bending radius. For production of HTSC induction motors, the wire should withstand stresses of 6 kg/mm$^2$.

## 3.7     Summary

Major technical work for this reporting period have emphasized application studies for long term and near term HTSC wire and the study of the wire properties.

Homopolar DC and heteropolar DC motors have been considered for use with future HTSC wire with a current density of 100,000 Amperes/cm$^2$ in a field of three Tesla. Homopolar DC and AC induction motors are being designed for use with near term availability HTSC wire at 1000 Amperes cm$^2$ in a 0.01 Tesla (100 Gauss) field. Preliminary motor designs using iron flux paths for maximum torque have been presented.

Eddy current and hysteresis components of AC losses in HTSC wire have been analyzed. The conductor stability of a multifilamentary ribbon conductor has also been analyzed and presented.

The mechanical stresses on wire for various winding methods has been discussed. Their tradeoffs and suitability for HTSC wire has also been presented.

## SECTION 4

## GENERAL DISCUSSION AND SUMMARY

The program is close to the original schedule on all major tasks. We have chosen to design an HTSC motor which is appropriate for near-term HTSC wire, rather than an idealistic high-$J_c$ wire which may not be available by the second year of the program. We anticipate that this motor can be built and tested during the coming year. Motor performance should increase as the current capactity and field tolerance of the HTSC wire improves.

The task of making wire from Y-123 fiber has progressed well. Prototype clad wire has been made in about half-meter lengths, and the first coils of wire for the proof-of-principle motor are expected in the second quarter of the coming year. This wire is based on 100 micron Y-123 filaments, rather than the target 10 micron filament, but will have adequate flexibility in the near term. We expect to be able to decrease the fiber diameter as the program advances.

Concepts for the design of flexible clad-fiber HTSC wire were further developed for multifilamentary ribbon wire and a simpler monofil wire design. The relationship between diameter and bending radius was quantified, and compared with preliminary data. The residual thermomechanical stress in silver alloy claddings were estimated, so the strength of metal clad fiber could be predicted. The wire should have adequate strength for handling. Concepts and methods for producing filament transposition were defined. Analyses by Hillal of the University of Wisconsin, reported in Section 3, have led to improved understanding of eddy current and hysteretic losses for HTSC wire, and

determining the adiabatic and dynamic stability of ribbon conductors.

This program has rather stringent raw material requirements. Fiber spinning consumes large quantities of powder, and excellent sinterability is required to rapidly sinter Y-123 fibers. To supply the program, a process was placed into operation to manufacture reproducible phase pure Y-123 powder in kilogram quantities. This powder is made by solid state reaction, controlled to yield at least 98 wt% of the Y-123 phase, with traces of barium carbonate, barium cuprate, and "211". Jet-milling is used to produce a highly sinterable powder with an average particle size of $1.6 \pm 0.2$ microns and specific surface area of $2.5 \pm 0.3$ m$^2$/gm. All of the recent Y-123 green fibers are made with this powder.

The solvent-based dry spinning process for Y-123 green fibers has been replaced by a novel melt spinning process developed at Albany International Research Company. This process produces continuous 50 vol% Y-123 green fiber using conventional fiber spinning equipment. This a process readily lends itself to scale-up. The solvent-based dry spinning method is used only for small experimental lots.

A large number of thermoplastic resins, carrier polymer-lubricant blends, and processing conditions have been explored. The evaulations were based on processibility, binder burnout behavior, and properties related to continuous sintering of fibers. High density polyethylene-based systems presently make the best green fiber with Y-123. Melt spun green fiber has been prepared with diameters ranging between 50 and 330 microns at lengths up to about 0.5 kilometer. The current standard green fiber diameter is 125 micron in diameter. This grade of fiber is being used to supply the cladding and sintering operations. Development efforts continue to reduce fiber diameter

167

down to about 10 microns, to allow a more flexible wire to be produce.

The feasibility using braided Y-123 green fiber to produce multifilamentary wire with transposed filaments has been supported by recent success in producing continuous braids from the HDPE-based green fiber using a conventional braiding machine. Earlier work on simple braids showed that binder burnout and sintering is possible with braided green fiber. The task now is to increase the length of braid which can be made without fiber breakage.

The Y-123 green fiber can be coated with a silver or Ag/Pd alloy coating, which can be co-fired with the Y-123 during sintering. For the ribbon wire, the silver alloy coating provides a wettable surface for adhesion of the solder and acts as a barrier isolating the Y-123 from the solder. For the monofil wire, the silver alloy coating is the primary metallization, and serves all of the functions of the stabilizing metal. Presently about 100 meters of fiber are coated continuously. The system is still being developed to produce thicker, more uniform coatings.

The green fibers are sintered by two techniques. The older method, multiple zone sintering, produced 10-cm long samples by moving the fiber through the hot zone of a small tube furnace. Typically, a Y-123 fiber was exposed to about six repeated passes through the furnace, each involving 0.5- 5 minutes at peak temperature. Zone sintering was used to simulate continuous sintering, and to evaluate the sinterability of experimental powders and fibers, and to produce dense Y-123 filaments with self field critical currents as high as 2600 A/cm$^2$. Microstructure development during zone sintering has been characterized.

A commercial belt furnace was reconfigured for continuous sintering of fibers. This is currently being used to develop a process for continuous sintering of bare and Ag-coated Y-123 fiber. Green fibers are fed into this belt

furnace for binder removal and sintering. This process is the prototype for reel-to-reel manufacture, and has replaced the zone sintering method. It was necessary to overcome a number of practical problems related to the burnout characteristics of the green fiber, adhesion of the fiber to the belt cover, and some mechanical difficulties with the furnace itself. At present, fibers can only be semi-continuously sintered. The filament length was limited by two factors: 1) fiber breaks due to occasional problems believed to be related to burnout; and 2) the present need to pass the fibers through the belt furnace several times for binder burnout, presintering, and sintering.

The achievement of semi-continuous fiber sintering is significant because it demonstrates that coated green fiber an be carried through binder burnout and densification continuously without breaking. This indicates that the manufacture of composite wire from green fiber is feasible. Experiments on meter-length samples are in progress to define an optimal heating schedule. Based on these results, additional heating zones will be installed on the belt furnace so it can operate in true reel-to-reel mode.

A cladding method was developed to make the ribbon wire by solder bonding Y-123 filaments to cipper strips. A cladding machine has been built to do continuous cladding of continuous sintered Y-123 filaments. This machine is designed to fabricate the ribbon by sandwiching a sintered fiber array between copper foil strips and solder bonding them. The cladding module is presently being tested.

Several base metal deposition methods were evaluated as alternatives for cladding. Chemical vapor deposition, aqueous, and non-aqueous electrochemical methods were explored with the help a collaborators. At present, while these methods are able to produce sound deposits, they are not considered attractive

alternatives. It was determined that these base metals create insulating layers between themselves and the superconducting Y-123 filament.

Techniques were developed to directly measure the transport properties of single Y-123 filaments. This involved a rather long search for reliable methods to make low resistance electrical contacts to the tiny filaments. The Y-123 filaments have good properties, for bulk Y-123. The resistive transition show that the quality of the 100-micron filaments is equivalent to the best polycrystalline Y-123. Filaments have been produced with self-field critical currents up to 2600 A/cm$^2$, with typical performance around 1500 A/cm$^2$, both bare and metal clad specimen. The variability of th $J_c$ from one specimen to another, and within single specimens, has been characterized on a limited basis. These filaments, like all bulk Y-123, are weak-linked, so the $J_c$ drops to around 10 A/cm$^2$ at 800 G.

During this first year, nearly all of our attention has been devoted to the wire development task, and little attention was given to strategies for improving critical current. Clearly, weak-linked material cannot make wire of any practical use. This is, of course, the major challenge facing bulk HTSC materials. We believe that the fiber process could potentially yield high $J_c$ wire. A small effort has been directed to developing a type of melt processing, applicable to fine filaments, which could lead to a more practical version of melt texturing. In another small effort, we have begun to explore fibers of thallium cuprate materials. This activity will expand in the coming year.

Preliminary data on the mechanical properties of sintered Y-123 filaments indicate a fracture strength of 75-180 MPa. This data has been used to predict that long coils, with a 10-cm radius of curvature, can be wound from Ag/Pd clad 100 micron diameter filaments. These early data emphasize the crucial

role of the residual compressive stresses applied to the Y-123 by the cladding metal.

Progress has been made at Emerson Electric in HTSC motor design. After considering the characteristics of DC homopolar, heteropolar, reluctance, and induction motors, the induction and homopolar machines were selected as the machines for proof-of-principal. Assuming that current capacity and flexibility of early Y-123 wire will be limited, a novel type of drum homopolar machine has been designed. This machine has simple bobbin wound field coils to minimize bending stresses on the Y-123 wire and an iron magnetic circuit to allow useful horsepower output from as little as a 300 G field. This machine is explicitly designed to be a testbed for HTSC wire. A second motor under investigation is a cryogenic induction machine based on existing copper wound machines which operate immersed in liquid nitrogen.

ATTACHMENT I

REPORT SUMMARY


COMPOSITE CERAMIC SUPERCONDUCTING WIRES FOR ELECTRIC MOTOR APPLICATIONS



First Annual Report on
Contract Number  N00014-88-C-0512

July 7, 1989

John W. Halloran, Ceramics Process Systems Corporation,
Milford, MA 01757


This report describes progress on producing Y-123 wire for an HTSC motor.
The wire development activity includes synthesis of Y-123 powder, spinning
polymer-containing "green fiber", heat treating the fiber to produce metallized
superconducting filaments, and characterizing the electrical properties of the
filaments.  The HTSC motor has been designed and will be built by Emerson
Electric Company.

Signifiant progress has been made on the both the HTSC wire and on
the design of HTSC motors.  The program is close to the original schedule on all
major tasks. Prototype clad wire has been made in about half-meter lengths, and
the first coils of wire for the proof-of-principle motor are expected in the
second quarter of the coming year.

The design of flexible clad-fiber HTSC wire was refined for both
ribbon conductor design and a simpler monofil wire design.  The relationship
between diameter and bending radius was quantified, and compared with preliminary
data.  The strength of metal clad fiber was calculated. Concepts and methods for
producing filament transposition were defined. Progress was made in defining the
eddy current and and hysteretic losses for HTSC wire, and determining the
adiabatic and dynamic stability of ribbon conductors.

A process was placed into operation to manufacture reproducible phase
pure Y-123 powder in kilogram quantities.  This powder is made by solid state
reaction, controlled to yield at least 98 wt% of the Y-123 phase, with traces
of barium carbonate, barium cuprate, and "211".  Jet-milling is used to produce
a highly sinterable powder with an average particle size of $1.6 \pm 0.2$ microns
and specific surface area of $2.5 \pm 0.3$ m$^2$/gm.  All of the recent Y-123 green
fibers are made with this powder.

A novel melt spinning process has been developed at Albany
International Research Company to manufacture continuous green fiber containing
50 vol% Y-123 carried in a polymer blend. The melt spun fibers are made with
conventional fiber spinning equipment with a process which readily lends itself
to scale-up.  Consequently, melt spinning has been adopted as the preferred
method of producing green fiber.  The solvent-based dry spinning method is used
only for small experimental lots.

A large number of thermoplastic resins, carrier polymer-lubricant blends, and processing conditions have been explored. The evaulations were based on processibility, binder burnout behavior, and properties related to continuous sintering of fibers. High density polyethylene-based systems presently make the best green fiber with Y-123. Melt spun green fiber has been prepared with diameters ranging between 50 and 330 microns at lengths up to about 0.5 kilometer. The current standard green fiber diameter is 125 micron in diameter. This grade of fiber is being used to supply the cladding and sintering operations. Development efforts continue to reduce fiber diameter down to about 10 microns, to allow a more flexible wire to be produce.

The feasibility using braided Y-123 green fiber to produce multifilamentary wire with transposed filaments has been supported by recent success in producing continuous braids from the HDPE-based green fiber using a conventional braiding machine. Earlier work on simple braids showed that binder burnout and sintering is possible with braided green fiber.

The Y-123 green fiber can be coated with a silver or Ag/Pd alloy coating, which can be co-fired with the Y-123 during sintering. For the ribbon wire, the silver alloy coating provides a wettable surface for adhesion of the solder and acts as a barrier isolating the Y-123 from the solder. For the monofil wire, the silver alloy coating is the primary metallization, and serves all of the functions of the stabilizing metal. Presently about 100 meters of fiber are coated continuously. The system is still being developed to produce thicker, more uniform coatings.

The green fibers are sintered by two techniques. The older method, multiple zone sintering, produced 10-cm long samples by moving the fiber through the hot zone of a small tube furnace. Typically, a Y-123 fiber was exposed to about six repeated passes through the furnace, each involving 0.5- 5 minutes at peak temperature. Zone sintering was used to simulate continuous sintering, and to evaluate the sinterability of experimental powders and fibers, and to produce dense Y-123 filaments with self field critical currents as high as 2600 A/cm$^2$. Microstructure development during zone sintering has been characterized.

A commercial belt furnace was modifed make it suitable for continuous sintering of fibers. This is currently being used to develop a process for continuous sintering of bare and Ag-coated Y-123 fiber. Green fibers are fed into a belt furnace for binder removal and sintering. This process is the prototype for reel-to-reel manufacture, and has replaced the zone sintering method. To progress from the tube furnace to the belt furnace it was necessary to overcome a number of practical problems related to the burnout characteristics of the green fiber, adhesion of the fiber to the belt cover, and some mechanical difficulties with the furnace itself. At present, fibers can only be semi-continuously sintered. The filament length was limited by the present need to pass the fibers through the belt furnace several times for binder burnout, presintering, and sintering.

The achievement of semi-continuous fiber sintering is significant because it demonstrates that coated green fiber an be carried through binder burnout .nd den ification continuously without breaking. This indicates that the manufacture of composite wire from green fiber is feasible. Experiments on meter-length samples are in progress to define an optimal heating schedule. Based on these results, additional heating zones will be installed on the belt furnace so it can operate in true reel-to-reel mode.

A solder reflow method was developed to clad fibers to make the ribbon wire. A cladding machine has been built to do continuous cladding of continuous sintered Y-123 filaments. This machine is designed to fabricate the ribbon by sandwiching a sintered fiber array between copper foil strips and solder bonding them. The cladding module is presently being tested.

Techniques were developed to directly measure the transport properties of single Y-123 filaments. The resistive transition show that the quality of the 100-micron filaments is equivalent to the best polycrystalline Y-123. Filaments have been produced with self-field critical currents up to 2600 $A/cm^2$, with typical performance around 1500 $A/cm^2$, both bare and metal clad specimen. These filaments, like all bulk Y-123, are weak-linked, so the $J_c$ drops to around 10 $A/cm^2$ at 800 G.

Preliminary data on the mechanical properties of sintered Y-123 filaments indicate a fracture strength of 75-180 MPa. This data has been used to predict that long coils, with a 10-cm radius of curvature, can be wound from Ag/Pd clad 100 micron diameter filaments.

Notable progress has been made at Emerson Electric in HTSC motor design. After considering the characteristics of DC homopolar, heteropolar, reluctance, and induction motors, the induction and homopolar machines were selected as the machines for proof-of-principal. Assuming that current capacity and flexibility of early Y-123 wire will be limited, a novel type of drum homopolar machine has been designed. This machine has simple bobbin wound field coils to minimize bending stresses on the Y-123 wire and an iron magnetic circuit to allow useful horsepower output from as little as a 300 G field. A second motor under investigation is a cryogenic induction machine.

<u>ATTACHMENT II</u>

ARPA ORDER NUMBER: 9525

PROGRAM CODE NUMBER: 7737

CONTRACTOR:          Ceramics Process Systems Corporation
                     155 Fortune Boulevard
                     Milford, MA   01757

CONTRACT NUMBER:   N00014-88-C-0512

CONTRACT EFFECTIVE DATE:        30 JUNE 1988

CONTRACT EXPIRATION DATE:       31 MARCH 1991

SHORT TITLE OF WORK:    High Temperature Superconducting Wire and Motor

PRINCIPAL INVESTIGATOR: John W. Halloran
                        (508) 634-3422


This report describes progress on developing Y-123 wire for an HTSC motor. The wire develoment activity includes synthesis of Y-123 powder, spinning polymer-containing "green fiber", heat treating the fiber to produce metallized superconducting filaments, and characterizing the electrical properties of the filaments. A melt spinning process was developed for producing 125-micron diameter green fiber containing 50 vol% Y-123.  This fiber can be braided for producing transposed multifilamentary wire. A process was developed to coat green fiber with silver alloys which can be co-fired to yield Ag-clad Y-123 wire. Half-meter prototypes of wire were produced by continuous sintering. A second process for multifilamentary ribbon wire is also being developed.

The Y-123 filaments have 77° self-field $J_c$ values up to 2600 A/cm$^2$. They are weak-linked, with $J_c$ reduced to 10 A/cm$^2$ at 800 G. Preliminary data is presented on mechanical properties.

A DC homopolar motor with an iron magnetic circuit is being designed at Emerson Electric as the first proof-of-principle motor. This machine is designed to operate with early HTSC wire. A cryogenic induction motor is being evaluated as a second application. Models have been developed to caluculate eddy current loss, hysteresis loss, and adiabatic and dynamic stability in HTSC wires.

ARPA ORDER NUMBER:  9525                PROGRAM CODE NUMBER:  7737

CONTRACTOR:          Ceramic Process Systems Corporation
                     155 Fortune Boulevard
                     Milford, MA 01757

CONTRACT NUMBER:  N00014-88-C-0512      CONTRACT AMOUNT: $ 5,509,387.00

EFFECTIVE DATE OF CONTRACT:   30 JUNE 1988

EXPIRATION DATE OF CONTRACT:   31 MARCH 1991

PRINCIPAL INVESTIGATOR:        John W. Halloran

TELEPHONE NUMBER:              (508) 634-3422

SHORT TITLE OF WORK:    High Temperature Superconducting Wire and Motor

REPORTING PERIOD:       30 JUNE 1988 through  30 JUNE 1989

## DESCRIPTION OF PROGRESS

This report describes progress on developing Y-123 wire for an HTSC motor. The wire develoment activity includes synthesis of Y-123 powder, spinning polymer-containing "green fiber", heat treating the fiber to produce metallized superconducting filaments, and characterizing the electrical properties of the filaments. A melt spinning process was developed for producing 125-micron diameter green fiber containing 50 vol% Y-123. This fiber can be braided for producing transposed multifilamentary wire. A process was developed to coat green fiber with silver alloys which can be co-fired to yield Ag-clad Y-123 wire. Half-meter prototypes of wire were produced by continuous sintering. A second process for multifilamentary ribbon wire is also being developed.

The Y-123 filaments have 77° self-field $J_c$ values up to 2600 A/cm$^2$. They are weak-linked, with $J_c$ reduced to 10 A/cm$^2$ at 800 G. Preliminary data is presented on mechanical properties.

A DC homopolar motor with an iron magnetic circuit is being designed at Emerson Electric as the first proof-of-principle motor. This machine is designed to operate with early HTSC wire. A cryogenic induction motor is being evaluated as a second application. Models have been developed to caluculate eddy current loss, hysteresis loss, and adiabatic and dynamic stability in HTSC wires.

SUMMARY OF SUBSTANTIVE INFORMATION DERIVED FROM SPECIAL EVENTS
        Project members attended the several conferences on high temperature superconductivity to keep abreast of current developments.

CHANGE IN KEY PERSONNEL
        No change

PROBLEMS ENCOUNTERED AND/OR ANTICIPATED
        None

ACTION REQUIRED BY THE GOVERNMENT
        None

FISCAL STATUS (JUNE 30,1989)

1)      CUMULATIVE AMOUNT CURRENTLY RECEIVED
        ON CONTRACT . . . . . . . . . . . . . . . . . . $ 1,442,278

2)      CUMULATIVE EXPENDITURES AND
        COMMITTMENTS TO DATE

            EXPENSES PRIOR TO 06/02/89....$1,442,278

            EXPENSES 06/03/89 - 06/30/89
            (INVOICE OUTSTANDING).......$ 123,553

                                TOTAL . . . . . . . $ 1,565,831

3)      ADDITIONAL FUNDS REQUIRED TO COMPLETE WORK

            THROUGH 2/28/90 (expense forecast) . . . . . $ 1,647,851
            THROUGH 3/31/91 . . . . . . . . . . . . . . .$ 3,943,557